REVIEW

Short-pulse lasers for weather control

To cite this article: J P Wolf 2018 Rep. Prog. Phys. 81 026001

View the article online for updates and enhancements.

Related content

- Ultrashort filaments of light in weakly ionized, optically transparent media
 L Bergé, S Skupin, R Nuter et al.
- Laser-assisted water condensation in the atmosphere: a step towards modulating precipitation?
- J Kasparian, P Rohwetter, L Wöste et al.
- Tunnel ionization, population trapping, filamentation and applications
 See Leang Chin and Huailiang Xu

Recent citations

 Maximizing energy deposition by shaping few-cycle laser pulses
 Julien Gateau et al



IOP ebooks™

Bringing you innovative digital publishing with leading voices to create your essential collection of books in STEM research

Start exploring the collection - download the first chapter of every title for free.

Rep. Prog. Phys. 81 (2018) 026001 (34pp)

https://doi.org/10.1088/1361-6633/aa8488

Review

Short-pulse lasers for weather control

J P Wolf

Department of Applied Physics (GAP), University of Geneva, 1211 Geneva 4, Switzerland

E-mail: jean-pierre.wolf@unige.ch

Received 27 September 2016, revised 12 July 2017 Accepted for publication 7 August 2017 Published 19 December 2017



Corresponding Editor Professor Masud Mansuripur

Abstract

Filamentation of ultra-short TW-class lasers recently opened new perspectives in atmospheric research. Laser filaments are self-sustained light structures of 0.1–1 mm in diameter, spanning over hundreds of meters in length, and producing a low density plasma (10^{15} – 10^{17} cm⁻³) along their path. They stem from the dynamic balance between Kerr self-focusing and defocusing by the self-generated plasma and/or non-linear polarization saturation.

While non-linearly propagating in air, these filamentary structures produce a coherent supercontinuum (from 230 nm to 4 μ m, for a 800 nm laser wavelength) by self-phase modulation (SPM), which can be used for remote 3D-monitoring of atmospheric components by Lidar (Light Detection and Ranging). However, due to their high intensity $(10^{13}-10^{14}~{\rm W~cm^{-2}})$, they also modify the chemical composition of the air via photo-ionization and photo-dissociation of the molecules and aerosols present in the laser path. These unique properties were recently exploited for investigating the capability of modulating some key atmospheric processes, like lightning from thunderclouds, water vapor condensation, fog formation and dissipation, and light scattering (albedo) from high altitude clouds for radiative forcing management. Here we review recent spectacular advances in this context, achieved both in the laboratory and in the field, reveal their underlying mechanisms, and discuss the applicability of using these new non-linear photonic catalysts for real scale weather control.

1

Keywords: ultrashort lasers, lightning, filamentation, atmosphere, clouds, plasma

(Some figures may appear in colour only in the online journal)

1. Introduction

The prevention of damaging weather phenomena like flooding, drought, hail and lightning strikes has been a dream for centuries, attracting attention to broadly defined weather control techniques. The modification of the Earth's weather and climate by human activities has been however mainly provoked unintentionally, as collateral damage of economic interests, and with consequences in contradiction to the original goal mentioned above. Global warming has induced some irreversible damages to the earth system and increased the occurrence of damaging meteorological events such as drought and flooding (IPCC 2013). For instance, the flood exposure of the global population is increasing by a factor 4–14 over the 21st

century as compared to the former one (up to 25 if the population rise is considered; IPCC 2013, Kundzewicz *et al* 2014). These natural catastrophes and uneven access to fresh water may also increase tensions and conflicts between neighboring countries. In order to modulate the amount of precipitations locally, extensive studies have been carried out based on cloud seeding using chemicals like silver iodide (AgI), liquid propane or dry ice. Hundreds of programs dedicated to precipitation enhancement by cloud seeding were and still are carried out in the USA, Russia, Europe, Canada, Australia and more recently in China and the UAE (Czys 1995, Qiu *et al* 2008, Baum 2014). For instance, only in China, a National Weather Modification Office has been setup, employing as much as 48000 people and armed with 50 airplanes, 7000

rocket launchers and 7000 cannons to harvest more rain from the atmosphere. The chemical seeding technology has, however, not significantly evolved since the first demonstration by B Vonnegut, V Schaefer and I Langmuir in 1946. Despite these 70 years of efforts, no definitive consensus is met today on the efficiency of the seeding process to enhance precipitation (NRC 2003, Garstang *et al* 2004, IPCC 2013), nor on the environmental impact of the involved chemicals.

On a global scale, injecting sulphur compounds into the stratosphere (10-20 km altitude) was proposed for enhancing the cloud coverage and thus reducing the solar radiation at ground level (Crutzen et al 2003, 2006, Keith 2013). The idea originated from the observation of the effect of large volcanic eruptions such as the one of Mount Pinatubo in 1991. Rough estimations to counteract global warming by fossil fuel emissions result in the need of some 25 thousand tons of sulphur injected in the stratosphere per year by 2020, rising to 250 thousand tons per year by 2030 (Keith 2013). The side effects of such massive measures obviously have to be thoroughly investigated, so that the reduction of radiative forcing by the enhanced stratospheric albedo is not realized at the cost of some other undesirable side effects. We all keep in mind the unforeseen dramatic impact of chlorofluorocarbons (CFC) on the ozone layer, while they were initially selected for their chemical inactivity at ground level. The debate and the political/ethical aspects about the necessity of using dedicated geo-engineering measures is not the scope of this article. However, there is a clear call for additional scientific investigations about the different options proposed today, as well as for basic research dedicated to invent further possible tools. A risk, which should not be discarded either, is that the development of new tools, efficient and environmental friendly, may have negative political impacts on the mitigation of fossil fuel emissions in the future.

Weather control also concerns some direct economical/industrial aspects, such as diverting lightning from sensitive installations, clearing fog from airports runways and for enhancing free space optical data transmission, or reducing hail damage on cultivation fields.

For instance, only in the USA, on-going research evaluates lightning costs and losses to several billion USD per year (Curran *et al* 1997, Diels *et al* 1997, NOAA 1998, NLSI 2009) including e.g. forest fires (50% of the forest fires in the western USA are lightning-caused), breakdown of electrical networks, aircrafts repair costs and airlines operating costs (\$2 billion per year; NOAA 1998), and destruction of electronic devices. It is important to notice that lightning strikes do not only produce direct damages and casualties but also indirect damages due to the intense electromagnetic field that they generate.

Following the steps of Benjamin Franklin and his famous lightning kite in 1750, many scientists used rockets pulling electric wires to trigger and guide lightning discharges (Newman *et al* 1967, Fieux *et al* 1975, 1978, Hubert *et al* 1984). These rockets play the role of an artificial leader rising to the cloud until the breakdown field is reached. The discharge then follows the least resistive path so that the strike is guided along the wire. In most cases, the conducting copper

wire is directly connected to the ground. However, it may also be connected to the ground via an insulating Kevlar cable, so that leaders are initiated in both directions at higher altitude (Lalande *et al* 1998, Saba *et al* 2005). Interestingly, only a few tens of meters of copper wire are sufficient to trigger lightning bolts. The success rate for this technique reaches 60% (Fieux *et al* 1975, 1978). However, the limited quantity of rockets available, their associated costs, and their consecutive fall on the ground (possibly hazardous for the installations that were intended to be protected) constitute major drawbacks for a widespread use of the method.

A potential alternative to rocket launching for lightning control or chemical seeding for precipitation enhancement has recently emerged: the use of ultrashort, high intensity lasers, which produce long ionized channels while propagating through the air. The aim of the present article is to review the potential and the capabilities of these intense laser filaments for controlling atmospheric processes associated to the earth weather and climate.

2. Filamentation of high intensity lasers in air

2.1. Non-linear propagation and laser filamentation

When the peak power of a laser exceeds a critical value P_c , its propagation in a transparent medium becomes non-linear, and self-actions like self-focusing and self-trapping ('filamentation') of the light appear. Although these phenomena were already described in the early '60s in solids and liquids (Askaryan 1962, Chiao et al 1964, Hercher 1964, Lallemand et al 1965, Shen et al 1965, Talanov 1965, Javan et al 1966), the first observation of filamentation in air, requiring femtosecond lasers, was achieved 30 years later (Braun et al 1995). The experiment from Braun et al demonstrated that self-trapping, or filamentation, in air can be explained as a dynamic balance between Kerr self-focusing from the intensity dependent refractive index and defocusing from both diffraction and plasma generation. Since then, a detailed description of the filamentation process has been achieved and reported in review articles (Chin et al 2005, Bergé et al 2007, Couairon et al 2007, Kasparian et al 2008b) and books (Chin 2010, Bandrauk et al 2016). For this reason, we will concentrate here on some key aspects and concepts of femtosecond filamentation, which are useful for the description of atmospheric control applications in the next sections.

The most accurate description of filamentation requires a microscopic, quantum, treatment of the strong field-matter interaction using, for instance, the time dependent Schroedinger equation (TDSE) as well as an inclusion of many body effects treated in a density matrix formalism (Schuh *et al* 2016). The solutions from TDSE, which include both the non-linear atomic polarization and the free electrons (as continuum states) can be coupled to a Maxwell based wave equation (similar to equation (2.1)) to evaluate the evolution of the field (Lorin *et al* 2007, 2012, 2015, Bejot *et al* 2013, Kohler *et al* 2013, Richter *et al* 2013, Spott *et al* 2014). The modified field will then modify the TDSE, and the propagation will be treated in an iterative way. Remarkable and

pioneering developments in this respect have been obtained by Laurin and Bandrauk in Canada (Lorin *et al* 2007, 2012, 2015, Bandrauk *et al* 2016). The complexity and long computing time however still limit these most accurate descriptions of the filamentation process to millimeter scale propagation distances. Therefore, in most of the reported theoretical studies and numerical simulations, the microscopic description of the field-atom interaction was abandoned in favor of macroscopic average parameters, which values are empirically determined on the basis of experimental results.

From Maxwell's equations, the vector wave equation describing the propagation of a laser pulse in a transparent medium reads (Bergé *et al* 2007):

$$\Delta \mathbf{E} - \nabla \left(\nabla \cdot \mathbf{E} \right) - \frac{1}{c^2} \frac{\partial^2}{\partial t^2} \mathbf{E} = \mu_0 \left(\frac{\partial^2}{\partial t^2} \mathbf{P} + \frac{\partial}{\partial t} \mathbf{J} \right)$$
(2.1)

where E is the electric field of the wave, P the polarization of the medium (which includes non-linear terms) and J the current density from free charges. As in most cases, the transverse dimensions of the beam are much larger than the wavelength. This equation can be simplified as a paraxial equation:

$$\Delta \mathbf{E} - \frac{1}{c^2} \frac{\partial^2}{\partial t^2} \mathbf{E} = \mu_0 \left(\frac{\partial^2}{\partial t^2} \mathbf{P} + \frac{\partial}{\partial t} \mathbf{J} \right). \tag{2.2}$$

As compared to the traditional, linear, wave equation, the propagation of the field is governed by an intensity dependent non-linear polarization P (including Kerr self-focusing) and a current J, originating from the ionization of the medium by the laser,

$$\frac{\partial \mathbf{J}}{\partial t} = -\frac{e^2}{m_e} \rho \mathbf{E} \tag{2.3}$$

where ρ is the electron density in the generated plasma, and which evolution depends on the efficiency of the ionization processes (multiphoton, tunnel, avalanche; Keldysh 1965, Perelomov and Popov 1967, Perelomov *et al* 1967), the recombination with the ions, the attachment to neutrals, etc. The laser induced plasma leads to defocusing of the beam, but also to losses, associated to the photo-ionization process itself and interaction with the free electrons like inverse bremsstrahlung.

In these classical, macroscopic approaches, the dependence of P on the laser intensity is related to experimental values. So, the function P(E) can, for instance, be fitted by a truncated polynomial function, which validity is restricted to the intensity interval of interest (Loriot *et al* 2009, 2010, Bree *et al* 2011, Bejot *et al* 2013), or expanded in a converging Taylor power series, as in the usual framework of non-linear optics (Agrawal 2001, Boyd 2008):

$$P(E) = \varepsilon_0 \left(\chi^{(1)} \cdot E + \chi^{(3)} : EEE + \chi^{(5)} : EEEEE + .. \right)$$

where the $\chi^{(j)}$ are jth order susceptibility tensors (generally of rank j+1). All even orders vanish because of inversion symmetry of the isotropic medium. The first, linear term combines with the left hand side time derivative term in (2.4) to give rise to the linear refractive index $n_0^2 = (1 + \chi^{(1)})$ and its

associated dispersion with frequency. Most often, the perturbation expansion is stopped at the first non-linear term, i.e. the third order (although some theoretical works consider the 5th order as well, (Nurhuda *et al* 2002a, 2002b, Vincotte *et al* 2004)). Besides being at the origin of third harmonic generation, the third order term of the complex *E* field (assumed here as linearly polarized) thus gives rise to the well-known Kerr effect (assumed instantaneous here):

$$P_{\rm NL} = \varepsilon_0 \ \chi^{(3)}(E^*E)E = \varepsilon_0 \ \chi^{(3)}|E|^2E$$
 (2.5)

with
$$\chi^{(3)} = 4\varepsilon_0 c n_2 n_0^2 / 3$$
 (2.6)

(2.6) defines the nonlinear refractive index n_2 , which value is $\sim 3 \cdot 10^{-19} \text{ cm}^2 \text{ W}^{-1}$ in air (at 800 nm). Substituting the total polarization (linear and non-linear) $P = \varepsilon_0 \left(\chi^{(1)} + \chi^{(3)} |E|^2 \right) E$ into the wave equation results in the appearance of an 'effective refractive index':

$$n_{\rm eff} = n_0 + n_2 I \tag{2.7}$$

where *I* is the intensity of the field $I = \varepsilon_0 c |E|^2/2$

This increase of the refractive index with intensity yields, in the case of a laser beam, to self-focusing (the Kerr effect), as the intensity is larger at the center of the beam than at the edge. Moreover, the focal length of this Kerr lens becomes shorter as the beam propagates (and the intensity increases) leading to the collapse of the beam. The collapse of the beam is however arrested by diffraction or higher order processes such as the ionization of the gas (eighth order for multi-photon ionization at 800 nm of O2 and eleventh order for N2). As the effect of the plasma current $\frac{\partial \mathbf{J}}{\partial t}$ (see (2.3)) in the propagation equation is of opposite sign of the one of Kerr self-focusing, a dynamic balance between both effects occurs, leading to stable self-guided light structures: the 'filaments'. While this simple model of dynamic balance between Kerr self-focusing and plasma formation is extensively used in the literature because of its simplicity, it is however worth reminding that it is definitely incomplete.

As already mentioned, historically the balance leading to self-guiding was considered between Kerr self-focusing and diffraction (the transverse part of the Laplacian in equation (2.2)). More precisely a critical value P_c of the laser power was defined in this context (Chiao *et al* 1964, Marburger 1975) for:

$$P_{\rm c} = \frac{3.72 \,\lambda_0^2}{8\pi n_0 n_2}.\tag{2.8}$$

In air, at 800 nm, the value of the critical power P_c varies between 3 GW and 10 GW, depending on the experimental conditions, especially the beam profile and on laser pulse duration (Liu *et al* 2005, Wahlstrand *et al* 2012). The relation (2.8) gives 3.2 GW for $n_2 = 3 \cdot 10^{-19}$ cm² W⁻¹. The balance between self-focusing and defocusing also clamps the maximum intensity in the filament, at a typical value of ~5 · 10^{13} W cm⁻² in air at 800 nm.

The most widespread form of the non-linear propagation equation bases on the assumption that the field is linearly polarized (say, along e_x), propagating along e_z , in paraxial

approximation and that it can be described as a pulse with a slowly varying envelope (SVEA) as compared to its carrier frequency:

$$\boldsymbol{E}(\boldsymbol{r},t) = \frac{1}{2}\varepsilon(\boldsymbol{r},t)\exp\mathrm{i}\left(k_0z - \omega_0t\right)\boldsymbol{e}_x + \mathrm{c.c.}$$
 (2.9)

Under these conditions, the propagation is described by the evolution of the envelope, in the frame of the pulse $(t \to t - \frac{z}{v_g})$, with v_g the group velocity) as a non-linear Schroedinger type equation (NLSE):

$$\frac{\partial}{\partial z}\varepsilon = \frac{i}{2k_0}\Delta_{\perp}\varepsilon - i\frac{k''}{2}\frac{\partial^2}{\partial t^2}\varepsilon + i\frac{k_0}{n_0}n_2|\varepsilon|^2\varepsilon
- i\frac{k_0}{2n_0^2\rho_c}\rho\varepsilon - \frac{\sigma}{2}\rho\varepsilon - \frac{\beta^{(K)}}{2}|\varepsilon|^{2K-2}\varepsilon$$
(2.10)

where the transverse Laplacian accounts for diffraction, the second term for dispersion $(k'' = \frac{\partial^2 k}{\partial \omega^2})$, the third for Kerr self-focusing, the fourth for plasma defocusing, the fifth for losses due to inverse Bremsstrahlung (with σ its associated cross-section, see Raizer (1965)), and the last for losses due to multi-photon ionization. In this expression, we also introduced the critical plasma density $\rho_c = \varepsilon_0 \omega_0^2 m_e/e^2$ (~1.7 · 10²¹ cm⁻³ at 800 nm) beyond which the plasma becomes opaque for the optical radiation. $\beta^{(K)} = K\hbar\omega_0\sigma_K\rho_{\rm at}$ is a coefficient representative of the efficiency of ionizing a gas of density $\rho_{\rm at}$ with a K photons cross-section σ_K .

As mentioned earlier, the free electron density ρ has to be computed in combination with the propagation equation. For intensities $I < 10^{13} \text{ W cm}^{-2}$ multiphoton ionization (MPI) dominates so that the evolution of the plasma density can be reasonably well approximated by:

$$\frac{\partial \rho}{\partial t} = (\rho_{\rm at} - \rho) \, \sigma_K I^K + \frac{\sigma}{U_i} \rho I - \alpha \rho^2 \tag{2.11}$$

where avalanche ionization is considered in the second right hand side term (with σ the inverse Bremsstrahlung cross-section and U_i the ionization potential of the considered species). The plasma decay is expressed by the effective recombination rate α .

However, in most cases, the low intensity MPI approximation is not sufficient to describe filamentation, and tunnel ionization has to be included as well (figure 1). The full ionization rate W(I), replacing the MPI rate in (2.11) has been derived by Keldysh (1965) and Perelomov, Popov and Terentev ('PPT', Perelomov and Popov 1967, Perelomov *et al* 1967) in their seminal works of the '60s for atoms and ions. For a detailed description of these ionization theories in the context of filamentation, the reader is referred to (Couairon *et al* 2007, Bergé *et al* 2007, Bandrauk *et al* 2016). Notice that, alternately, some authors use the MPI formulation with non-integer K values to account for tunneling such as, e.g. K = 7.5 instead of 11 for N_2 and K = 6.5 instead of 8 for O_2 (Kasparian *et al* 2000), obtained by a local fit of the PPT solution for a given intensity range.

Figure 2 shows, for example, the results of solving the propagation equation as well as an actual picture of an 800 nm laser filament in the laboratory. Self-focusing is clearly

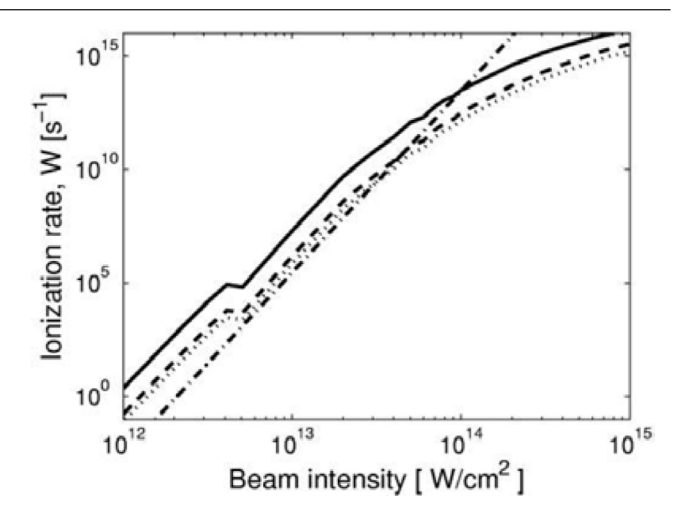


Figure 1. Ionization rate of O_2 molecules versus laser intensity obtained from the PPT theory (solid curve), Ammosov–Delone–Krainov (ADK) molecular model (dashed curve), the fitting curve from PPT with $Z_{\rm eff} = 0.53$ (dotted curve) and the MPI-like formulation (dash-dotted curve) at 800 nm. Reproduced with permission from Bergé *et al* (2007) © IOP Publishing Ltd. All rights reserved. Please notice the 15 orders of magnitude on the vertical scale.

observed from the initial beam diameter of 4 mm to the collapse point at 6 m distance. At this distance plasma is generated efficiently with a peak density at $10^{17}\,\mathrm{cm^{-3}}$, which arrests self-focusing by the electron cloud's defocusing. Beyond this non-linear focus, a dynamical balance is established between the two competing processes as well as diffraction, yielding a filament of $100\text{--}200\,\mu\mathrm{m}$ diameter over several metres distance. Self-channeling will stop as soon as the losses due to ionization and inverse bremsstrahlung are too high for being compensated by the surrounding photon reservoir around the filament.

We would like to underline again that the description in this section constitutes only an introduction about the mechanisms underlying the filamentation process. Several aspects, like retarded Kerr effect, higher order Kerr terms, Raman processes, self-steepening, non-paraxial effects, harmonics generation etc have not been considered for simplicity. Also, the non-linear Schroedinger equation (2.10) is nowadays advantageously replaced by a more general equation which treats the full electric field and not only its envelope: the unidirectional pulse propagation equation (UPPE) derived originally by Kolesik and Moloney (2004) and Kolesik *et al* (2002).

The typical characteristics of a single near IR (800 nm) filament propagating in air at power levels amounting some P_c (i.e. a few mJ pulse energies for femtosecond pulses), are summarized as follows:

Diameter	100–200 $\mu \mathrm{m}$
Length:	1-10 m
Intensity:	$10^{13} - 10^{14} \mathrm{W} \;\mathrm{cm}^{-2}$
Plasma density:	$10^{15} - 10^{17} \mathrm{cm}^{-3}$

At higher laser powers, the beam breaks up in a multitude of filaments, initiated by modulational instability. For several years, it was commonly accepted that the number of filaments scaled with the total power in the laser beam, more precisely,

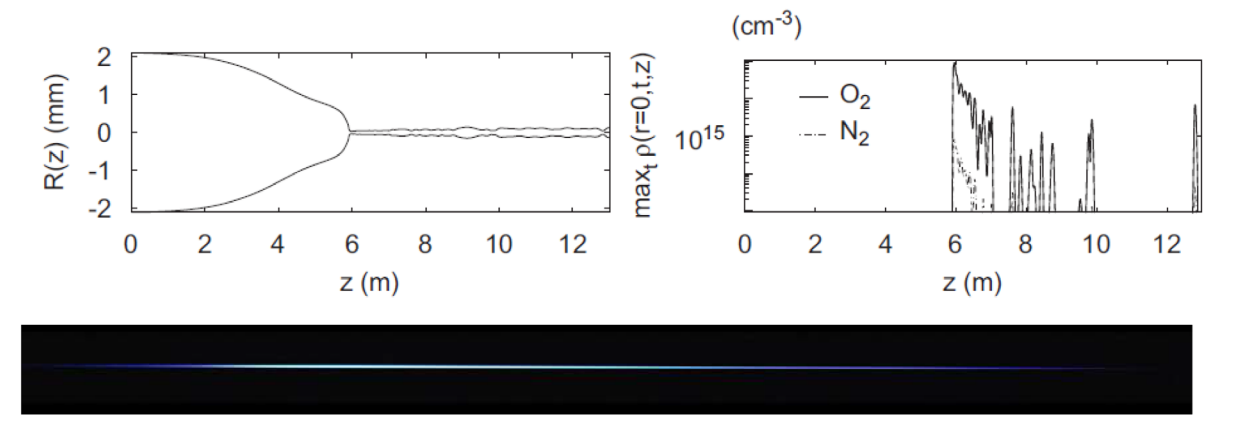


Figure 2. Filamentation in air at $\lambda = 800 \, \text{nm}$, duration = 50 fs. Upper left: Computed radius of the beam as a function of the propagation distance and right associated maximum electron density. Reprinted with permission from Couairon and Bergé (2002), Copyright by the American Physical Society. Lower: Side picture of a ~1 m long filament in the laboratory revealed by its characteristic blueish luminescence due to plasma recombination lines.

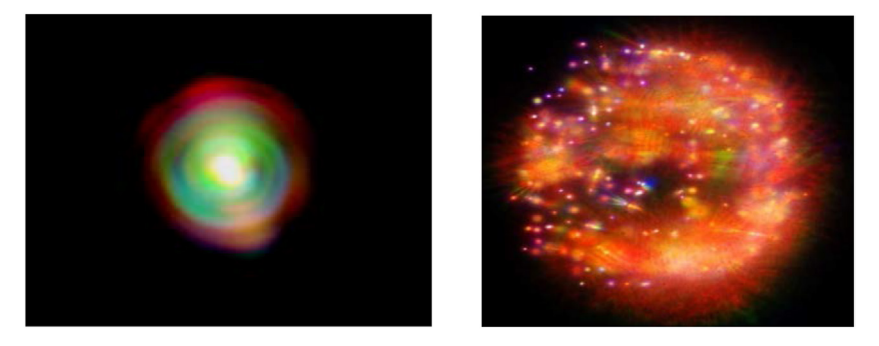


Figure 3. Real color image of the cross-section of a NIR filamenting laser beam. Left: low power beam leading to a single filament (beam diameter ~1 cm). Right: multi-filamenting sub-PW beam at the HZDR-laser facility in Rossendorf (beam diameter ~10 cm).

that each filament was bearing typically 5–10 P_c . However, a new feature of multi-filamentation recently emerged while increasing the incoming beam intensity with 100 TW-class lasers: the saturation of the filament surface number density (Henin et al 2010) due to filament-filament interaction (Ettoumi et al 2015, Mongin et al 2017). This 'geometrical' saturation was shown to occur also for lower TW-class lasers as soon as the beam diameter was reduced. The filaments number density is therefore mainly dependent on the beam intensity, rather than on the beam power. The threshold for geometrical saturation to appear is found around 0.5 TW cm⁻². This feature has practical consequences for atmospheric applications because a higher intensity remains in the photon bath surrounding the filaments, which starts to contribute to non-linear processes like photo-ionization or photo-dissociation as well (see section 3.3).

The colorful features observed in figure 3 originate from self-phase modulation in the filaments. This coherent supercontinuum, spanning from 200 nm to 14 μ m (Chin et al 1999, Kasparian et al 2000b, Kasparian et al 2003, Theberge et al 2008), arises because the intensity dependent refractive index (e.g. Kerr effect in equation (2.7)) also varies in time with the pulse shape. The phase of the carrier then shifts with the envelope's amplitude, yielding new frequencies in the spectrum. Supercontinuum generation by self-phase modulation was observed already in the early '70s in solids and gases by Alfano et al (1970a, 1970b). The angular distribution of the

different spectral components is, at least partially, emitted in a cone of different apex angles. This conical emission has been observed for the first time in air by Nibbering *et al* (1996), and has been extensively studied since then (for a comprehensive overview, see e.g. (Bergé *et al* 2007, Couairon *et al* 2007, Faccio *et al* 2008, Maioli *et al* 2009)).

2.2. Long distance filament propagation and atmospheric turbulence

TW-class mobile systems allowed to observe filamentary structures up to the kilometer range, both in vertical and horizontal pointing configurations (La Fontaine *et al* 1999, Mechain *et al* 2004, Rodriguez *et al* 2004, Skupin *et al* 2004a, Durand *et al* 2013). To this end, the laser pulses are often chirped, so that the dispersion of air while propagating and the lower initial peak power allow to shift the filamentation onset to longer distances from the laser. A key feature of the filaments revealed by these investigations over long distance is that the length of individual filaments increases with propagation distance, turning from optically turbulent cells to clusters of longer pillars, bearing however lower intensities (Skupin *et al* 2004b). In addition, some of these long optical pillars appeared to be 'plasma free' (Mechain *et al* 2004).

A significant difficulty for obtaining stable filaments at kilometric distances on a horizontal path is the presence of atmospheric turbulence (Durand *et al* 2013). Both the size of

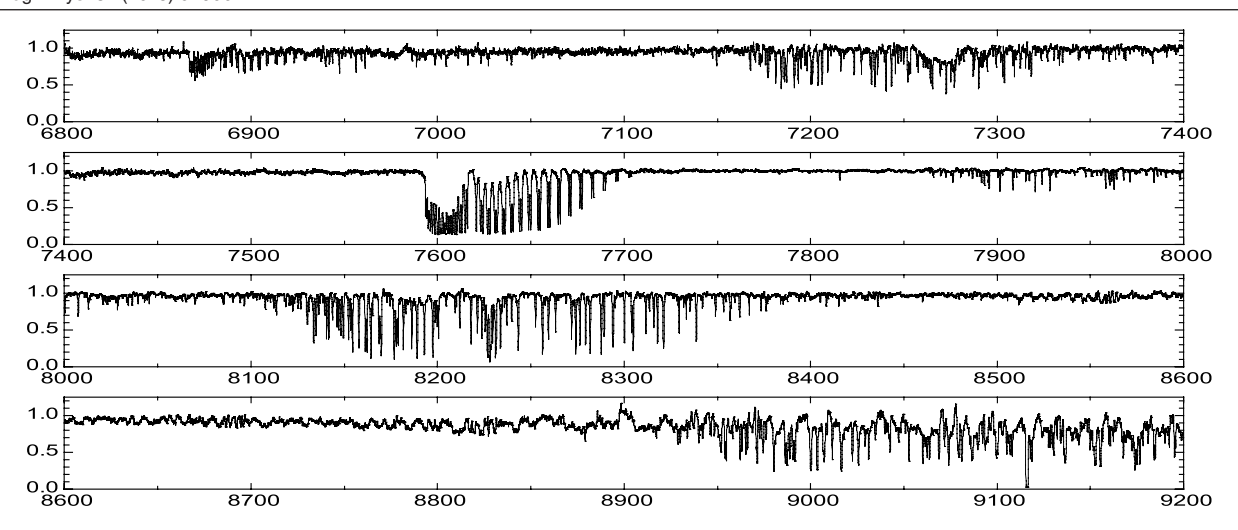


Figure 4. Spectrally resolved backscattered supercontinuum from 4.5 km altitude, using a filament based Lidar system. From Kasparian *et al* (2003). Reprinted with permission from AAAS.

the turbulence cells and the turbulence strength (represented by, e.g. the structure parameter of the refractive index C_n^2 ; (Kolmogorov 1991, Salame et al 2007)) play a role to this respect. In the early 2000s hope was raised in the community that filaments could be less affected by atmospheric turbulence than traditional Gaussian beams, because they self-modify the refractive index. However, filaments are strongly dependent on their surrounding photon reservoir, which unfortunately follows the wandering induced by turbulence. As a consequence, most of the studies concluded that the wandering of filaments is similar to that of a Gaussian beam (La Fontaine et al 1999, Chin et al 2002, Fujimoto et al 2002, Salame et al 2007, Ma et al 2008, Silaeva et al 2010). On the other hand, filaments are surprisingly robust in air turbulence once they are formed, their onset may be shifted and new filaments can even be nucleated by the modulated refractive index within turbulent cells (Kandidov et al 1999, Ackermann et al 2006b, Salame et al 2007, Houard et al 2008, Paunescu et al 2009, Eeltink et al 2016).

The question of self-stabilization of filaments in air turbulence was recently revisited (Schubert *et al* 2016b) in the context of the hydrodynamic channeling process by high average power laser beams (sections 4.3 and 5.4). Unfortunately no improvement in the filament pointing stability was observed for high repetition rate, high average power lasers, but rather an additional wandering induced by the heating from the laser itself (Yang *et al* 2015, Schubert *et al* 2016b).

If adaptive optics methods (Pfeiffer *et al* 2006, Daigle *et al* 2008, 2009, Ionin *et al* 2013), analogous to the ones used in astronomy, are likely to efficiently counteract turbulence induced wavefront distortion in a vertical pointing geometry, correction on a long horizontal path remains a real challenge.

2.3. Remote sensing using laser filament based non-linear Lidars

The supercontinuum generation within filaments was the original motivation of using filaments for atmospheric applications, especially Lidar (stands for 'Light Detection and

Ranging') remote sensing; (Measures 1992, Frejafon et al 1998, Wolf 2000, Weitkamp 2005). In the late 1990s, both laboratory experiments in air and aerosols (Nibbering et al 1996, Kasparian et al 1997, Kasparian and Wolf 1998, Kasparian et al 1998b, Hill et al 2000) and filament based Lidar investigations in the atmosphere (Woeste et al 1997, Rairoux et al 2000, Kasparian et al 2000b) were performed. These experiments set the grounds for a very innovative French-German research program: The Teramobile. The aim of the program was to develop the first mobile TW-laser to perform field experiments, and in particular atmospheric diagnostics and non-linear Lidar remote sensing (Wille et al 2002, Kasparian et al 2003). Several systems were constructed by different groups after the experience of the Teramobile, for instance the T&T (Kamali et al 2009) in Canada, the ENSTA-mobile (Forestier et al 2012) in France, and at CREOL (Webb et al 2014) in the USA, and are even nowadays commercially available (TT-mobile, Amplitude Technologies, France).

The use of filaments for Lidar based atmospheric diagnostics mainly concentrated (1) on the absorption features of atmospheric constituents along the optical path and (2) on the fluorescence from plasma recombination lines (Xu and Chin 2011) or from multi-photon excited species (Mejean *et al* 2004). In both cases, a major advantage of the Lidar detection is that the backwards emitted signal (scattering or fluorescence) is detected as a function of the time of flight of the light (i.e. time resolved), which provides spatially resolved measurements of concentrations.

The major advantage of supercontinuum based Lidars is that they are able to address simultaneously a large number of molecules, in contrast to the usual DIAL (differential absorption Lidar) technique, where a couple of laser transmitted wavelengths are chosen about an absorption line of a single specific species (e.g. a pollutant like NO, NO₂, SO₂, ozone, etc, (Frejafon *et al* 1998)). Therefore, filament based Lidars allow for an 'analysis' of the atmosphere without the need for an *a priori* knowledge of the pollutants to detect.

As an example, figure 4 shows the backscattered light recorded with the Teramobile Lidar from 4.5 km altitude.

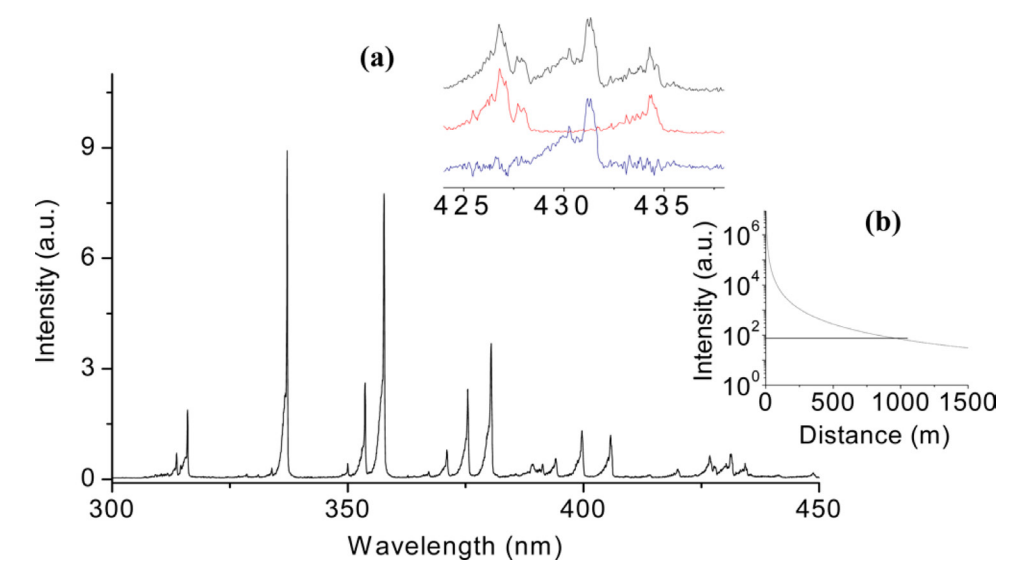


Figure 5. Filament-induced fluorescence spectrum of mixture of CH₄ and air with a CH₄ concentration of 2.6% (v./v.). The inset (a) shows the spectrum of methane in air (top), the spectrum of pure air in atmospheric pressure (middle), and the subtraction of the mixture and pure air spectra (bottom) The inset (b) shows the simulation of the detection limit according to the LIDAR equation. The 3σ detection limit was found to be about 0.9 km for a CH₄ concentration of 5% and a filament length of 20 m, where σ is the standard deviation of the background level. Reproduced from Xu and Chin (2011) CC BY 3.0.

The supercontinuum, generated at lower altitude, could be observed up to 18 km altitude, and was analyzed by a time gated high resolution spectrometer. The very rich spectrum clearly displays the rovibrational absorption bands of water vapor (around 730 nm, 820 nm and 900 nm) and of molecular oxygen (A band around 760 nm). A detailed analysis of the bands as a function of altitude allowed retrieving simultaneously the atmospheric temperature profile (via the lineshape and the ground state population of O₂) and the atmospheric water vapor content profile. Additionally, the analysis of the Mie scattering pattern provided information about the size distribution of the water droplets in the atmosphere at this moment allowing a direct and complete analysis of the meteorological properties of the air column (Bourayou et al 2005). While near-IR is attractive for meteorological soundings, trace gases and pollutants are mainly detected in the UV (NO, NO₂, SO₂, Ozone, aromatic hydrocarbons) and the mid-IR (CO, CO₂, volatile organic compounds (VOC)). As already described the UV-supercontinuum was found to extend down to 200 nm, also in conjunction with the coupling with the third harmonic generation of 800 nm, i.e. at 267 nm. Although Lidar measurements of the backscattered supercontinuum in this spectral range were already carried out in 2003 (Kasparian et al 2003), no simultaneous detection of pollutants like nitrogen oxides and ozone were reported yet. The main difficulty for this attractive remote sensing method in the deep UV is related to conical emission, which exhibits wide apex angles and strong wavelength dependence in this region (Maioli et al 2009). The design of the light collection geometry of the Lidar receiver is therefore a complicated task to achieve, in order to avoid distance related artefacts.

Attempts were carried out in the infrared, and the part of the spectrum around 1–1.7 μ m could be successfully detected up to 4 km altitude with the Teramobile laser (Mejean *et al* 2003). The most interesting pollutant signatures, from VOC

(volatile organic compounds), lie in the C–H stretching band around 3.3 μm or C-C band around 10 μm . At these wavelengths the backscattering efficiency, however, significantly drops as the molecular Rayleigh scattering scales with λ^{-4} , where λ is the laser wavelength. Moreover, the signal to noise ratio of multispectral, time gated spectrometers is also significantly decreased as compared to UV-vis. In order to compensate for this sensitivity decrease, new mid-IR supercontinuum sources are critically needed. Developments are currently performed both on the mid-IR laser source (Haberberger et al 2010, Andriukaitis et al 2011, Pigeon et al 2015, Shumakova et al 2016) up to the TW-level, and on mid-IR filamentation in air (Kartashov et al 2013, Mitrofanov et al 2015a, 2015b, Liang et al 2016). In particular, the first mid-IR filamentation experiment in the atmosphere was recently realized (Mitrofanov et al 2015a, 2015b). The properties of these mid-IR light bullets appear very attractive, because the break up in multi-filaments is reduced thank to the higher critical powers (λ_0^2 dependence, see equation (2.8)). Ultra-intense single channels are predicted to propagate over kilometric distances (Panagiotopoulos et al 2015, 2016). If these developments are successful mid-IR supercontinuum Lidars could be set-up to analyze in 3D the VOC (or other chemical) content over industrial plants and refineries, identify fugitive sources, analyze hazardous plumes from accidental chemical releases or from industrial fires, monitor vertical profiles of greenhouse gases, identify pathogens or chemical agents, etc.

As mentioned above, the second widely used method for stand-off detection using filaments in the atmosphere is the remote analysis of plasma fluorescence lines. This method, called 'clean fluorescence', because of the absence of blackbody background radiation in femtosecond plasmas, was developed and extensively used by the group of S L Chin (2010). Several hydrocarbons and halocarbons were detected in air with this technique, as well as powders (Gravel *et al*

2004, Luo et al 2006, Xu et al 2007, Chin et al 2009, 2012, Kamali et al 2009, Xu and Chin 2011, Li et al 2016). For example, methane was detected at the percent level in air by subtracting the pure methane spectrum from the spectrum recorded for methane mixed in air (figure 5).

The band results from the $A^2\Delta - X^2\Pi$ transition of CH. It results from multiphoton dissociation/ionization of CH₄ in the plasma filament.

From the signal to noise ratio measured at the laboratory scale (few meters distance between the detector and the sample), an extrapolation based on the Lidar equation (see, e.g. Measures 1992, Frejafon *et al* 1998) led to an estimated detection limit of 5% at 900 m.

Exciting novel perspectives in filament based remote sensing have been recently opened by the discovery of population inversion in atmospheric filaments and associated lasing. This induced 'air laser' can potentially be used to emit light preferentially towards the laser/Lidar transmitter, and thus overcome the usual $1/R^2$ signal decay (R is the distance between the Lidar system and the section of air that is analyzed), due to the decreasing solid angle of detection with distance. Originally discovered by S L Chin in the early 2000 (Luo et al 2003), stimulated emission from molecular nitrogen has been recently extensively revisited and refined (Shneider et al, 2011, Sprangle et al 2011, Yao et al 2011, Kartashov et al 2012, Penano et al 2012, Liu et al 2013, 2015, Wang et al 2013, Zhang et al 2013, Mitryukovskiy et al 2014, Laurain et al 2014, Point et al 2014, Kartashov et al 2015, Xu et al 2015). Additionally, schemes involving oxygen have been successfully demonstrated, which even widens the possibilities of the 'air lasing' approach (Dogariu et al 2011, Hemmer et al 2011, Traverso et al 2012).

Although fascinating perspectives are related to these new stimulated emission processes inside remote atmospheric filaments, we will now concentrate in the following sections on the use of intense laser filaments for not only observing the atmosphere, but to some extent, to control it.

3. Laser induced water condensation in the atmosphere

3.1. Background and early experiments using UV-lamps

The air is said « saturated » in water vapor (S=1, i.e. relative humidity RH is 100%) when an equilibrium is established between evaporation and condensation on a flat surface of liquid water (Pruppacher and Klett 1997, Seinfeld and Pandis 2006). In the case of a pure water droplet, the curvature induces an increase of internal pressure due to surface tension (known as the Kelvin effect) so that higher gas saturation values (S>1) are required to stabilize it. For instance during an adiabatic expansion in a cloud chamber, the saturation S reaches several units because of fast cooling and droplets are formed; these will, however, re-evaporate and disappear as soon as the temperature stabilizes back to its initial value (as S will). In the real atmosphere, homogenous nucleation would require S>3 (Kasparian $et\ al\ 2012$), which makes it irrelevant. Mixing water with other chemical substances can

compensate the Kelvin effect, allowing even small radii particles to grow at S < 1. When a vapour molecule is added to the droplet surface the Gibbs free energy increases because of surface tension, but adding a species with a chemical potential $\mu_{\rm I}$ in the liquid phase, which is lower than the corresponding potential $\mu_{\rm V}$ in the gas phase, leads to a decrease of Gibbs free energy, and thus stabilization. Different scenarii of nucleation rely on how the chemical potential can be varied in the water droplet, by the presence of other chemical substances, ions, and/or a soluble or insoluble solid phase. Some of these scenarii critically depend on the presence of light and photo-induced chemical reactions.

Already by the end of the 19th century, C T R Wilson observed the formation of fog in an expansion cloud chamber, when it was exposed to different kinds of radiation (Wilson 1899). This discovery awarded him the Nobel Prize in 1927, for the detection of ionizing particles in nuclear physics. Wilson also investigated the effect of UV light and found that UV was able to induce fog at much lower water saturation ratios ($S \simeq 1$) than that required for x-rays and high energy particles ($S \simeq 4$). Even more surprising: the UV generated droplets persisted 'for some hours at least'. This suggests, according to classical nucleation theory, that the droplets were stabilized into a local minimum of the Gibbs energy for this micrometric size. Wilson identified oxygen as a key ingredient of this chemical stabilization: water drops combine with reactive oxygen in contact with them, leading to dissolved H_2O_2 .

These initial experiments were repeated and refined by different groups (Farley, 1951, Hoppel and Dinger 1973, Reiss et al 1977, Wen et al 1978). They mainly supported Wilson's conclusions about the crucial role of oxygen and that the condensation nuclei were electrically neutral. Clark and Noxon conducted similar experiments but shorter wavelengths $(150 \,\mathrm{nm} \leqslant \lambda \leqslant 170 \,\mathrm{nm})$ (Clark and Noxon 1971). The most spectacular result was the generation of photoinduced water fog even under widely undersaturated conditions (typically down to $S \simeq 0.5$). They found a spectral dependence of the photonucleation rate that points to direct absorption by water molecules as the initial step. The addition of molecular oxygen and CO₂ increased the rate of particle production while N₂ quenched the process. This was interpreted as evidence for the involvement of singlet oxygen, O(¹D), produced by photolysis of O_2 or CO_2 , which yields the formation of $\cdot OH$ radicals.

3.2. Laser based laboratory experiments

The first demonstration of water vapor condensation by laser radiation was performed in the early 2000s by scientists from the Teramobile project (Kasparian *et al* 2003). They used a femtosecond Ti:Sapphire laser (50 fs, 1 mJ, 800 nm, 1 kHz) to generate a filament in a supersaturated diffusion cloud chamber. Unlike an expansion chamber, supersaturation is achieved via a strong temperature gradient. In the region where warm, humid, air mixes with the colder air mass, local supersaturation is achieved, similarly to exhaled air in a cold winter atmosphere. In these supersaturated conditions, the spectacular production of fog droplets by the laser filaments (as shown in figure 6) was attributed to condensation on the

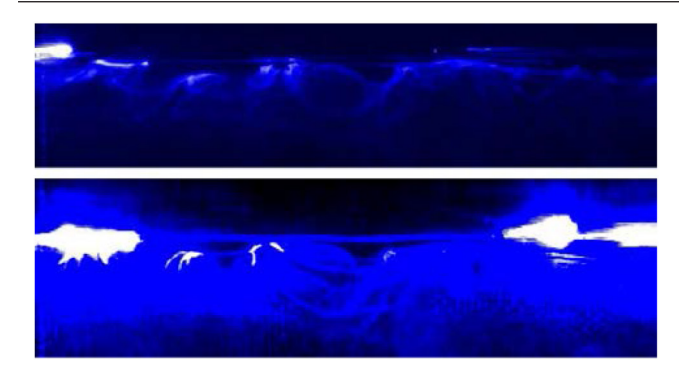


Figure 6. First demonstration of laser induced condensation in a cloud chamber (see Luderer (2001) and Kasparian *et al* (2003)). The particles produced by the short plasma filament over 5 cm length are monitored by elastic scattering of an additional low power cw laser. Vortices due to laser heating and plasma shockwaves are clearly visible.

ions produced in the laser plasma, analogous to the Kelvin–Thomson process induced by UV radiation and ionizing particles in the Wilson chamber (Luderer 2001, Kasparian *et al* 2003). Thanks to the high intensity in the filaments (10–100 TW cm⁻²), multiphoton and tunnel ionization of the air species lead indeed to plasma densities of the order of 10¹⁵–10¹⁷ cm⁻³ (Bergé *et al* 2007, Couairon *et al* 2007). Visualization of the laser induced fog formation in the chamber was achieved by an additional low power continuous wave (cw) laser, which was elastically scattered by the generated droplets.

Some years later, another laser induced water condensation was performed using nanosecond UV lasers (ArF, 250 mJ, $\lambda = 193 \,\mathrm{nm}$) by Yoshihara (2005). Since the UV-laser photons energy (6 eV) was insufficient for directly ionizing water vapor (6.5 eV), nitrogen (15.6 eV), or oxygen (12 eV) molecules, the only potential source of ions under these conditions could arise from resonance enhanced two-photon absorption. However the available intensity was relatively modest (10⁷ W cm⁻²) for efficient two-photon ionization, and the preferred interpretation of the observed UV-laser induced condensation process relied mainly on photochemical pathways, analogous to the ones described earlier by Wilson and by Clark and Noxon (1971). More precisely, the suggested pathway was: photodissociation of O₂ into oxygen atoms in the ³P state, formation of ozone, release of singlet oxygen (¹D) from a second photodissociation process, then formation of ·OH radicals and finally hydrogen peroxide H₂O₂. Several subsequent experiments were performed by the same group to confirm this photochemical pathway, including different wavelengths (figure 7) (248 nm: Yoshihara et al 2012; 266 nm with ozone precursor: Yoshihara et al 2014), experimental arrangements (soap bubble, diffusion/flow chambers), and diagnostics (light sheet imaging, differential mobility analyzers (DMA), cavity ringdown spectrometers (CRDS)).

The most recent experiments related to nanosecond UV-laser induced water condensation were dedicated to the direct observation of $\rm H_2O_2$ formation by CRDS spectroscopy (at 436 nm) when a flow chamber containing synthetic air with ozone and water vapor was irradiated by a 266 nm laser. The main outcome of these pump-probe experiments was

the quantitative assessment of both the creation of hydrogen peroxide by the UV irradiation and the efficient nucleation of water droplets by $\rm H_2O_2$ (Yoshihara *et al* 2014). The concentration of $\rm H_2O_2$ produced by the UV laser radiation in the chamber was estimated to about $6 \cdot 10^{14}$ molecules cm⁻³ (ca. 20 ppm vol) at 263 K, i.e. 4 orders of magnitude higher than in the natural atmosphere (Hua *et al* 2008).

In the non-linear optical regime, numerous additional photochemical pathways are possible. The use of high intensity laser filaments are therefore particularly attractive for laser water condensation processes. In the pioneering experiment reported in Kasparian et al (2003), water condensation was achieved under supersaturated conditions. However, the authors noticed that the residence time of the generated droplets widely extended beyond the return to sub-saturated conditions, pointing out photochemical stabilization mechanisms other than charge stabilization. In order to investigate these photochemical mechanisms, a new diffusion chamber was developed, allowing control of temperature, temperature gradients, relative humidity and air flow. A comprehensive series of experiments was performed with this cloud chamber (figure 8) by irradiating it with 220 mJ, 60 fs pulses (10 Hz) at 800 nm from the Teramobile system (Wille et al 2002). This led to a bundle of 20-30 filaments in the chamber, each bearing an intensity of typically $5 \cdot 10^{13} \,\mathrm{W} \,\mathrm{cm}^{-2}$. The most spectacular result was the observed massive production of micrometer sized droplets (measured with a Malvern Spraytec particle sizer) even under widely sub-saturated conditions (RH = 75%), after only a few seconds (Rohwetter *et al* 2010).

The unexpected stability of these micrometer-sized water droplets under sub-saturated conditions rely on the generation of additional dissolved substances that modify the chemical potential of the droplets and compensate the Kelvin surface tension by the Raoult effect (Pruppacher and Klett 1997). Because of the extreme intensities within laser filaments, highly reactive elements are generated by multi-photon ionization or dissociation of N_2 , N_2 , or N_2 , or N_2 , N_2 , N_3 , N_2 , N_3 , N_2 , N_3 ,

A natural route to hydrophilic species photo-production appeared thus as the nitric acid route (Kulmala et al 1993, Seinfeld and Pandis 2006) via NO, NO₂, O₃, and N₂O₅ (or direct OH oxidation of NO₂), which is a common process in the natural atmosphere, as for the sulphuric acid route (H₂SO₄-H₂O condensation). In our case, since the nitrogen related species are directly produced from the molecular nitrogen of the air, their concentration widely dominate the sulphur related traces present in the atmosphere. For this reason, the production of NO_x and ozone by laser filaments was investigated in flow chambers (Petit et al 2010). Typical concentrations of 200 ppb of ozone and 50 ppb NO_x were measured in the whole cell (at a 2.5 l min⁻¹ flow), which corresponded to a local concentration in the 100 μ m diameter filaments volume of 400 ppm O₃ and 100 ppm NO_x. Different pathways were identified for producing these high concentrations of trace gases, among them (for NO, with different branching ratios):

$$N^+ + O_2 \rightarrow NO^+ + O^-$$

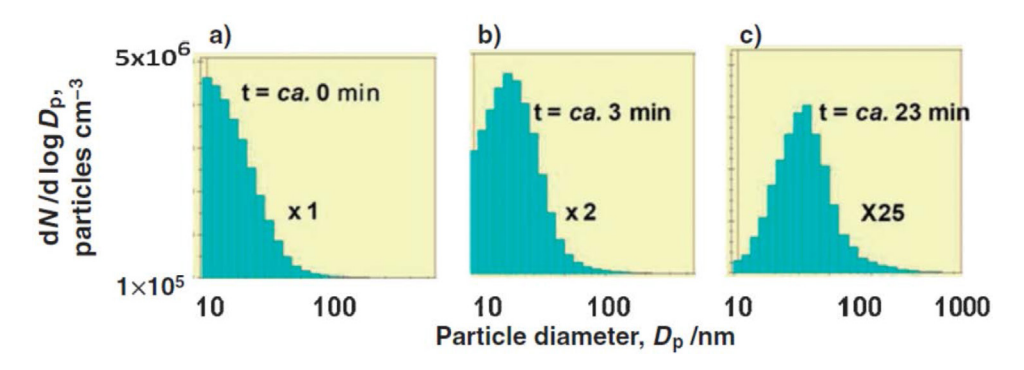


Figure 7. Particle size growth over time in a cloud chamber (air at 50 °C and 12% RH) after illumination at t = 0 by a 0.4 J nanosecond KrF laser (248 nm) at 10 Hz during 30 s. Vertical axes are magnified by $\times 2$ in (b) and $\times 25$ in (c). Reprinted from Yoshihara *et al* (2012), with the permission of AIP Publishing.

$$N^+ + O_2 \rightarrow NO + O^+$$

$$N_2^* + O^\centerdot \to NO + N^*$$

$$N^* + O_2 \rightarrow NO + O^*$$
.

For O₃:

$$O^{\centerdot} + O_2 + M \rightarrow O_3 + M.$$

And for NO₂:

$$NO + O_3 \rightarrow NO_2 + O_2$$
.

Considering the chemistry occurring at these high NO_x and O_3 concentrations leads to (Seinfeld and Pandis 2006):

$$NO_2 + O_3 \rightarrow NO_3 + O_2$$

$$NO_2 + NO_3 + M \rightarrow N_2O_5 + M$$

$$NO_2O_5 + H_2O \rightarrow 2HNO_3$$

and thus local HNO₃ concentrations in the filaments in the ppm range (Petit et al 2010). Compatible levels of HNO3 were, moreover, very recently confirmed by mass spectrometry directly in the plasma filament (Valle Brozas et al 2016). As briefly mentioned above, an alternative pathway to create HNO₃ is the direct oxidation of NO₂ by OH radicals, which can be released, for example, by the photodissociation of ozone and reaction of the resulting singlet oxygen with H₂O. Recent measurements from Camino et al (2015) using supercontinuum based cavity enhanced absorption spectroscopy (SC-CEAS) allowed to measure the production of ozone, NO₂, and NO₃, in a laser filament, in real time. While the concentrations of NO₂ and O₃ are consistent with the previous ones, they could quantify for the first time the presence of NO₃, and found roughly a concentration 1000 times lower than that of NO_2 .

Such high concentrations (1000–10000 times the typical natural concentration (Chiwa *et al* 2008) is known to contribute to particle stabilization besides H₂SO₄ in natural conditions. The equilibrium of aqueous solution particles with an atmosphere containing a highly soluble trace gas can be described by the Köhler theory (Kohler, 1936, modified here following Laaksonen *et al*, 1998). The equilibrium between the gas phase and liquid phase of the water and HNO₃ components in

the binary HNO₃–H₂O condensation is determined by the following relation (Rohwetter *et al* 2011, Kasparian *et al* 2012):

$$p_{\infty,i}(T,m_j) = p_{\text{sat},i}(T,m_j) \exp\left(\frac{4\sigma(T_{\text{p}},m_j)v_i(T_{\text{p}},m_j)}{k_{\text{B}}TD_{\text{p}}(T_{\text{p}},m_j)}\right)$$

where $k_{\rm B}$ is the Boltzmann constant, $D_{\rm p}$ the particle diameter and the index i stands for the species H₂O or HNO₃. $p_{\infty,I}$ (T, m_i) denotes the partial pressure of species i at a temperature T in the atmosphere, m_i its mass in the liquid phase, $p_{\text{sat},I}$ (T, m_i) its partial pressure at saturation over a flat liquid phase of same composition, as defined by the set of masses m_i , v_i (T_p, m_i) denotes its partial molecular volume, and $\sigma(T_p, m_i)$ is the surface tension of the solution for a particle at temperature $T_{\rm p}$. The saturation value S (or RH in case of $i = {\rm water}$) for which a particle of diameter D_p is at equilibrium is thus represented here by $S_{\text{equ}} = p_{\infty,I}(T, m_j)/p_{\text{sat},I}(T, m_j)$. The above equations, in which the exponential term results from the Kelvin effect, stems from the minimization of the Gibbs energy. Besides water and the highly soluble gas, the particular form of extended Köhler theory used here considers a mixed liquid phase containing additionally a fixed amount of a fully dissolving nonvolatile substance (Clegg et al 1998, Clegg and Wexler 2011, Dutcher et al 2010), represented by an ammonium nitrate nucleus of some nm in diameter. It is therefore a ternary nucleation process HNO₃-NH₄NO₃-H₂O. Solving the set of equations for different values of HNO₃ concentrations in the gas phase yields the Köhler plots of figure 9.

These curves define, for the considered conditions, the relative humidity ensuring the stability of a particle as a function of its diameter. The addition of HNO₃ drastically affects the shape of the Köhler curves. In particular, the RH required to activate particles between 50 nm and 2 μ m approximately, decreases significantly. As a consequence, two ranges of stable sizes (corresponding to positive slopes of the Köhler curves) emerge at RH values well below 100%, around 20-30nm and several micrometers, respectively. At $T = 279 \,\mathrm{K}$ a concentration of 4ppm of HNO₃(g) is sufficient to stabilize micrometer sized droplets for widely sub-saturated conditions, i.e. 75% RH. Photochemical stabilization of droplets in sub-saturated conditions following the ternary HNO3-NH4NO3-H2O condensation route appears therefore as plausible to explain the observed filament induced condensation in diffusion cloud chambers.

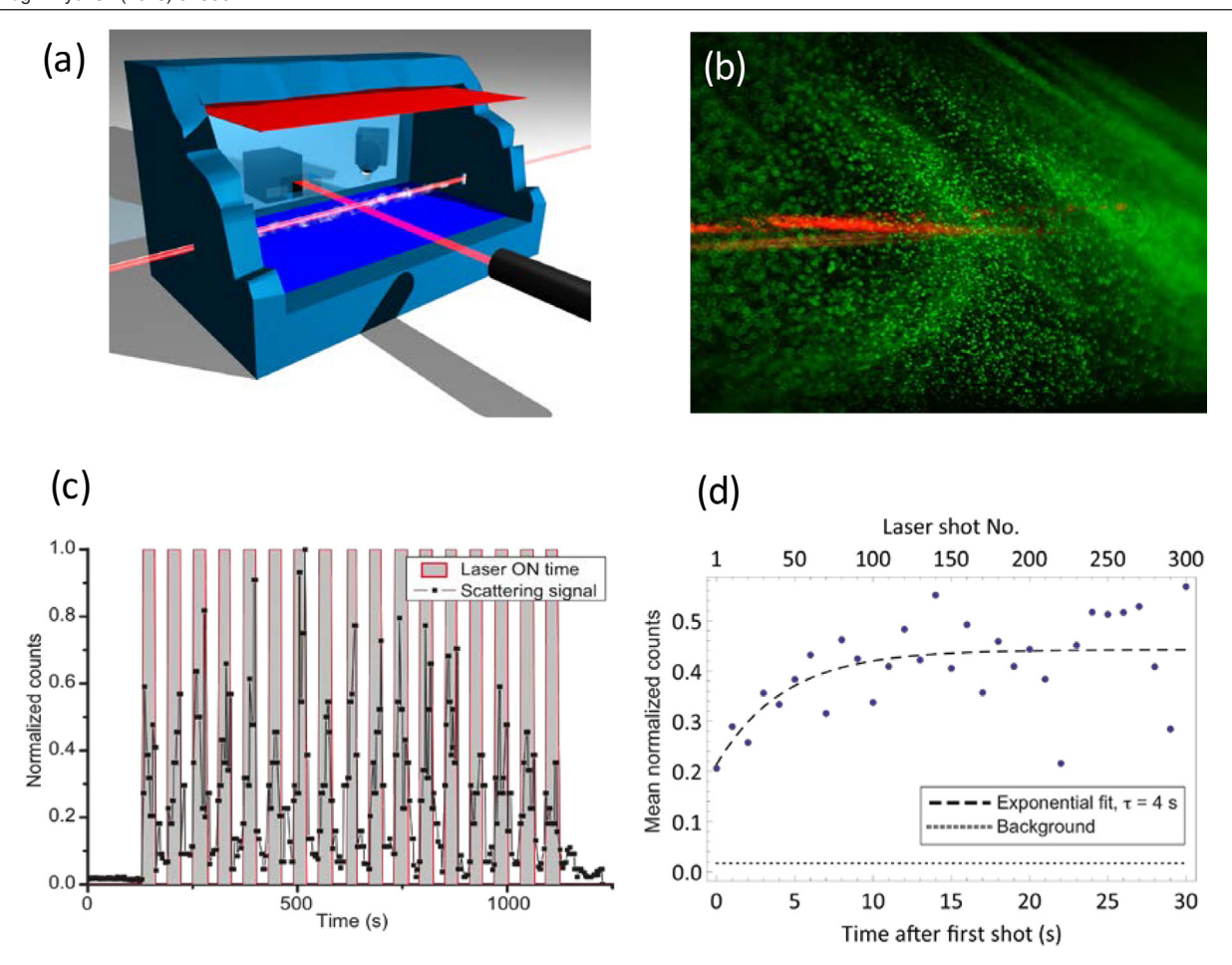


Figure 8. Laser Filament induced water condensation in a sub-saturated diffusion cloud chamber (T = 60 °C, RH = 75%–85%). (a) Schematic of the experiment: chamber with cooled bottom and heated top plate including a liquid water reservoir, laser filaments, scattering laser (532 nm cw) and CCD imaging device to record Mie scattering, and Malvern particle sizer. (b) Real color image of the droplets produced by the laser filaments (c) high reproducibility of the effect over repeated laser on/off cycles of 300 laser shots each and (d) increase of the droplets number until saturation due to depletion of the diffusion limited available water content in air. Reprinted by permission from Macmillan Publishers Ltd: Nature Photonics Rohwetter *et al* (2010), Copyright (2010).

An intriguing question is whether laser filaments were able to nucleate aerosols directly from the gas phase, without the initial presence of background nanometric nuclei. To this end, an extensive measurement campaign was performed at the large-scale (85 m³) aerosol and cloud chamber AIDA (Aerosol Interaction and Dynamics in the Atmosphere) in Karlsruhe (Möehler et al 2003, Schnaiter et al 2012) under illumination by the Teramobile. Temperature, relative humidity, trace gas levels, and laser power were varied systematically, and this with extremely low background particle concentration (<0.1 cm⁻³). Laser filaments nucleated particles from the gas phase that grew to sizes of 3–130 nm during the experiment. With ambient air in the simulation chamber, production rates up to 10⁹ s⁻¹ cm⁻³ were observed (Saathoff et al 2013). Although these rates depend on the actual experimental conditions, we may note that it lies 5-6 orders of magnitude above the 10⁴–10⁵ cm⁻³ s⁻¹ observed in industrial atmospheres (Kulmala et al 2004), but of course only within the filament volume. The fresh particle formation in synthetic air shows an exponential increase with water concentration. This points out the important role that water molecules play in the formation of clusters (Kurten et al 2007)

and in the formation of reactive species like OH radicals in the plasma, which have the ability to generate condensable species like inorganic acids or oxidized organic molecules (Fresnet *et al* 2002). Notice also that particle formation was observed even in water vapor containing noble gases, like humid argon. Although the chamber was kept as clean as possible, this observation was interpreted as the action of some traces of organic contamination.

Without additional trace gases added, the typical particle diameters lie between 5 and 20 nm. At 97% relative humidity and 283 K, also larger particles with a diameter of about 100 nm were observed. As expected, the formation and growth of new particles was significantly enhanced by the presence of ppb traces of NH₃, SO₂ or volatile organics like toluene or α -pinene. Interestingly, similar observations and related interpretation were recently reported in the framework of the CLOUD experiment at CERN (Kirkby *et al* 2016, Trostl *et al* 2016) where an ultra-pure cloud chamber was irradiated by a proton synchrotron, for simulating the effects of galactic cosmic rays (GCR) on the Earth atmosphere.

In addition to photochemical stabilization, it was shown that filaments induce significant turbulence by heat deposition

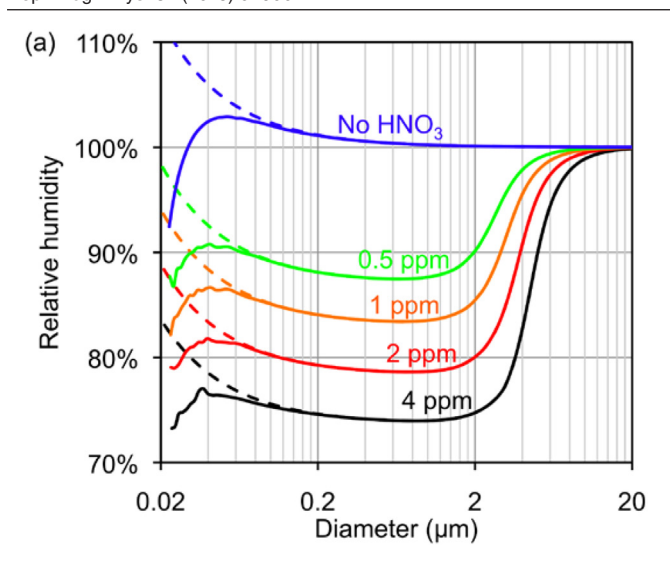


Figure 9. Simulation of the droplet stability conditions after the laser shot. Köhler plots for a droplet density of $1000\,\mathrm{cm^{-3}}$, at $T=279\,\mathrm{K}$ and $1013.25\,\mathrm{hPa}$. Curves from top to bottom correspond to 0, 0.5, 1, 2, and 4 ppm initial concentration of gaseous HNO₃; solid lines: droplets including a $15\,\mathrm{nm}\,\mathrm{NH_4NO_3}$ core; dashed lines: droplets without salt core. Reprinted by permission from Macmillan Publishers Ltd: Nature Communications Henin *et al* (2011), Copyright (2011).

and shockwave expansion (Vidal *et al* 2000, Cheng *et al* 2013, Jhajj *et al* 2014, Lahav *et al* 2014) in the plasma, which strongly enhances turbulent mixing, and thus particle growth in diffusion cloud chambers (Ju *et al* 2012, 2013a, 2013b, 2014, 2016). This effect was thoroughly characterized, by investigating the influence of the energy, pulse duration (Sun *et al* 2016) and repetition rate of the filamenting laser (up to 1 kHz), focusing geometries, relative humidity and temperature of the involved mixing air masses, etc.

In figure 10, the effect of laser induced turbulence is clearly observed. While short filaments create vortices between the filament and the bottom cold plate (separated by 1 cm), with air speeds as much as 15 cm s⁻¹, longer and less intense filaments generate weaker laminar drafts. Since in the diffusion chamber a strong vertical temperature gradient is present (10–15 °C cm⁻¹) the laser generates efficient turbulent mixing of the cold and warm air masses, with associated supersaturations up to $S_w \sim 1.3$ relative to water and $S_i \sim 2.1$ relative to ice. The cooling rates of the related air parcels lead to extremely fast condensation and particle growth. Because of the low temperature of the bottom plate $(-46 \, ^{\circ}\text{C})$ to $-30 \, ^{\circ}$ °C) and of the air above it, water vapor condensation led to ice crystals formation, which eventually fell as snow on the bottom plate. After irradiating the cloud chamber during 60 min with ~8 W average laser power (8 mJ, 1 kHz, 30 fs) some 50 mg of snow was collected on the cold bottom plate (Liu et al 2016). Ionic chromatographic analysis of the snowflakes revealed a significant amount (~500 ppm) of NO₃ ions, which is consistent with the HNO₃-H₂O photochemical pathway identified in air. However, experiments were repeated in humid argon and humid helium, which also successfully yielded snowfall in similar concentrations. In particular in humid Helium, the NO₃ ions in the snowflakes was 100 times lower than in air, pointing to other nucleation processes than the nitric acid route. One possibility could be, as observed at AIDA in the case of humid argon, a possible oxidation of organic traces contaminant.

An interesting observation is the variation of the ice crystal shape while moving the position of the filament height. It is well known indeed that the crystal structure depends on the growth speed and the temperature (Pruppacher and Klett 1997, Libbrecht 2006). The dendritic leaf-like shape observed (figures 11(b) and (c)) when the laser beam was at 0.6 and 1.5 cm from the bottom at -46 °C suggest that the ice crystal formation occurred between -15 °C and -25 °C. In opposite, the almost graupel-like structure of figure 11(d) suggests higher initial temperatures, which is in line with a higher bottom temperature (-30 °C) (Ju *et al* 2013). These observations aimed at demonstrating that the ice particles were produced in air rather than freezing while already in contact with the cold bottom plate.

3.3. Scaling-up with sub-Petawatt lasers

With the spectacular increase in peak and average powers of today's lasers, the question of the applicability of the laboratory experiments to the real scale atmosphere may be addressed. While the Teramobile system, for instance, provide Terawatt (10¹² W) peak and some watts average powers, the current and near future planned laser facilities aimed at delivering 10–100 Petawatt (10¹⁶–10¹⁷ W) and multi-kW average powers (Bashinov *et al* 2014); this will correspond to 1000–10000 Teramobile systems coherently combined together!

A first step towards scaling up to these extreme levels was realized by performing laser induced water condensation at the 0.1–0.2 PW levels at the HZDR-Rossendorf (Petrarca *et al* 2011), ALLS-Montreal (Matthews *et al* 2013) and FLAME-Frascati facilities (Petrarca *et al* 2014).

The aerosols/water condensation experiments presented in figure 12 were carried out with the DRACO laser from the Forschungszentrum Dresden-Rossendorf, a Ti:Sa chirped pulse amplification (CPA) chain providing up to 3 J, 100 TW pulses of 30 fs duration, at a repetition rate of 10 Hz and a central wavelength of 800 nm. After ~7.5 m of propagation, up to 900 filaments were generated. From this location, the filamenting beam propagated through an open diffusion chamber filled with ambient air. The temperature and RH in the chamber were controlled by a heated water reservoir at its top, and a fluid circulator at a temperature of -15 °C on its bottom. During the measurements, the RH ranged within 75%–95%, at a local temperature of 8-12 °C. The aerosol generation was characterized by a nanoparticle sensor (Grimm Nanocheck 1.320), which counts and evaluates the median diameter of nanoparticles between 25 and 300 nm. While the number of filaments saturated, the concentration of the generated particles dramatically increased above 0.5 TW cm⁻². Fitting the curves with a power law function leads roughly to a fifth power dependence, which could be interpreted as the number of photons required for the O₂ photodissociation, releasing atomic oxygen radicals for oxidating e.g. VOCs in condensable species (simultaneous measurements of ozone confirmed this hypothesis). The contribution beyond 0.5 TW cm⁻²

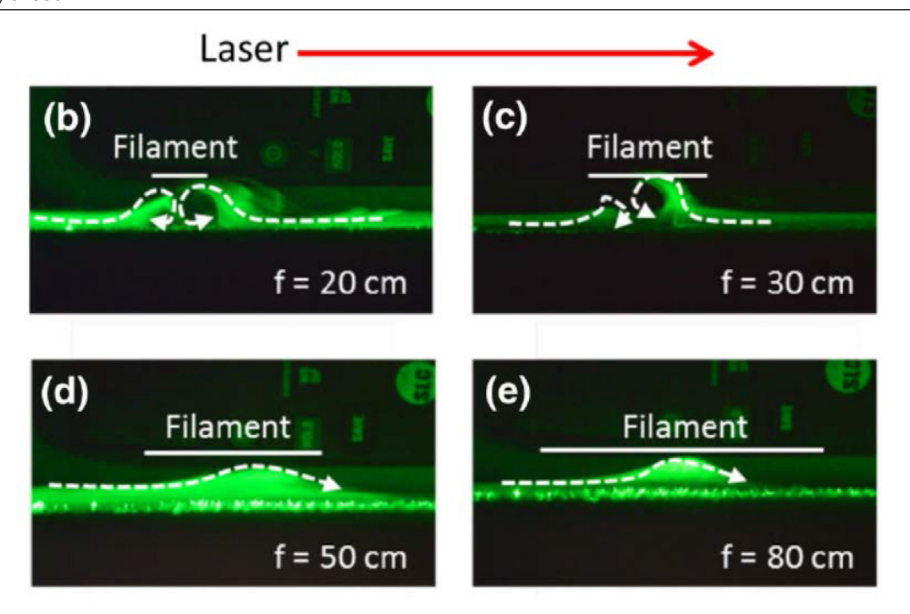


Figure 10. Laser induced turbulent flow around filaments produced with different focal length lenses. From Ju et al (2014). With permission of Springer.

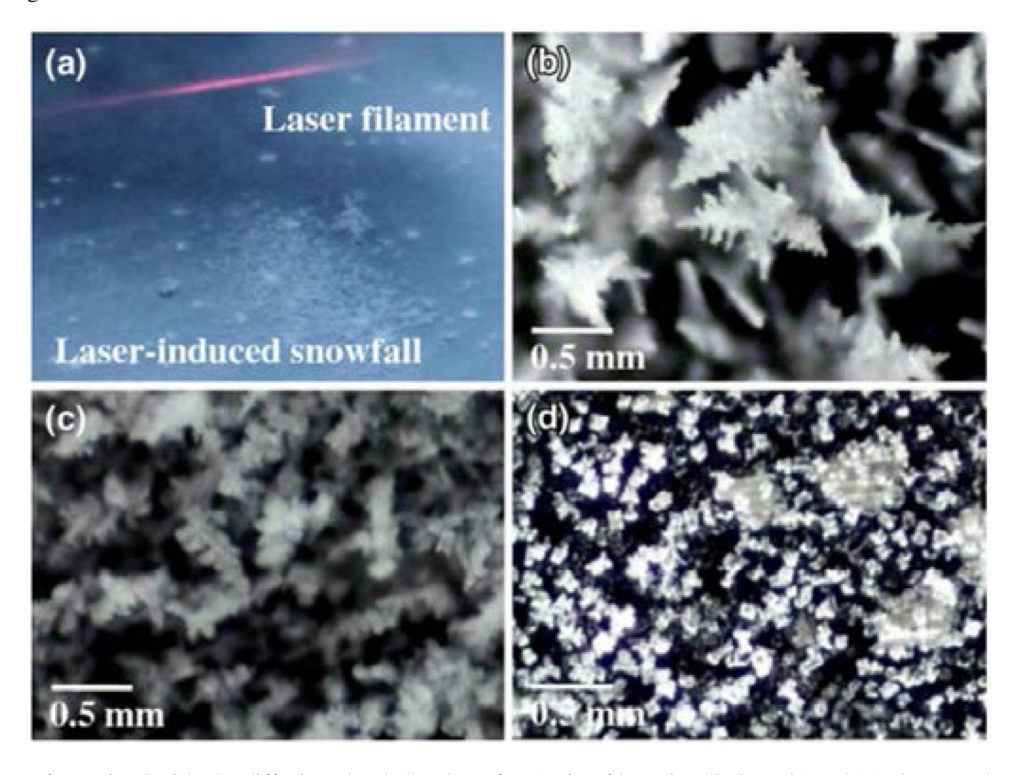


Figure 11. (a) Snow formation inside the diffusion cloud chamber after 1 min of laser irradiation, (b) and (c) close-up shots of the snow heap when the height of the laser was changed from $0.6 \, \text{mm}$ and $1.5 \, \text{cm}$, respectively. (d) Close-up shot of the ice particle heap when the temperature of the bottom base plate was set at $\sim -30 \, ^{\circ}\text{C}$ ($-46 \, ^{\circ}\text{C}$ for (a)–(c)) and the height of the laser axis was set at $1.0 \, \text{cm}$. From Ju *et al* (2013). With permission of Springer.

therefore points to the contribution of the whole beam rather than from the filaments. Once the intensity in the photon reservoir is sufficient, the whole beam photodissociates and photoionizes the air species, without the usual intensity clamping occurring in the filamentary structures. At 1 TW cm⁻², it was calculated that 95% of the laser energy was contained in the photon bath, because of the filament number saturation phenomenon. These experiments conclude that (1) filamentation is not necessary to condensate or nucleate

aerosol particles with NIR ultrashort laser beams, and (2) the efficiency of the condensation process can increase significantly if average intensities exceeding 0.5 TW cm⁻² can be produced and maintained in the whole beam cross-section.

The particle production from NIR 100 TW-class lasers could be further enhanced by adding a synchronized, 250 mJ nanosecond laser (collimated) at 266 nm, which produced no particles by itself. The experiment was performed at the ALLS laser facility from the INRS-Montreal. A doubling of

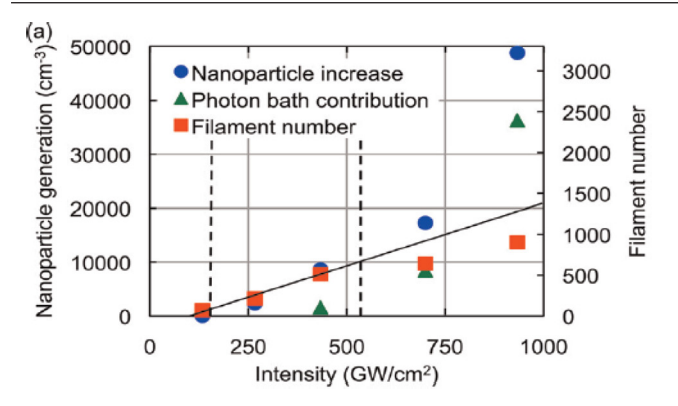


Figure 12. Evolution of the number of filaments and of the number of nanoparticles generated by the laser as a function of incoming beam intensity. Reprinted from Petrarca *et al* (2011), with the permission of AIP Publishing.

the photo-production rate by the low intensity UV laser as compared to the 100 TW NIR laser alone was observed, and interpreted as the production of OH radicals from the ozone produced by the NIR beam (Matthews *et al* 2013). More precisely:

$$O_3 + h\nu_{UV} \rightarrow O(^1D) + O_2$$

$$O(^1D) + H_2O \rightarrow 2OH.$$

OH then efficiently oxidizes NO_2 or VOCs to produce soluble species and stable binary or ternary condensation processes. The quantitative analysis of the process yielded an estimation of the OH radical production rate within the filament volume: $10^{13} \, \mathrm{cm}^{-3} \, \mathrm{s}^{-1}$, i.e. 7 orders of magnitude higher than in the natural atmosphere. This high production rate is in line with the recent measurements of the OH fluorescence in filaments by the group of S L Chin (Yuan *et al* 2013), in spite of OH's extremely fast chemical reaction rate constants.

Scaling up to real atmosphere's macroscopic effects requires not only increasing the laser intensity and average power, but also the process efficiency, as shown, for example, above. Clearly, UV is an attractive spectral region, as already pointed out by Wilson with UV-lamps and the group of K Yoshihara with nano-second excimer lasers. A natural question arose then about the use of filamenting, ultrashort, high intensity UV laser pulses. Developments performed in Göttingen (Nagy et al 2009), New Mexico (Feng et al 2014, Rastegari et al 2016) and Moscow (Zvorykin et al 2013, Zvorykina et al 2015) led to high intensity ultrashort lasers in the deep UV (266 nm and 248 nm), which generate filaments in air. The first UV laser filaments based water condensation experiment was performed with a femtosecond laser seeded KrF laser at 248 nm system delivering 11 mJ in 110 fs pulses (0.1 TW), or 25 mJ in 700 fs pulses in Göttingen. With an experimental diffusion cloud chamber identical to the one used at ALLS, 5-10 times higher production rates of nanoparticles was observed as compared to the 100 TW NIR laser (Joly et al 2013). The concentration of particles between 25 and 300 nm size reached some 300 000 cm⁻³ after some minutes irradiation, i.e. several hundred times the background concentration. This spectacular efficiency is interpreted by the

lower non-linear order required to ionize and photodissociate the air species: 1 photon at 248 nm carries the energy of about 3 photons at 800 nm. Additionally, 248 nm efficiently produces OH radicals from ozone, as described above. Therefore, the combination of UV radiation and high intensity allows for taking advantage of non-linear pathways leading to N_2 , O_2 , H_2O dissociation and ionization, but simultaneously linear photochemical reactions with their products. Since NO_x and ozone was also measured in this experiment, the nitric acid pathway could be confirmed also in the UV. However, comparison with a 20 ns, 350 mJ KrF laser showed that it also produces particles, as previously reported in reference (Yoshihara et al 2012) without NO_2 production. This confirms the different pathways followed by nanosecond UV lasers, e.g. via H_2O_2 , as proposed by K Yoshihara.

High intensity (TW class) UV lasers appear therefore as an attractive option for laser condensation experiments. However, production yield is not the only parameter for applications in the real atmosphere. Long distance propagation (several hundreds meters, up to some kilometers) and filamentation control are as important. In this respect the deep UV spectral range suffers of significant drawbacks. In particular, the λ^{-4} dependence of Rayleigh scattering and the ozone absorption (Hartley bands) can significantly reduce the operational range of deep UV lasers (only 25% transmission at 248 nm through 1 km of air containing 50 ppb background ozone).

3.4. Laser induced aerosol/water condensation in real scale: Field experiments

A decisive advantage of the Teramobile system is its ability to carry out real scale atmospheric experiments (Kasparian *et al* 2003). In this context several field campaigns were organized over a long, free horizontal path in Geneva.

The first campaign was carried out in 28 runs, for a total of 133h of records from fall 2009 to spring 2010 on the bank of the Rhône River (46°12′ North, 6°5′ East, 380 m above sea level). This location was chosen to get the benefit from the relatively warm water flow from the Lake of Geneva acting as a heat buffer, locally increasing the RH. Data were acquired in a wide variety of atmospheric conditions: RH from 35 to 100% and temperature between 2 and 36 °C. Furthermore, experiments during the day and the night ensured that both phases of increase and decrease of temperature and RH have been recorded. The laser was operated continuously and provided up to 160 mJ pulses of 240 fs duration at a central wavelength of 800 nm and a repetition rate of 10 Hz. The beam was expanded to 10cm diameter and slightly focused $(f \sim 20 \text{ m})$ by a built-in expanding telescope. At the nonlinear focus, that is, after ~15 m of horizontal propagation 1.2 m above ground, the beam generated some 10 filaments in the atmosphere. Filamentation spanned over typically 15-20 m, as inferred from both visual observation on a screen and the emission of a shockwave recorded by a microphone. As displayed in figure 13 filament induced water condensation was observed in the real atmosphere for every size class, from nanoparticles to 10 μ m (Henin et al 2011). The size distribution was thoroughly analyzed and cross-checked using 5

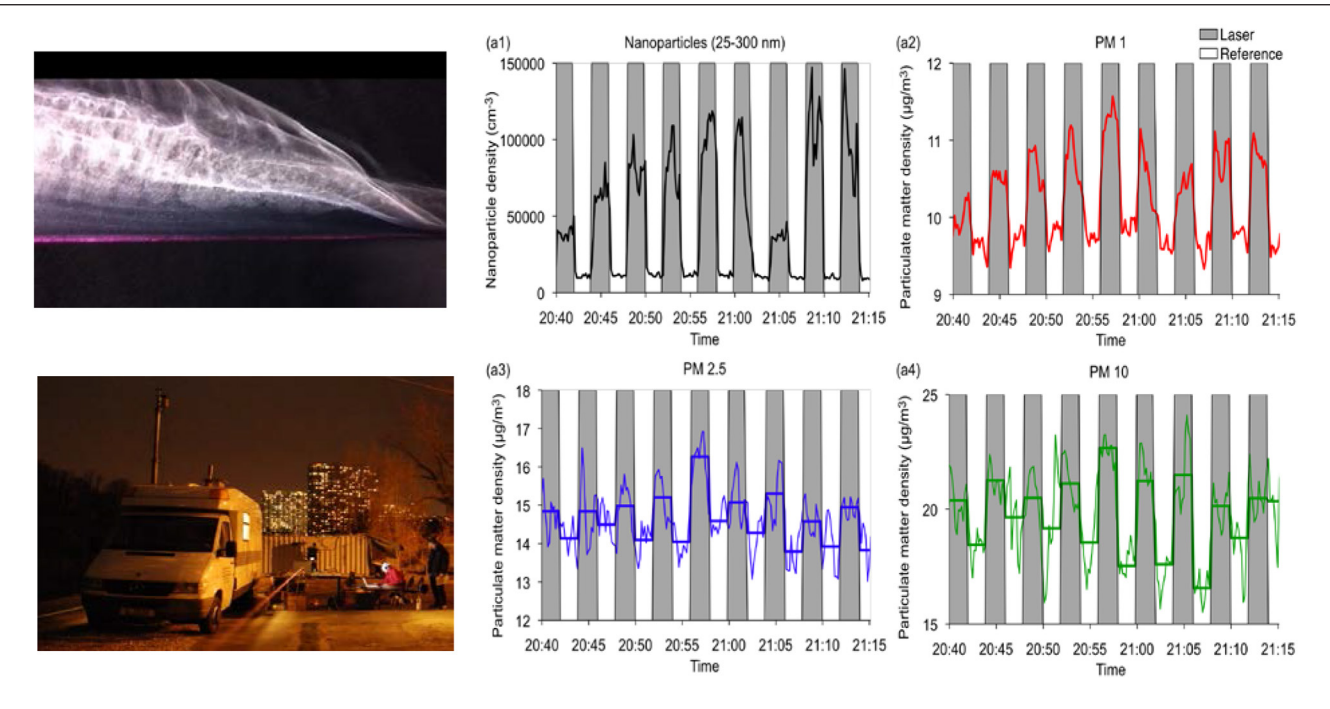


Figure 13. Left upper: equipment test in the laboratory showing filament induced condensation. Left lower: the Teramobile system located in the field, along the Rhone River in Geneva, and a van based air analyzer facility provided by the Hochschule Dusseldorf. Right: efficient particle production for every size class directly in ambient air (shaded: laser on, unshaded: laser off). Reprinted by permission from Macmillan Publishers Ltd: Nature Communications Henin *et al* (2011), Copyright (2011).

particle sizers (two Grimm Nanocheck 1.108, two Grimm 1.107, and one TSI Model 3007). As observed in the previous laboratory experiments, the most spectacular laser effect is seen for nanoparticles (25-300 nm) where number densities as high as 150 000 cm⁻³ in the filament volume are recorded (for 75% RH, 13 °C). Although weaker, laser induced particle generation is also observed for larger sizes, even if particle growth to micrometric sizes usually requires longer timescales than the 5 min integration time used in the comparative runs. A Student test was systematically applied to verify that all the reported results are statistically relevant ($\alpha < 0.01$). Local concentrations of ozone of ~200 ppb and NO₂ of 25 ppb, generated by the filaments, as well as NO₃ ions in the ion-chromatography analysis of the particles confirmed the occurrence of the HNO₃-H₂O pathway in the ambient air. The large data set acquired during this 6 months campaign allowed to identify correlations between the particle generation yield and the atmospheric conditions. A clear positive correlation is observed for smaller particles with RH, and for large particles with the total water vapor content, while negative correlation is observed for nanoparticles with temperature. These behaviors are consistent with the particle nucleation and growth models in the natural atmosphere (Pruppacher and Klett 1997).

A second field campaign in Geneva was carried out in summer 2014 using additional diagnostics to analyze in real time the composition of the generated particles, which could not be performed before. To this end the group of U Baltensperger (PSI Villingen, CH) engaged a field compatible Aerodyne high resolution time of flight aerosol mass spectrometer (AMS) (DeCarlo *et al* 2006, Canagaratna *et al* 2007). Briefly, the AMS continuously samples particles from ambient air

 $(0.8\ 1\ min^{-1})$ through a 100 μm critical orifice into an aerodynamic lens (2 torr). The particles are then focused into a narrow beam and accelerated to a velocity that is inversely related to their vacuum aerodynamic diameter. The particle beam can be modulated by a spinning chopper wheel, yielding size-resolved mass spectra. The particle ionization on a resistively heated surface (600 °C, 10 – 7 torr), where the non-refractory components flash vaporize, are ionized by electron impact (70 eV) and are detected by time-of-flight mass spectrometry. The AMS can detect most atmospherically-relevant species except for black carbon, mineral dust and water droplets. Mass spectra are analyzed and quantitatively split into e.g. nitrate, sulfate, ammonium, and organics using the standard fragmentation table-based analysis of Allan *et al* (2004).

The chemical composition and the size distribution of aerosols generated by femtosecond-Terawatt laser pulses in the outdoor atmosphere was analyzed in real time using the AMS (figure 14). It showed that nitric acid condenses in the form of ammonium nitrate, and that oxidized volatile organics also contribute to particle growth. These two components account for two thirds and one third, respectively, of the dry laser-condensed mass. They appear in two different modes centred at 380 nm and 150 nm. The number concentration of particles between 25 and 300 nm increases by a factor of 15.

In particular, the concentration of NO₃ and NH₄ observed in the laser-induced aerosols (50% and almost 20% of the dry condensed mass, respectively, i.e, a total contribution close to 70%) shed new light on the previously inferred binary water—HNO₃ condensation under laser illumination. The hygroscopic HNO₃ previously identified to assist the condensation of water is not only condensed, as initially expected, as nitric

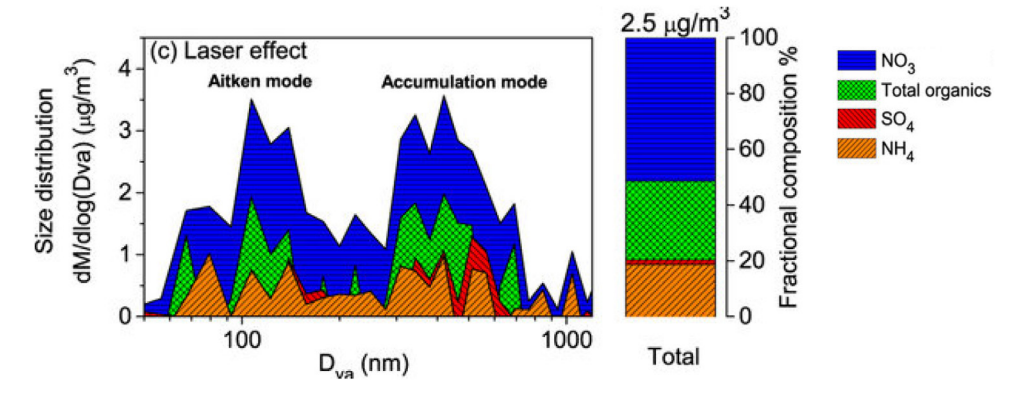


Figure 14. Mass distribution of the measured condensable species within the particles (dry mass): mass difference between irradiated and non-irradiated. Reprinted by permission from Macmillan Publishers Ltd: Nature Scientific Reports Mongin *et al* (2015), Copyright (2015).

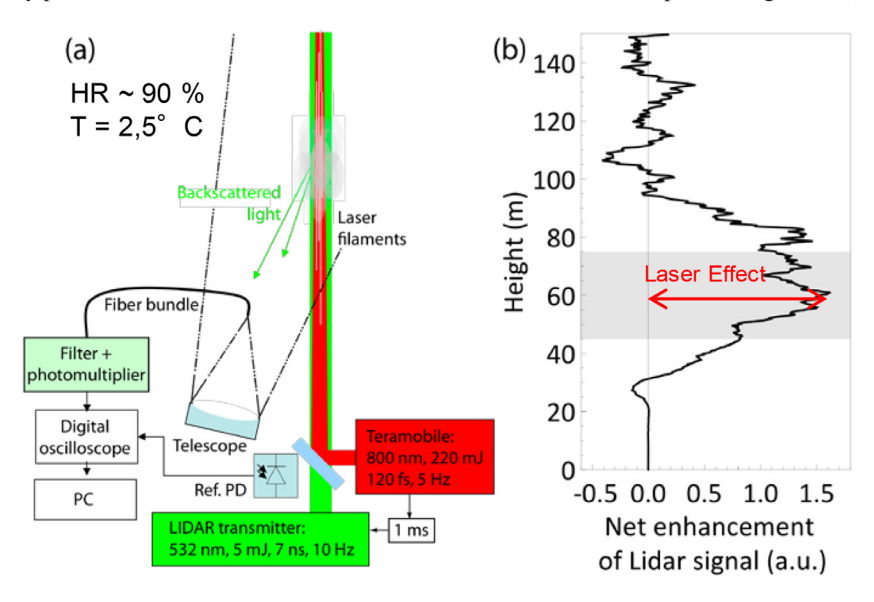


Figure 15. Laser-induced condensation experiment in the atmosphere. (a) Experimental set-up. The Teramobile laser (red) is fired 1 ms before the LIDAR pulse (green) measuring the aerosol content of the atmosphere. (b) Time-averaged relative increase of the Mie backscattering coefficient β_{Mie} measured with and without firing the terawatt laser. The signal enhancement at the height of the filaments (the most active filamenting region at 45–75 m is shaded) is a clear indication for filament-induced condensation. Reprinted by permission from Macmillan Publishers Ltd: Nature Photonics Rohwetter *et al* (2010), Copyright (2010).

acid in a binary mixture with water, but rather as hygroscopic ammonium nitrate through the reaction (Seinfeld and Pandis 2006):

$$NH_3 + HNO_3 \leftrightarrow NH_4NO_3$$
.

NH₃ is typically available as background trace gas in the summer sub-urban atmosphere of the experiment location in amounts of several μg m⁻³ (Thöni *et al* 2004). This concentration is comparable with the laser-condensed mass of NH₄⁺ suggesting that the laser-induced condensation relies on the condensation of pre-existing ammonia together with HNO₃. The latter is generated via the interaction of NO_x produced by the multi-photon ionization of N₂ with O₃ or ·OH radicals, both produced by the multiphoton absorption and photolysis of O₂. The very low efflorescence of ammonium nitrate and the high quantities of NH₄NO₃ in the laser condensed mass suggest that there is always water in the laser induced aerosols. Besides, it validates *a posteriori* the ad hoc introduction of ammonium nitrate for modelling the growth of laser-induced particles (Henin *et al* 2011, Rohwetter *et al* 2011).

Besides ammonium nitrate, the laser mainly condenses organics (28% of the dry mass) in the real atmosphere. The amount of organics condensed by the laser seems to be driven by its ability to create an oxidative atmosphere. The absolute amount slightly below 1 μg m⁻³ of organics condensed by the laser constitutes a few percent of the total concentration of VOCs available in a typical urban atmosphere (Derwent et al 2014), confirming the VOC availability for laser-induced oxidation and condensation. The filament plasma produces a concentration of ·OH radicals much higher than in normal atmospheric conditions, leading to efficient oxidization of the available organics. The resulting highly oxygenated, low volatility organics then efficiently condense onto particles with a high oxygenation state comparable to that of α -pinene particles after exposure to 500 ppb of O₃ half a day (Shilling et al 2008, Ng et al 2010, 2011). This very fast oxidization produces an ultrafast 'aging' for secondary organic aerosols (SOA), which become efficient CCN. This process is well known in the natural atmosphere, but usually occurs over timescales like hours or even days.

The experiments carried out in conditions closest to real world applications were realized in Berlin in 2010 (Rohwetter et al 2010), where the particles generated by filaments at 50-100 m altitude in the atmosphere were measured in real time with a synchronized Lidar. More precisely, a green nanosecond Nd: YAG laser was fired twice, 1 ms and 100 ms after the Teramobile laser pulses, and the backscattered light from aerosol particles was recorded with a Lidar receiver (consisting of a 20 cm in diameter telescope, a 532 nm spectral filter, a photomultiplier tube and a fast digital transient recorder). In this way, comparison between the Mie backscattered signals originating from particles produced by the laser filaments (1 ms probe delay) and from background aerosols (100 ms probe delay) led to the direct measurement of altitude-resolved particle generation (as shown in figure 15(b)). Because of the atmospheric motion (wind), the dispersion, the small probed volume, and the remote detection, these measurements constituted a real challenge. Nevertheless, a faint but measurable haze of about 50 m thickness generated by laser filaments, centered 70 m above ground was detected for the first time in the real atmosphere. The signal increase corresponded to a local enhancement of volume Mie scattering coefficients (Bohren and Huffman 1998) by a factor of 20 within the filaments, from $\beta_{\text{Mie}} = 10^{-6} \text{ m}^{-1} \text{ sr}^{-1} \text{ to } 2 \times 10^{-5} \text{ m}^{-1} \text{ sr}^{-1}$ (statistically significant with $\alpha < 0.01$). Notice that the volume backscattering coefficient β is an average over all aerosol sizes (and their related Mie scattering cross-sections), so that a number concentration cannot be directly derived from it without a priori assumptions or additional information (Kasparian et al 1998a). While the campaign spanned over several weeks, the remote laser condensation effect was only observable for favorable atmospheric conditions, i.e. RH > 90% and wind speeds $\sim 3-5 \text{ m s}^{-1}$.

The vertical profile in figure 15 illustrates the surgical precision with which aerosols can be produced by laser filaments, unlike spread of chemicals. In the shown profile, the location in which condensation is observed perfectly matches the location of the laser filaments. Control of the filamentation onset and filament length can be controlled by spatial focusing using a large aperture sending telescope (here 20 cm diameter) and by temporal focusing by impinging a negative chirp to the launched laser pulse, and leaving the propagation air perform the pulse compression (by dispersion) for a pre-defined distance (Bergé *et al* 2007, Couairon and Mysyrowicz 2007).

3.5. Potential applications: precipitation modulation and albedo control

Perspectives opened by the present basic research results clearly imply a certain level of imagination or speculation. The first possible application of laser induced condensation is related to modulation of precipitations, e.g. rain, hail and snow. Considering the modest energies at play, only 'catalytic' effects from the laser photons can be envisaged. This relates in the present context to the generation of nano-sized condensation nuclei (i.e. a limited amount of involved molecules), which eventually grow into larger micrometer sized droplets if and when the atmospheric conditions are favorable.

Because of this dependence on the transport and evolution of the related seeded air parcels (e.g. cooling, mixing with other air masses, etc) the assessment of the efficiency of any cloud seeding method always remains unclear, statistically difficult to assess, and controversial (NRC 2003, Qiu and Cressey 2008, Geerts *et al* 2010, Miao and Geerts 2013). The major advantage of the laser based method is the spatial and temporal precisions with which CCN can be produced, as demonstrated above (figure 15). In this way, seeding could be realized only at altitudes and locations where the atmospheric conditions are favorable (RH, T, but also air mass trajectories simulations) for maximizing the effect. The 'maturity' of an air mass to be seeded or not could even be assessed by the same laser based system (Rairoux *et al* 2000, Bourayou *et al* 2005, Xu and Chin 2011).

An important aspect to consider is the spectacular development of Yb based ultrashort lasers, where TW peak powers with kW average powers are becoming commercially available (Metzger 2016). This would lead to a factor 100 in the CCN particle production as compared to the current measurements with the Teramobile (figure 13). Another interesting aspect is that laser generation of CCN might be used to prevent precipitation instead of promoting it. Rainfalls indeed occur when the droplets are able to grow to typically 100 μ m, and start to efficiency coalesce in mm rain drops while falling. If sufficiently large numbers of CCN are injected in a saturated air mass, the available water will be distributed on the numerous nuclei, so that none of the droplets will reach the critical size for coalescence. Such a scenario could be implemented, for instance, in regions affected by the well-known rain shadow effect (e.g. Atacama desert in Chile, Sierra Nevada in the USA etc). Briefly, warm and moist air from the ocean is blocked on the coast by a mountain creating orographic lifting and thus adiabatic cooling towards the top of the mountain. The fast cooling produces water condensation on natural CCN (e.g. marine aerosols) leading systematically to precipitation on the same side and the top of the mountain. On the leeward side the dried air descends and gets warmer, leading to arid regions, i.e. the rain shadow side. By injecting systematically more CCN on the windward side with, e.g. a laser based system, water vapor would be trapped on large amounts of aerosol particles and transported on the leeward side. The gravity (lee) waves could then produce revivals of the adiabatic cooling and condensation up to the coalescence critical size leading to precipitation on the arid regions. Localized laser seeding may also prove useful to attenuate dramatic flooding or prevent hail from damaging cultures.

Besides precipitation, cloud condensation can find applications in increasing the albedo of the Earth and reduce radiative forcing, i.e. global warming, or in hiding objects behind some localized haze curtain for defense purposes (Coble 1997). Concerning the geo-engineering side, several scenario have been proposed using chemical seeding to generate a 'cloud parasol' in the stratosphere. The most famous is the proposal of seeding sulphur compounds, like (SO₂, H₂S, CS₂, DMS) in the upper atmosphere by the 1995 Nobel Prize winner Paul Crutzen (Crutzen *et al* 2003, 2006). The impact of massive injection of Sulphur in the stratospheric chemistry

is, however, difficult to evaluate, and laser generation of local CCN appears significantly less invasive. The key question which obviously arises then is the feasibility of such large scale operation. Although highly speculative, this approach should, however, be brought in perspective to some parallel projects also aiming at bringing high intensity lasers on satellite platforms (Dicaire *et al* 2015, Mourou 2015, Quinn *et al* 2015, Dicaire *et al*, 2016). We will present some developments to this end in section 4.2 on the specific case of cirrus clouds.

4. Laser modulation of the optical transmission and albedo of fog and clouds

4.1. Intense lasers through clouds and fogs

In the previous section, we highlighted the possible use of laser induced condensation to increase the scattering of light (cloud albedo) in the atmosphere, in order to mitigate global warming. However, the opposite process, i.e. reducing scattering from clouds and fogs and enhance light transmission is also of considerable interest, in particular for optical data transmission applications. Significant efforts have been recently dedicated by space agencies (NASA, ESA) to improve laser communications between two satellites and between satellites and the Earth. For instance, the LCRD (Laser Communication Relay Demonstration; www.nasa.gov/mission_pages/tdm/lcrd/index.html) gram from NASA is designed to demonstrate high bandwidth telecommunication between geosynchronous orbits and the Earth by mid-2019. In addition to space programs, some internet wide coverage transmission programs, such as the Facebook Connectivity Lab program (https://info. internet.org/fr/ story/connectivity-lab/) and the Hyperion program from Airbus and Oxford (http://projecthyperion. co.uk/), which aim at establishing efficient laser datalinks between the ground and relay drones. An important limitation for all these programs is the availability of clear sky and the only present solution is to select some specific locations, reasonably unaffected by fog and clouds (like the JPL telescope at Table Mountain, California). However, the possibility of transmitting optical information through clouds and fogs remains a key issue for the widespread of laser telecommunications.

Clearing fog and clouds with lasers has been already investigated in the 70s and '80s with high power CO₂ lasers (figure 16) (see e.g. the remarkable book from V.E: Zuev (1985) However, the very large lasers needed to evaporate and shatter water drops (typically 10 kW cm⁻² continuous wave lasers (Zuev 1985) and 10–1000 MW cm⁻² pulsed lasers (Kwok *et al* 1988, Pustovalov *et al* 1992) respectively) appeared prohibitive for applications in the field with >100 m fogs. Notice that for focused Joule level nanosecond CO₂ lasers, plasma formation and shock wave induced explosion was already reported (Kafalas *et al* 1973, Kwok *et al* 1988, Singh *et al* 1988, Pinnick *et al* 1990, Zemlyanov *et al* 1996)

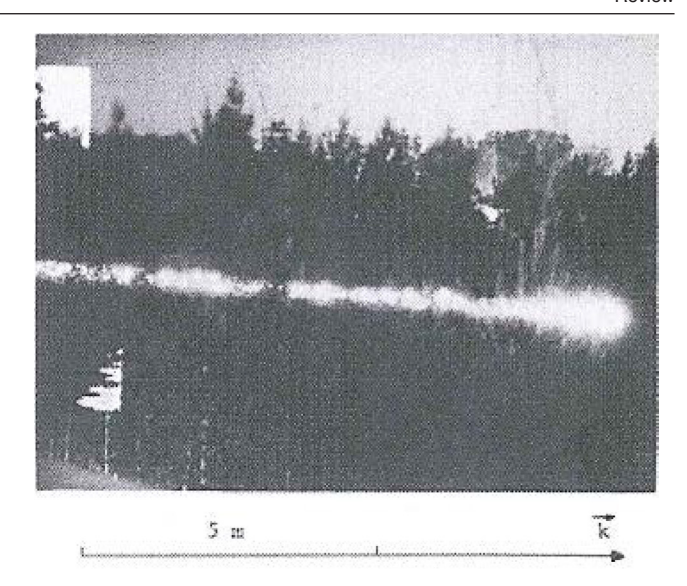


Figure 16. Fifteen meters spark induced in haze (15 m length) with a 200 J CO₂ laser, focused with a f/240 telescope (Zuev 1985).

in addition to evaporation, which occurred however for laser fluences beyond $200 \,\mathrm{J} \,\mathrm{cm}^{-2}$.

Ultrashort pulses and filamentation allowed to reconsider the possibility of transmitting information through fog with a fully different approach. In 2003, it was demonstrated for the first time that laser filaments could be transmitted through clouds (Courvoisier et al 2003a, Mejean et al 2005), because of a self-healing processes. More precisely when a 100–200 μ m diameter filament interacts with a 10–100 μ m water droplet, part of its energy is diffracted, and part of it is absorbed by the droplet mainly due to multi-photon ionization of water and plasma heating, leading to explosion. The Mie diffracted part, however, feeds the surrounding photon reservoir, so that Kerr effect refocuses the light after the interaction and reforms a filament (Courvoisier et al 2003a, Kolesik and Moloney 2004, Skupin et al 2004a). Since linear Mie scattering reduces the energy of the photon reservoir along propagation through the turbid medium it restricts its ability to reform a filament after interaction with the water drops. This limitation was clearly observed while transmitting multi-filamentary beams through extended clouds (Mejean et al 2005).

The mechanisms leading to droplet explosion in the case of ultrashort laser pulse illumination are also distinct from the case of nanosecond CO_2 lasers. In particular, femtosecond light pulses are focused by the spherical shape of the droplet and generate a localized nanoplasma at an internal focal spot, which emits blackbody radiation back to the illuminating source (Favre *et al* 2002, Courvoisier *et al* 2003b). The plasma then produces a shock wave that leads to the explosion of the drop (Lindinger *et al* 2004), as shown in figure 17. At intensities beyond 10^{13} – 10^{14} W cm⁻², plasma formation was also reported to occur already on the illuminated face of the droplet (Jeon *et al* 2015). The energy loss induced by a 50 μ m diameter droplet was estimated to be about 54 μ J, from which 41 μ J was directly absorbed by the plasma. Interestingly, the plasma distribution in the droplet and its deformation can be

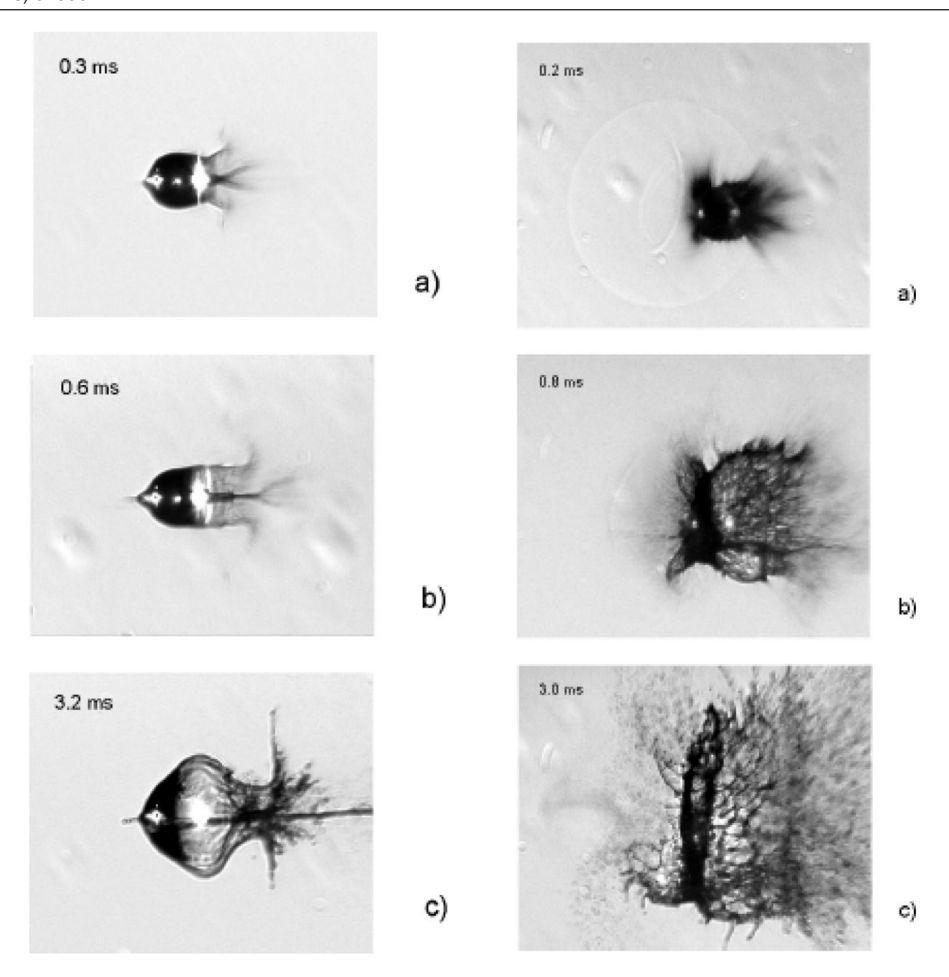


Figure 17. Explosion dynamics of individual water droplets by 60 fs laser pulses at 2 different intensities: $4 \cdot 10^{11} \,\mathrm{W \ cm^{-2}}$ (left) and $10^{14} \,\mathrm{W \ cm^{-2}}$ (right); (a)–(c) correspond to different times (in μ s and not ms as in the original caption) after the laser pulse. Laser propagates from left to right. Reproduced with permission from Lindinger *et al* (2004) © Copyright 2004 | The Optical Society. All Rights Reserved.

observed on the angular dependence of the white light emission. This was carried out as a function of incident intensity, showing a strong backward emission enhancement (factor 35 between the backward emission and the emission at 90° from the incoming laser) for the lower intensities (10¹² W cm⁻²) turning to much more isotropic emission for the highest intensities (Boutou et al 2002). From the higher intensity spots inside the droplets, not only multi-photon induced incoherent emission is generated (plasma, multi-photon induced fluorescence, Hill et al 2000) but also coherent harmonics (Leach et al 1993, Kasparian et al 1997). As will be shown below, exploding/evaporating ice crystals via plasma shockwave may have a further advantage: fast evaporation leading to supersaturation and generation of secondary particles of smaller size. This modification of the size distribution induces, in turn, a modification of the optical properties of the cloud, which could be useful in the context of climate warming mitigation.

4.2. Turning cirrus clouds radiative balance from heating to cooling?

Global warming relies on the spectral reflectivity (albedo)/transmission/absorption properties of the constituents of the

atmosphere. Cirrus clouds are formed over large areas of the upper troposphere at altitudes between 6 and 12 km at temperatures below -37 °C where only ice can exist as all water freezes by homogeneous nucleation (Stockel *et al* 2005). The cirrus ice crystals are large (50–100 μ m) as compared to both visible and IR wavelengths so that they reflect both the incoming solar radiation and the heat emitted by the Earth. On average, the warming effect seems to prevail; the magnitude and sign of the net climatic effect of cirrus clouds depend on the height and temperature of the cirrus cloud as well as on the size distribution and shape of the ice crystals (Liou 1986).

The interaction of laser filaments with cirrus ice crystals were investigated both at the large atmospheric cloud chamber AIDA (Karlsruhe institute of Technology) (Leisner *et al* 2013) and in a laboratory arrangement able to trap individual ice particles in an electrodynamic balance (Paul trap). The two experiments allowed to discover a new phenomenon called FISIM, for Filament Induced Secondary Ice Multiplication.

As mentioned in section 3.2, the AIDA facility allows studying the nucleation and condensation in a very wide range of conditions. In particular, cirrus-like clouds can be produced in conditions representative of the upper

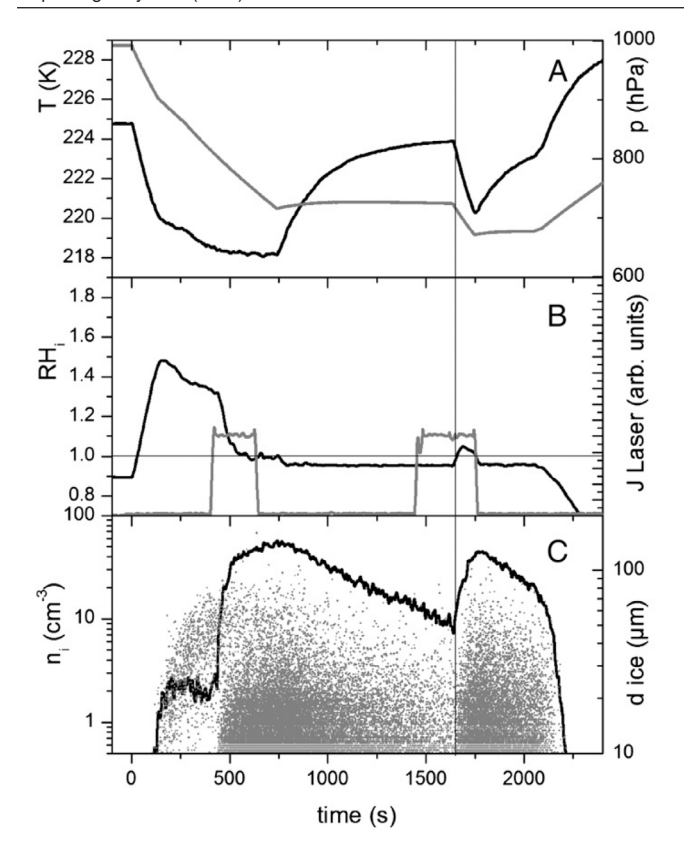


Figure 18. Typical expansion profile and ice cloud characteristics at low temperatures and two periods of laser action. The black and gray curves correspond to the left and right vertical axes, respectively. (A) Chamber gas phase temperature and pressure. (B) Relative humidity with respect to ice and duration of laser operation. (C) Forward and backward light-scattering intensity. (D) Ice particle number concentration and ice particle size. Reproduced with permission from Leisner *et al* (2013). Copyright © 2013 National Academy of Sciences.

troposphere and lower stratosphere. Laser filament–cloud interaction experiments have been performed over a range of tropospheric conditions with temperatures between $10\,^{\circ}\text{C}$ and $-60\,^{\circ}\text{C}$, and pressures from 0.6 to 1 bar. Clouds were created by adiabatic expansion in atmospheres consisting of synthetic air with or without additional cloud condensation nuclei introduced before the expansion (mineral dust or sulfuric acid particles).

Although laser filaments nucleated additional ice crystal at temperatures below the limit of homogeneous freezing and at supersaturation with respect to ice, we will concentrate here on conditions where cirrus clouds were formed in the chamber before the laser filaments were irradiating the chamber, using mineral dust as CCN (Leisner *et al* 2013). In this case (-50 °C), a thin ice cloud ($2 \, \text{cm}^{-3}$) was nucleated heterogeneously on the mineral dust particles around time $t = 100 \, \text{s}$ (figure 18). The laser was fired at $t = 400 \, \text{s}$ when the initially nucleated ice particles were already grown to about $50 \, \mu \text{m}$. Within less than $100 \, \text{s}$, the laser filaments led to the production of a large number ($50 \, \text{cm}^{-3}$ at $t = 700 \, \text{s}$) of much smaller ice particles. At that time, the laser action was stopped as the relative humidity respective to ice RHi had dropped to unity and no

further ice was produced. At $t = 750 \,\mathrm{s}$, pumping was stopped and the ice cloud started to evaporate at a relative humidity level just below unity. At $t = 1450 \,\mathrm{s}$, the laser was fired again into the evaporating ice cloud for a second period but with no detectable effect. Only after pumping was resumed at $t = 1630 \,\mathrm{s}$, a second mode of laser-generated ice particles could be observed as soon as RHi increased above unity again (figure 18(b)).

The need for preexisting ice particles to observe FISIM implies that the interaction of laser filaments with ice particles plays a central role in the ice multiplication process. For typical laser parameters used in these experiments and at typical initial ice number concentrations, only about 1 of 10-100 laser pulses interacts with an ice particle within the 80 mm³ of the filament volume. The fast growth of the ice particle number density implies that each laser-ice particle interaction produces an extremely large number of secondary ice particles with a size limited to the nanometer range by water mass conservation. Their subsequent optical detection indicates that they can grow into the μ m size range while being distributed through the ice-supersaturated AIDA atmosphere. Eventually, they are transported back into the filament region where they can contribute to a new to the ice multiplication process. The secondary ice particles could be created either by laser-induced mechanical shattering of the preexisting ice particles or by thermal evaporation of the ice particles and a subsequent condensation of the water vapor to form a large number of small droplets.

The FISIM phenomenon was analysed in detail by investigating the laser-ice crystal interaction at very high spatiotemporal resolution and at the single particle—single laser shot level (Matthews et al 2016). Each individual ice particle was injected into an electrodynamic Paul trap as a distilled water droplet, using a piezo-injector. It homogeneously freezed into a 90 μ m ice particle during its descent into the trap, which is kept at a temperature of -41 °C (that is, below homogeneous freezing) by a cold finger. The evolution of each ice particle after interaction with the laser filament was monitored at a rate of up to 140 000 fps by an ultrafast camera equipped with a microscope objective ($\times 5$) and an illuminating light-emitting diode. The interaction with the filament induced a plasma shock wave in the ice particle which partially shatters it in smaller fragments but also vaporizes a significant part of it (typically 15-20%) within a few microseconds. At later times, more than 10 freshly grown static particles of at least several micrometers appeared within the depth of field of the imaging system in the trap center. In contrast to the fragments resulting from particle shattering that are ejected with momentum from the explosion, these particles have no kinetic energy and stay in the trap over times of up to milliseconds. In figure 19, few tens of new ice particles are observed, with an average diameter of $\sim 5 \mu m$, periodically re-illuminated by scattered light from later laser shots. Throughout the water evaporated zone, water vapor condensed either on preexisting aerosol particles or on the ions remaining from the laser plasma at a relative humidity

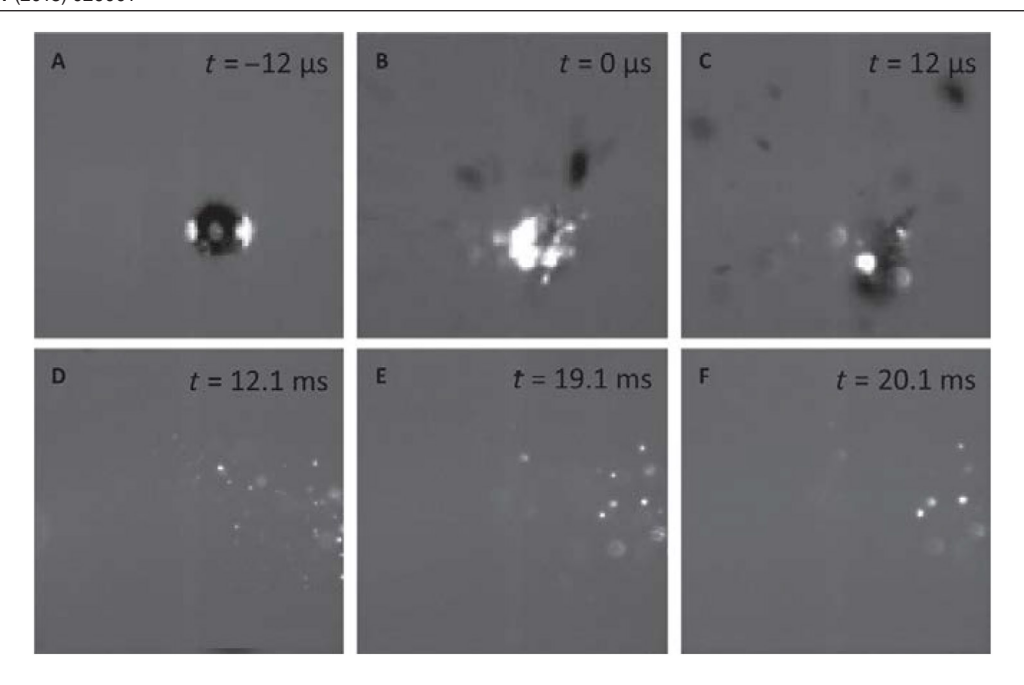


Figure 19. Formation of new, homogeneously frozen ice particles by the FISIM process (A) particle before the laser illumination. (B) Laser illumination. (C) Particle explosion. The main fragment is ejected backward and leaves the field of view, whereas many smaller particles are ejected from the shadow face. (D)–(F) Formation of smaller particles along the trajectory of the larger fragment after further illuminations by the laser filament. Reproduced from Matthews *et al* (2016) CC BY 3.0.

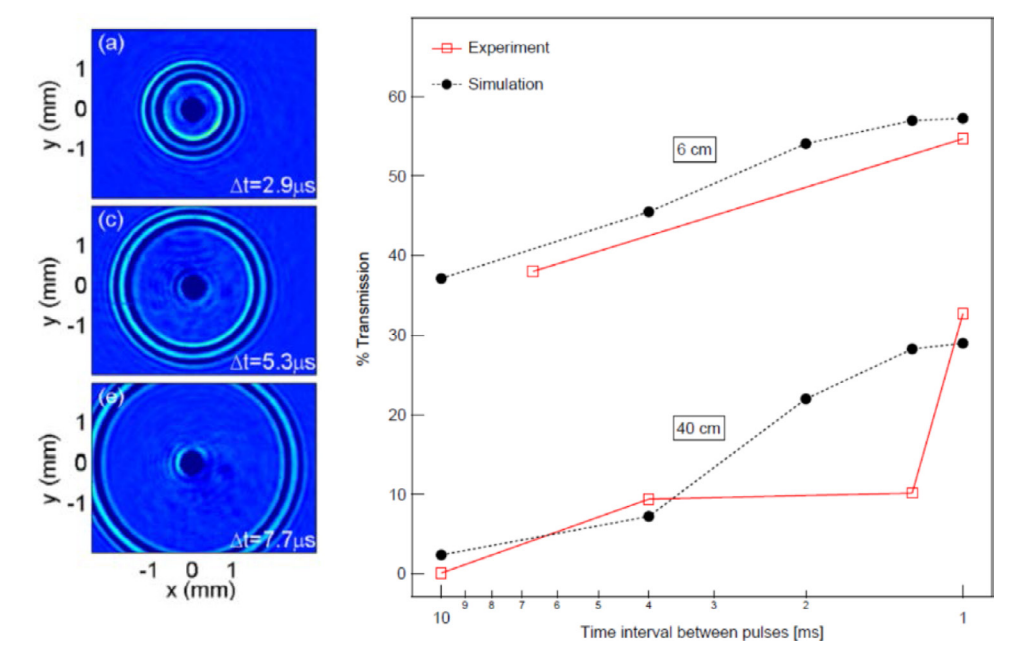


Figure 20. Left: observation of a filament shock wave propagating in clear dry air. Reprinted figure with permission from Lahav *et al* (2014), Copyright (2014) by the American Physical Society; right: first demonstration of laser transmission through fog using the opto-mechanical expulsion of droplets by the filament shock wave. Reprinted from De la Cruz *et al* (2016), with the permission of AIP Publishing.

above the threshold for ion induced nucleation of RH = 4 (Rabeony *et al* 1987), or homogeneously around RH = 15 (Wolk *et al* 2001).

In summary the interaction of filaments with the cirrus ice particles lead not only to the fragmentation of the crystals but a significant fraction of the crystal was evaporated by the induced shock wave. In turn the additionally released water vapor led to supersaturation, so that a multitude of small, micrometer sized secondary ice crystals were created, harnessing the available water around the mother particle. FISIM therefore leads to an increase of albedo for visible wavelengths (solar radiation) and a decrease of albedo for the infrared (heat from the Earth) because of the shift of the size distribution towards smaller sizes. Such a phenomenon would therefore lead to a net radiative balance towards cooling the atmosphere instead of heating.

4.3. Novel approaches for cutting a path through fog and transmit optical data

The two former sections rely on the vaporization/shattering of water droplets and ice crystals when irradiated by very intense lasers. Cutting a path through fog for transmitting optical data by evaporating or shattering all the droplets along the optical path requires, however, considerable amounts of laser energy. An alternative approach was recently proposed, based on displacing the fog droplets instead of evaporating them. When a NIR filament is created in air, it produces a shock wave that leads to a reduced density channel significantly larger than the size of the filament itself (~10 times larger) over a time window of 0.1–1 ms (Vidal *et al* 2000, Cheng *et al* 2013, Jhaji *et al* 2014, Lahav *et al* 2014). This shock wave, in turn, radially expels the surrounding droplets and if the repetition rate is faster than the time required for the particles to re-enter the cleared volume, this volume remains clear.

The first demonstration of clearing fog by opto-mechanical expulsion was recently performed using a 100 mJ, picosecond thin disk laser at 1 kHz repetition rate (De la Cruz et al 2016). More precisely, the Ytterbium laser generated a couple of filaments in an artificial fog containing ~10⁴ droplets cm⁻³ of sizes from 1 to 10 μ m, with varying time intervals between the pulses (i.e. repetition rates). Two fog thicknesses were tested: 6 cm and 40 cm. The experiment showed that the transmission spectacularly increased (from 0 to 30% for the thicker cloud) when the time interval between two pulses was reduced from 10 ms to 1 ms (figure 20). The red curves in figure 20 correspond to numerical simulations based on the shock wave dynamics observed by several authors for similar filaments (Vidal et al 2000, Cheng et al 2013, Jhaji et al 2014, Lahav et al 2014), atmospheric diffusion and turbulence, as well as droplet explosion and shattering. The increase of transmission is clearly identified as the mechanical radial expel of the fog drops (and eventually particles generated by the filament), allowing a larger section of the laser beam to be transmitted, and a replenishment of the cleared channel by the diffusion of new drops at longer times. This interpretation is also confirmed by the beam profile of the transmitted beam as a function of laser repetition rate (De la Cruz et al 2016).

More precisely, recording the image of the cross-section of the beam on a screen beyond the cloud allows to determine the diameter of the cleared channel, which increases (FWHM) from ~ 3 mm at 100 Hz to ~ 12 mm at 1000 Hz. This increase of the size of the cleared channel is in fair agreement with Monte Carlo based numerical simulations.

While the filament related shock wave was already successfully used both in the context of high voltage discharge guiding and triggering (see section 5.4) and in the context of laser guiding (Vidal et al 2000, Tzortzakis et al 2000, Cheng et al 2013, Jhajj et al 2014, Lahav et al 2014, Rosenthal et al 2014, Point et al 2015), the above described experiments extend their use to optical transmission through clouds. A major issue remaining for real scale applications is the ability of producing long range spanning filaments with sufficient energy to produce a strong shock wave even in turbulent air. In this respect, the present active development of terawatt mid-IR sources might bring significant progress.

5. Laser control of high voltage discharges in air: towards a laser lightning rod?

5.1. Physical mechanisms of natural lightning

Atmospheric electrification mechanisms and related discharging processes, including lightnings, are only partially understood (Gurevich et al 1992, Krider 2003, Lowke 2004, Gurevich et al 2005, Uman and Rakov 2005, Rakov and Uman 2003, Dwyer et al 2014). Cloud charging and charge separation are achieved by collisions between ice particles and/or water droplets as they experience strong vertical winds, with speeds up to 20 m s⁻¹. In most cases, convective updrafts transport positive charges to the cloud top and negative charges to its base (although some residual positive charging may remain at the very bottom of the cloud, below the negative layer). The charge separation induces local electric fields up to $\pm 150 \,\mathrm{kV}$ m⁻¹ (Marshall et al 1991) and a cloud-to-earth potential difference of 100 MV (Bazelyan et al 2000). Such high fields locally initiate corona Townsend type discharges (Townsend 1915), which develop into streamers by avalanche ionization. These low current streamers (typically 0.1 A, Bondiou et al 1994) eventually bundle up to create a much more conductive channel, in which Joule heating additionally decreases the resistivity: a leader. The current and temperature in a leader are respectively hundreds of amperes and 1500 K (at which an electron attachment process is prevented) (Bondiou et al 1994).

Due to the low resistivity of the leader channel, the voltage of the thundercloud is brought to the tip of the leader (figure 21), giving rise to corona and new streamers that allow the leader to propagate further towards the ground, by steps. These new streamers provide the current necessary to heat the leader. Each step of typically 50 m in length lasts some tens of microseconds, because of the time needed to heat the channel and lower the resistivity. While streamers can propagate at speeds close to the velocity of light (10^7-10^8 m) s⁻¹; Bazelyan et al 1998, Takahashi et al 2011), leaders are thus limited to average speeds of $10^5 - 10^6$ m s⁻¹. When the stepped leader approaches the earth, the potential of its tip at ~10 MV raises the surface electric field so much that corona discharges and upward propagating positive leaders are initiated at the top of elevated structures, especially if they are sharp, like lightning rods. The ascending positive leader eventually connects with the downward negative leader which gives rise to a highly conductive channel between the cloud base and the earth. A massive return stroke carrying more than 100 kA results from this short-cut, producing the characteristic flash of light and acoustic shock-wave of the lightning discharge. If the cloud available charge is not fully neutralized by the first discharge, subsequent strokes can follow until the process stops.

5.2. Laser induced high-voltage discharge triggering and guiding

The use of laser induced plasma formation in air for triggering high-voltage discharges started soon after the invention of

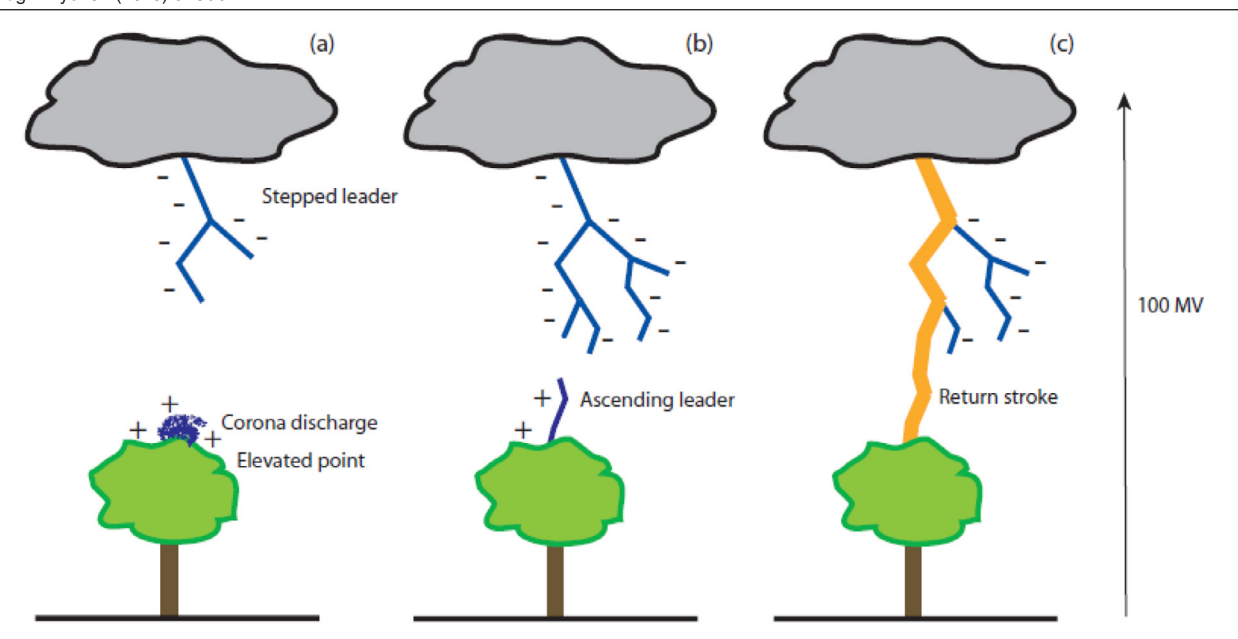


Figure 21. Simplified development of a lightning discharge: (a) stepped leader formation; (b) initiation of an upward leader; (c) return stroke. From Kasparian *et al* (2008). With permission of Springer.

the laser. For instance, Koopman et al demonstrated streamer guiding (over 28 cm) and 350 kV discharge triggering (Vaill et al 1970, Koopman et al 1971) using a Nd:Glass laser of 86 J and 2 GW peak power. He also showed that gas rarefication due to laser energy deposition was able to extend the length of the guiding channel (Saum et al 1972). These pioneering demonstrations initiated many investigations from scientists around the world as for example the remarkable work performed at the Electrical Power Research Center in Japan in the 1990s. Laboratory experiments with high energy nanosecond CO₂ lasers (Miki et al 1993, Shindo et al 1993a, Shindo et al 1993b) and KrF UV lasers (Miki et al 1996b) allowed to guide megavolt-class discharges up to 2 m-long gaps. However, the nanosecond laser pulses yielded a series of localized plasma balls, rather than an extended conductive channel: The high electron density plasma, produced by the leading edge of the mid-IR pulse and avalanche ionization, was opaque for its trailing part, which hindered adequate further propagation. The mechanism of triggering and guiding discharges on a meter scale with a series of plasma balls was demonstrated a few years later by using a series of conductive spheres along the path between the electrodes (Miki et al 1996a).

The first attempt to trigger and guide lightning in real scale was realized in 1999 by Uchida *et al* on the shore of the Sea of Japan in a period of intense winter low-cloud thunderstorms (Uchida *et al* 1999; preparatory work: Wang *et al* 1994, 1995). Three lasers were used: One 1 kJ CO₂ laser was focused on a dielectric target at the top of a 50 m high tower constructed on a 200 m high hill, while a second one was focused near to the generated ablation plume to form a 2 m long plasma spark. A third, ultraviolet laser produced a weakly ionized plasma channel slightly offset from the tower, intended to direct the leader to the cloud. The lasers were triggered when the initiation of cloud discharges, considered as the precursor of the descending lightning strikes, was detected. The authors

reported two successful attempts, but the poor statistics on the results could not lead to decisive conclusions.

As mentioned above, a major drawback of nanosecond lasers is their inability to produce long conductive channels. In 1995, the group of J C Diels demonstrated that extended channels are produced by femtosecond UV lasers (seeded KrF lasers) and that they efficiently trigger and guide 100 kV discharges on the 26 cm gap between the electrodes (Zhao *et al* 1995, Rambo *et al* 2001). He therefore demonstrated that ultrafast lasers are excellent candidates for HV discharge control, which were, since then, extensively used by different groups.

It is important to notice, however, that the distance on which the investigations are performed plays a crucial role. As described above, discharges over some centimeters are not fully representative of a lightning process, since the development of a leader and its associated corona front requires meters of propagation. We will therefore concentrate here on experiments and simulations related to this scale. In turn, electric breakdown over some meters in air requires dedicated high voltage facilities able to provide some MV. In this respect, pioneering experiments were carried out at the turn of the millennium by scientists in Canada (INRS and Hydro-Quebec) and by the Teramobile consortium in Europe. In 2000–2001, triggering and guiding leader discharges was demonstrated by the groups of J C Kieffer and H Mercure, by focusing 400 mJ picosecond laser pulses (at 800 nm) between two electrodes (Comtois et al 2000, Pepin et al 2001) separated by 3-7 m. They observed a decrease of the leader inception voltage of 50% and discharge guiding over distances up to 3 m, which constitutes the first large scale guiding and triggering of MV-class discharges. These remarkable results could also be interpreted by a physical model, based on the work of Bondiou and Gallimberti (Bondiou et al 1994). They extended their work by guiding discharges over 2 m with laser filaments and evidenced a ten fold acceleration of the leader velocity by the laser induced plasma (La Fontaine et al 2000). Triggering

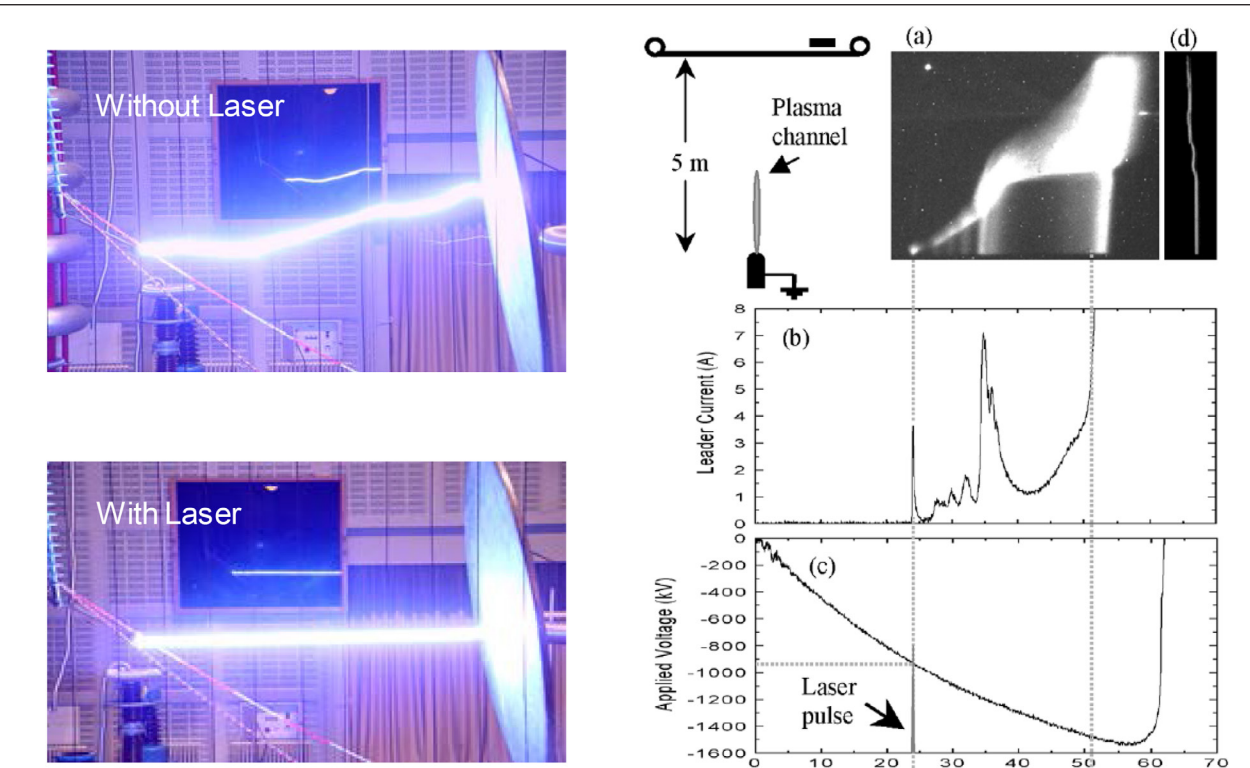


Figure 22. Triggering and guiding MV-class discharges by laser filaments over several metres. Left: bridging the entire gap with laser filaments leads to a weakly ionized channel that resistively connects both electrodes. From Kasparian et al (2003). Reprinted with permission from AAAS. Note the positive streamers arising from the plate ground electrode when the laser is absent; right: laboratory configuration designed as closest to a laser lightning rod. In contrast to the left panel, the rod is grounded and the plate electrode is negatively charged. (a) Streak picture of the development of the leader. (b) Current record. (c) Voltage impulse applied to the cathode. (d) Time-integrated picture of the resulting arc. Reproduced with permission from Comtois et al (2003a) © Copyright 2003 IEEE.

and guiding of MV discharges over 3.8 m with long laser filaments was demonstrated by the Teramobile group (Rodriguez et al 2002, Ackermann et al 2006a). A reduction of ~30% of the breakdown voltage was observed as compared to natural breakdown. In contrast to the Canadian experiments, the voltage pulse provided by the Marx generator and applied to the electrode was negative (down to—2.7 MV) as compared to the ground electrode. The mechanisms, revealed by current analysis and fast frame camera pictures rely on a laser guided path for the negative leader tip. Additionally it was also observed that the laser plasma channel can trigger space-leader discharges between the electrodes (Ackermann et al 2006a). These experiments were repeated under (artificial) rain conditions in order to approach realistic thunderstorm conditions. A heavy rain with a flow of 1.4 mm min⁻¹ reduces the discharge laser triggering probability by 30% but has almost no influence on the triggering thresholds, both in electric field and laser energy, which is encouraging for real scale applications (Ackermann et al 2004).

Further investigations were dedicated to get experimental laboratory conditions as close as possible to a laser lightning rod (Comtois et al 2003a, 2003b). More precisely, they used a 5 m diameter negative electrode, representing the descending negative leader, located at 5 m distance from a 2 m long lightning rod, installed at the center of a 15 m diameter circular ground plate. The rod was drilled in its center to let the laser through and the negative voltage was ramped on a time scale mimicking the actual approach of a leader to the ground during a thunderstorm, i.e. a rise of the electric field at the rod tip between 600 and and $3000\,kV\ m^{-1}\ m\ s^{-1}$ (Rizk 1994). The role of the laser in this configuration is to promote and guide the positive ascending leader from the lightning rod until it connects to the descending leader and produce the final stroke.

30

Time (us)

60

 t_2

More precisely, as depicted in figure 22 (right column), as soon as the laser is launched in the gap at t_1 (-930 kV), it instantaneously triggers a first corona, as well as the leader inception (see the associated current spike). The positive leader is then guided by the plasma channel over 2 m at a speed exceeding 10^5 m s⁻¹, as shown by the fast rise of the second current peak and the streak image. Notice that in this laboratory experiment, the natural leader velocity amounts $\sim 10^4$ m s⁻¹. At the end of the laser plasma channel, the leader propagates through the remaining 3 m gap to the negative plane electrode at its natural velocity, i.e. one order of magnitude slower. Finally, when the positive leader reaches the plane electrode, simulating the descending negative leader, connection is achieved and the final jump occurs, with a perfectly guided section of its path corresponding to the laser plasma channel.

More recently, the LOA group showed that femtosecond laser filaments are able not only to trigger and guide high voltage discharges, but also to divert an electric discharge from its natural path. For instance, arching towards a traditional lightning rod could be prevented at the benefice of a laser filament assisted one (Forestier et al 2012).

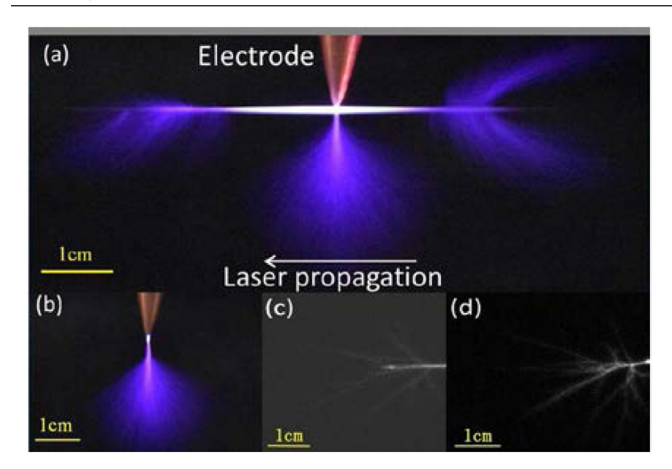


Figure 23. (a) Real-color images of typical filament guided corona discharge, the filament being the white elongated horizontal region, (b) corona discharge without laser filament, (c) and (d) for the fine structures for those streamers in the forward direction of laser propagation from (a) and (b), respectively. The corona discharging voltage and filamenting pulse energy were 50kV and 7.5 mJ, respectively. Reproduced from Wang *et al* (2015) CC BY 3.0.

As described at the beginning of the section, the path length between HV electrodes plays a crucial role, as leaders can only develop at or beyond the meter scale. But the temporal variation of the electric field dE/dt applied to the electrodes plays a similar role as well. For instance, applying a DC voltage instead of microsecond pulses showed that two breakdown modes may co-exist, the fast mode, already identified with pulsed sources and a slow mode spanning over millisecond time scales (Fujii et al 2008). This slow process, linked to the ions mobility appeared, however, only for DC voltages close to the natural breakdown.

In contrast to the DC and the ramped fields, investigations were also carried out using AC generators such as Tesla coils (Brelet *et al* 2012, Henriksson *et al* 2012, Daigle *et al* 2013, Arantchouk *et al* 2014). Although less representative of actual lightning conditions, these coils could be deployed in addition to the laser to extend the plasma channel. For instance, triggering and guiding was demonstrated over 1.8 m at fields of only 2kV cm⁻¹, and could even be consecutively repeated at a 10 Hz repetition rate (Arantchouk *et al* 2014). The discharge control mechanisms are, however, different from the slow or DC fields, since the discharge evolves in a pure leader regime (no leader streamers) (Daigle *et al* 2013). A recent interesting study also nicely addressed the development of discharges between HV electrodes as a function of pulse duration and chirp sign, by using fast imaging (Schmitt Sody *et al* 2015).

Finally, the role of laser filaments on corona discharges and associated streamers was studied in depth by the group of T Fujii at CRIEPI in Japan. In particular, the authors focused on the appearance of runaway electrons, which are suspected to play a crucial role in the lightning development (Gurevich et al 1992, Dwyer 2005, Gurevich et al 2005). Runaway electrons (originating, e.g. from cosmic rays) are electrons travelling close to the light velocity, which allows them to travel much longer paths in the atmosphere than their more traditional counterparts. They produce secondary fast electrons via avalanche ionization and radiations like x-rays or gamma rays

(Fishman *et al* 1994, Dwyer *et al* 2003, Tsuchiya *et al* 2007), which further promote ionization and cloud droplet nucleation. The CRIEPI group reported the possible observation of runaway electrons around the laser filament and the electrodes by imaging UV burst emissions (Sasaki *et al* 2010, Sugiyama 2010). They also recently reported the filament capability of quenching runaway electrons (up to 1 MeV), when the laser is perpendicular to the discharge axis (Eto *et al* 2012).

Laser guiding and diverting corona discharges were also investigated in the context of glow discharging (Wang et al 2015) and spark-less unloading of HV capacitors (Schubert et al 2015). For instance corona discharges have been clearly guided from the tip of a HV electrode to the tips of a filament (figure 23). Additionally the glowing time of the corona was extended up to several microseconds, i.e. 1000 times longer than a filament without HV. Similar observations were reported by Schubert et al, in the context of suppressing natural breakdown between 100 kV electrodes by neutralizing them with a filament induced super-corona discharge (Schubert et al 2015). These unexpected results are interpreted as a quasi-continuous flow (repetition rate of the laser was 1 kHz) of charges through the glowing filament channel, the resistance of which is strongly decreases by heating, and a strong modification of the field lines because of the presence of this highly conductive channel. The breakdown suppression effect is nicely demonstrated in the supplementary videos linked to Schubert et al (2015).

5.3. Electric activity modulation of thunderclouds with laser filaments

Very few field measurements have been carried out to trigger, guide, or divert lightnings with lasers in actual conditions, since the tentative of Uchida et al (1999). To our knowledge, the only attempt reported in the literature was achieved by the Teramobile group in 2004 (Kasparian et al 2008c). Unlike the experiment from Uchida et al, the aim of the experiment was to trigger lightning from the thundercloud, and not to extend the active length of an existing lightning rod. To this end the Teramobile system was moved for a 3 months campaign to the Langmuir Laboratory, on the top of the South Baldy Peak (New Mexico, USA), located 3200 m above sea level. The 3 TW laser was triggered at a repetition rate f = 10 Hz (i.e. every $T = 100 \,\mathrm{ms}$) by an internal clock, independently from the thunderstorm activity. It produced multiple filaments with significant ionization over a typical length of 100 m, a few hundreds of meters above ground.

The beam was launched southwards at an angle of 70° above horizontal. They focused the analysis on times when the electric field on the ground would have been sufficient to trigger lightning using rockets, i.e. exceeded 10 kV m⁻¹ (measured by a field mill). The Langmuir Laboratory was equipped by a Lightning Mapping Array (LMA; Rison *et al* 1999), which detects radio-frequency (RF) pulses at 63 MHz, monitoring the electric activity of the atmosphere. The multiple antennas (in this particular study: 5) allow for reconstructing the paths of atmospheric discharges in 3D with 100 m resolution. Since the laser was fired at 10 Hz on its own master clock, fully

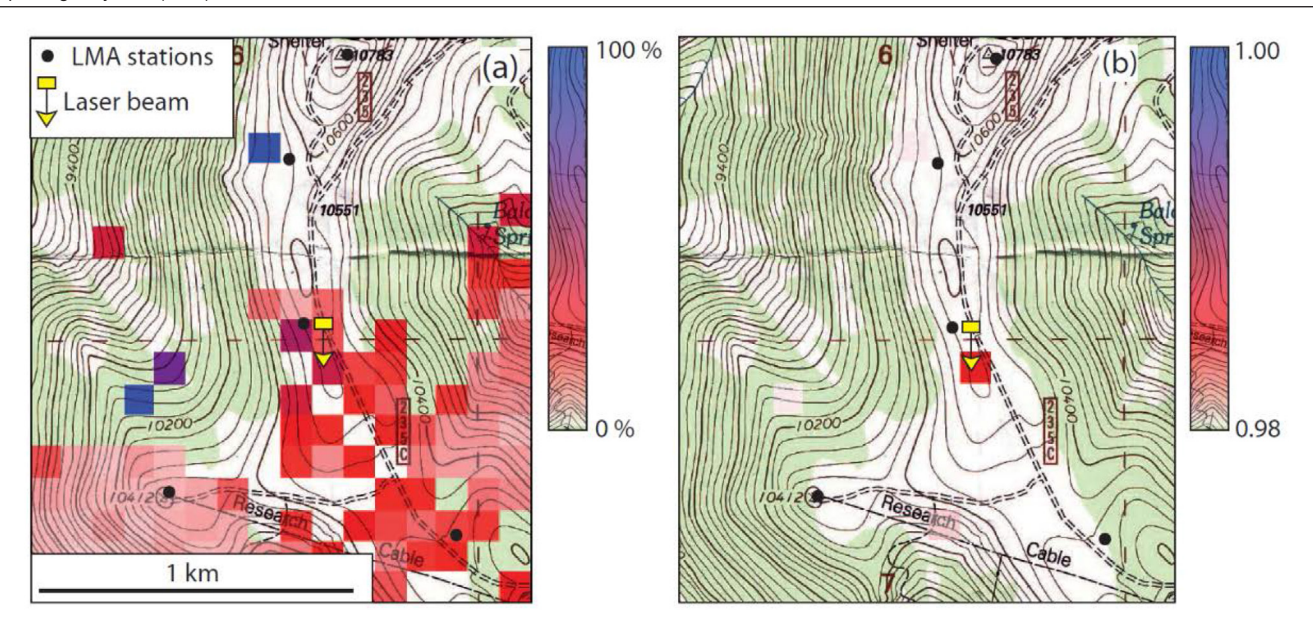


Figure 24. Laser induced generated discharges in an actual thundercloud by the Teramobile (location labelled by a yellow rectangle). (a) Pulses synchronized with the laser repetition rate; (b) corresponding statistical confidence level. The color scale is transparent below 98% (i.e. for error risks above 2%). Topographic background courtesy of US Geological Survey. Reproduced with permission from Kasparian and Wolf (2008a) © Copyright 2008 The Optical Society. All Rights Reserved.

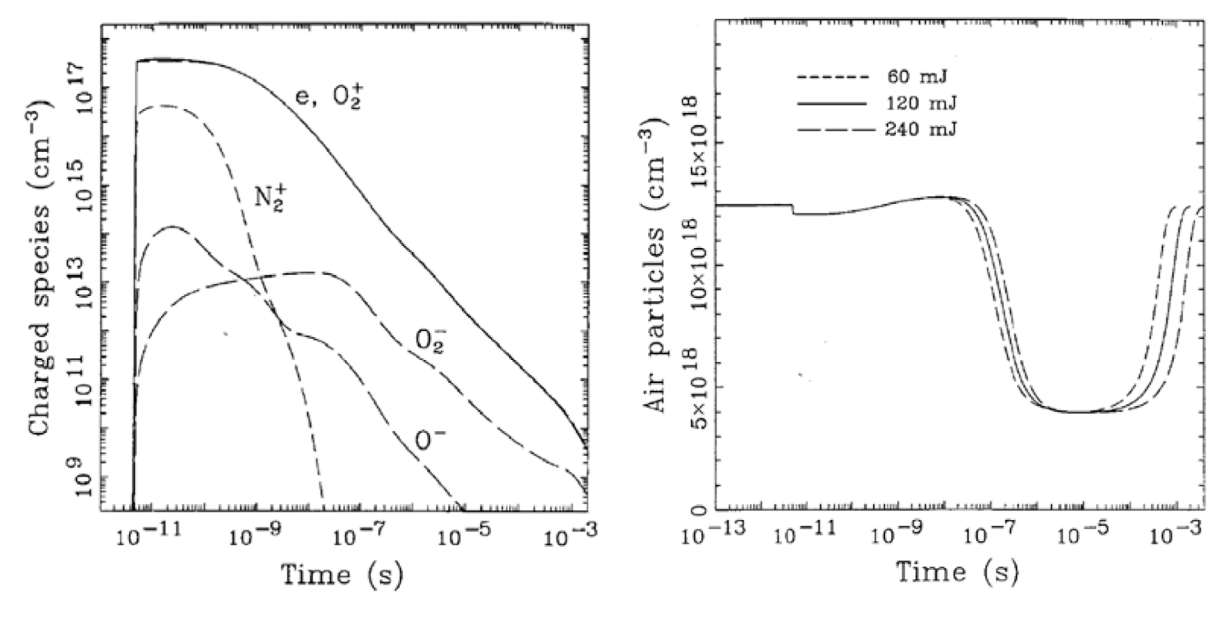


Figure 25. Dynamics of carrier densities (laser pulse energy: 120 mJ) and air rarefaction in the wake of a laser induced plasma channel and in an external electric field of ~5 kV cm⁻¹. Reproduced with permission from Vidal *et al* (2000) © Copyright 2000 IEEE.

independent from the random atmospheric breakdown events, a statistical analysis could be performed to assess causality between laser firing and atmospheric activity.

More precisely, figure 24 shows an example of data, over a 5 min window. On the left, all electric events synchronous with the laser and detected by the LMA are displayed. Clearly, the frequency and randomness of the discharges allow discharges to occur at time intervals corresponding, by chance, to the time interval between laser pulses. However, if we consider only the events where the statistical confidence is above 98%, the only statistically representative events are precisely located at the filaments position (note the slight shift as compared to

the laser system, due to the 70° elevation angle of beaming towards the southern direction). Notice that, additionally, no event associated to the laser firing was observed if the electric field at ground level was less than $10\,\mathrm{kV}$ m⁻¹.

The meteorological conditions over the 3 months campaign only provided two thunderstorms. Similar results as the ones displayed in figure 24 were obtained during both events. However, no lightning guiding or triggering down to the earth was achieved, while wire pulling rockets would probably have. A probable reason invoked by the authors is the short laser plasma lifetime, as compared to the leader propagation speed of $10^6 \ \mathrm{m \ s^{-1}}$.

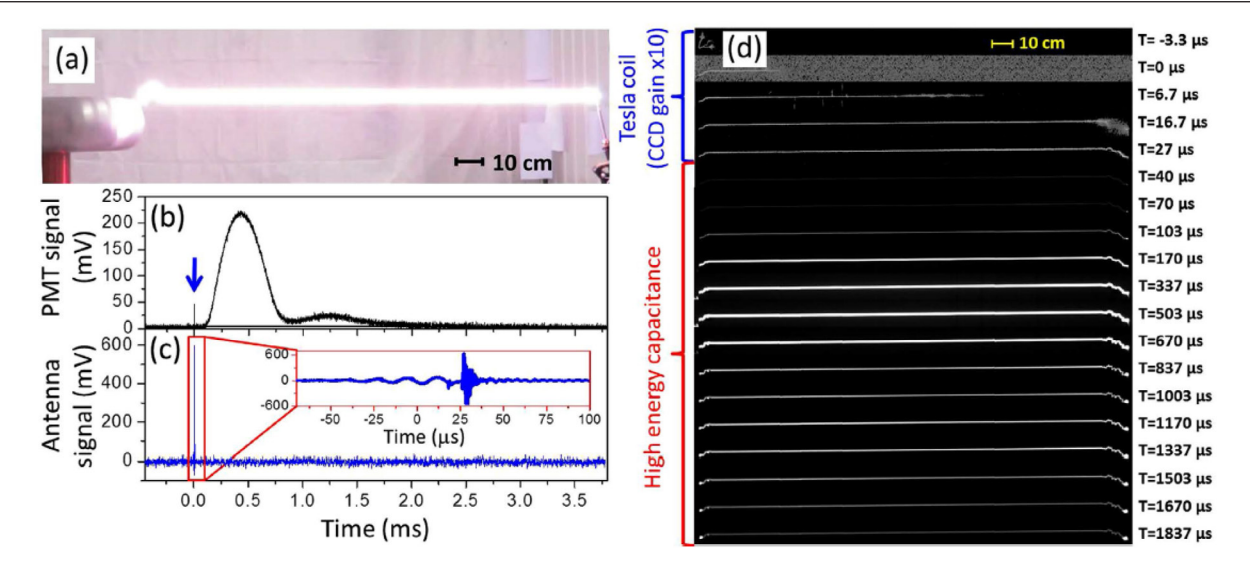


Figure 26. (a) Time-integrated colour image taken by a digital camera of the laser-guided AC–DC discharge over a 200 cm air gap. The DC voltage amounts only 30 kV. (b) Plasma fluorescence (c) temporal waveform of the electric field during the laser-guided AC–DC discharge. (d) Successive video frames of laser-guided AC–DC discharge taken by a monochrome high-speed camera. Reproduced from Theberge *et al* (2017) CC BY 3.0.

5.4. Extension of the laser conductive channel lifetime

A major limitation to real scale lightning guiding or triggering is the short lifetime of the plasma channel left in the wake of the filament. Recombination of the free electrons to the parent ions occurs within nanoseconds, while attachment to neutral oxygen molecules follows afterwards an exponential decay over some hundreds of nanoseconds (Tzortzakis et al 2000, Bodrov et al 2011). More precisely, the electron ionization rate and electron-ion recombination are essentially described by equation (2.11) from section 2. On longer timescales, two- and three-body attachment to neutral molecules leads to a first order decay, which efficiency strongly depends on the electronic and molecular temperatures (Zhao et al 1995). Vidal et al (2000) simulated the decay of carriers for a situation including a laser and external high voltage field, i.e. close to thunderstorm conditions or experiments on meter long discharges. An updated model of the laser induced HV-discharge triggering mechanisms, which relies on a compilation of the most recent values of the parameters needed for the simulation, was for instance recently presented in Schubert et al (2016a).

As shown in figure 25, the carrier density decreases by about 4 orders of magnitude over the first microseconds, which would correspond to the propagation of a leader over only 1 m.

However, these free electrons are accelerated by the external electric field and significantly heat the plasma, leading to a rarefication of the gas column by more than 50% (figure 25 right) after 1 μ s. If the Joule heating leads to a temperature exceeding the critical temperature (1500 °C), attachment to molecular oxygen is prevented and electrons may be released from the existing anions. Additionally, a lower air density opens a preferable path for the electric discharges by reducing the breakdown voltage following the well-known Paschen law (Paschen 1889). When the gas density is reduced, the mean free path of the free electrons increases, so that they

can gain more easily the kinetic energy required to ionize neighboring molecules and initiate a Townsend avalanche. Notice that the hot, lower density channel remains active for several ms, which would theoretically allow the propagation of a leader over kilometers. However, a major outcome of F Vidal's simulations is that a minimum electric field strength of 4kV cm⁻¹ and a minimum electronic lineic density of 10^{11} /cm are required for the development of a laser guided leader (Vidal *et al* 2000).

The main tracks for extending the length of guided lightning strikes thus rely mainly on two possible actions: (1) photo-detaching the electrons trapped on O_2^- and (2) heating the plasma channel.

5.4.1. Trains of ultrashort pulses. The most natural idea for extending the lifetime of a plasma channel is to partition the energy in several pulses, separated by adequate time delays. Recent results obtained for NIR pulses show that partitioning the total energy of a pulse in a train of sub-pulses (separated by ~3 ns) is more efficient to extend the plasma lifetime than using the full energy in a single pulse (at the cost of the peak electron density), mainly because of the spatial break-up of the beam in a bundle of multiple filaments (Guo et al 2012, Schubert et al 2016a). Notice, however, that the situation will certainly be different at other wavelengths, like in the mid-IR (Panagiotopoulos et al 2015), or at high laser repetition rate, where cumulative thermal channeling appears.

Some groups investigated the effect of adding successive ultrashort pulses in a train as compared to a single one. For instance a pair of femtosecond pulses (15 mJ + 15 mJ), with a time separation of 7 ns, doubles the time on which carriers are available, but does not provide significant improvement on triggering or guiding high voltage discharges (Zhang *et al* 2009). On the other hand, the group of Ruxin Li (Ji *et al* 2010) demonstrated that producing a train of \sim 10 low energy femtosecond pulses allows to sustain a plasma over 60 ns. More recently, the group

of J Zhang developed a dedicated laser that provided a train of 17 femtosecond pulses over ~200 ns (with total energy: 60 mJ) and could extend the plasma lifetime up to a microsecond (Liu *et al* 2012). They also increased the length of this steady-state plasma channel from the centimeter to the meter scale (Lu *et al* 2015) but showed that even with a time separation between pulses as short as 2.9 ns, no significant cumulative effect (e.g. heating by inverse bremsstrahlung) occurred in their conditions. The plasma lifetime extension was therefore attributed to the periodic creation of free electrons via consecutive photo-ionization.

5.4.2. Photo-detachment and re-heating with a concerted long pulse laser. In order to produce significant heating of the femtosecond filament by subsequent laser pulses, high energy nanosecond lasers have often been proposed. J C Diels originally suggested the concept in 1992 (Diels et al 1992) and realized it in 1999 using a 10 ps UV pulse at 248 nm followed by a 2 microsecond, 210 mJ pulse at 750 nm from an Alexandrite laser (Rambo et al 1999, Rambo et al 2001). Laser triggered discharges with these concerted laser pulses were demonstrated over 1 m with 400kV across the electrodes. Based on the experimental results, it was estimated that at least 5 J at 750 nm over 10 μ s would be required to maintain the necessary plasma density over 10 m. The advantage of using an Alexandrite, as compared to a 1064 nm YAG laser, is that it provides microsecond long pulses (sustaining the electron density on the adequate timescale) and a wavelength that can both heat the free electrons by inverse bremsstrahlung and directly photo-detach electrons from $O_2^$ and O⁻. The electron binding energies of the two anions lie indeed at 0.54 eV and 1.45 eV, respectively (Burch et al 1958, Rambo et al 2001).

Several studies on the laboratory scale were performed on the extension of the plasma lifetime using a re-heating strategy with Joule-class Nd: Yag lasers (Hao et al 2005, Zhou et al 2009, Polynkin et al 2011, Scheller et al 2014, Papeer et al 2014, 2015, Clerici et al 2015). In most of the cases, the plasma lifetime was extended to 50-60 ns and the maximum carrier density enhanced, up to a factor 200 (Polynkin et al 2011). Breakdown voltages over a cm sized gap could also be reduced by a factor 4 when using heater fluences larger than 1 kJ cm⁻² (Scheller et al 2014). A further interesting discovery is that the plasma could be revived after delays as much as one millisecond by launching two nanosecond pulses, at 532 nm and 1064 nm after the femtosecond igniter (Zhou et al 2009). As mentioned above, 532 nm is more efficient to photo-detach electrons, while longer wavelengths are more efficient for heating via inverse bremsstrahlung (scales with $\sim \lambda^2$; Yablonovitch *et al* 1972).

In almost all the above mentioned reported studies, simulations of the effect of the additional heating pulse are reported as well, with good agreement. A comprehensive parametric simulation study was also presented by Shneider *et al* (Shneider *et al* 2011). Interestingly, the effect on the plasma dynamics of a Nd:Yag laser at 1.06 μ m and of a CO₂ laser at 10.6 μ m are similar, if the Nd:Yag laser intensity is 100 times higher than its mid-IR competitor. However, beam propagation is not included in the simulation, so that the observed local plasma

bubbles that hinder further propagation (e.g. Miki *et al* 1996, Polynkin *et al* 2011) are not taken into account.

A critical issue in using two different lasers is the spatial overlap of the filament with the non-filamenting nanosecond laser. Best results have been obtained in this respect by the use of an axicon for focusing the nanosecond laser (Zhou *et al* 2009, Polynkin *et al* 2011, Scheller *et al* 2014, Clerici *et al* 2015). In this configuration, the associated Bessel beam could overlap efficiently the filament on a range from 30 to 50 cm. Unfortunately, scaling this approach to atmospheric distances appears very challenging.

The enhancement brought by an additional heating laser in conditions closer to real lightning, i.e. on distances over which leaders can develop, has also been demonstrated. In particular, the use of a modest energy 532 nm (0.4 J) nanosecond laser allowed to significantly increase the breakdown probability (by a factor 5) as compared to the femtosecond laser only, for a megavolt discharge over 1.2 m (Mejean *et al* 2006). The interpretation proposed by the authors is an efficient photodetachment provided by the visible light, and the acceleration of the freed electrons by the MV m⁻¹ external field, leading to avalanche ionization and channel heating. Conversely, a 1 J 1064 nm laser did not provide significant improvement.

Following the pioneering work of J C Diels using ultrashort UV lasers, recent developments were reported on the combination of a train of picosecond UV pulses with a long UV nanosecond pulse, originating from the same multi-Joules laser system (Ti:Sapphire seeded KrF laser; Zvorykin *et al* 2015). This hybrid pulse sequence was shown to trigger discharges over distances doubled as compared to the long UV pulse only (Ionin *et al* 2012), and successfully guided sub-MV discharges over 0.7 m (Zvorykin *et al* 2015).

5.4.3. Laser energy deposition and long-lived low density channels. Heating the plasma channel can also be achieved by the ultrashort laser filaments themselves, provided their energy deposition is sufficient. Interestingly, already in 1972, Saum *et al* investigated the effect of adding 15% ammonia in air, in order to increase the absorption of their CO₂ laser. The distance on which a HV discharge could be guided was extended from 14 to 20 cm thank to the higher deposited energy.

In the case of NIR laser filaments, heating arises via inverse bremsstrahlung absorption from free electrons, associated cascading ionization and thermalization from the hot electrons to the heavy species (recombination and collisions). Depending on the energy, peak power, and focusing geometry of the laser, the measured lineic deposited energy in the gas ranged from few μJ cm⁻¹ (Rosenthal *et al* 2016) to 13 mJ cm⁻¹ (Point *et al* 2016) in the case of focused TW-class lasers. Temperatures up to 1000 K were associated to this efficient laser energy deposition (Point *et al* 2015), which becomes then similar to the discharge heating of a leader by an external HV field.

Additionally, cumulative heating and gas rarefication can be achieved if the repetition rate of the laser is equal or larger than 1kHz, since the low density channel lifetime amounts ~1 ms (Cheng et al 2013, Jhajj et al 2014, Rosenthal et al 2014, Lahav et al 2014, Point et al 2015, De la Cruz et al

2016). With high repetition rate, high average power lasers, long lived underdense channels could be generated over 60–70 cm (Jhajj *et al* 2014, Houard *et al* 2016).

As already described in section 5.4, these columns of low density, hot air reduce both electron attachment to oxygen and breakdown voltage via Paschen's law, so that they represent attractive conditions for discharge guiding, even with moderate free carriers densities. They might then constitute a useful measure to counteract the limited plasma lifetime. A first demonstration of such a high average power (100 W) laser induced triggering of HV discharges by the hydrodynamic effect was recently reported by Houard *et al* (2016). The breakdown voltage could be reduced by as much as a factor of 3 (10 kV instead of 30 kV) over a 1 cm gap when the laser repetition rate was increased from 10 Hz to 1 kHz.

5.4.4. Channel heating by seeding filaments with high voltage boosters. An interesting approach to sustain long guiding channels over timescales beyond $100~\mu s$ (i.e. 100~m propagation of a leader) is to connect the filament to an additional high voltage potential. For instance, injecting additional current from a 20~kV source allowed to extend the discharge between two electrodes connected to a 100~kV Marx generator up to $130~\mu s$ (Arantchouk *et al* 2016). During this long time frame, the discharge remained fully guided over the 8.5~cm gap.

Seeding filaments with an AC Tesla Coil provided even more impressive results. The AC booster, able to deliver 1 J/ pulse, allowed to trigger and sustain a 2 m long conductive channel over milliseconds, when a modest 30kV DC voltage was applied between the electrodes. This 30kV DC would have been able to produce a breakdown over only a few cm without the AC seeding of the filaments. Accordingly, the air breakdown voltage for obtaining a DC glow discharge between the electrodes was as low as 12 kV for 1 m gap and 23 kV for a 1.75 m gap, i.e. a field as low as $0.13 \,\mathrm{kV} \,\mathrm{cm}^{-1}$ (230 times lower than the natural breakdown electric field). The heating of the column and associated gas expansion was therefore extremely efficient in this laser-AC pulse configuration, confirmed by the spectroscopic measurements of the emitted light. Analyzing the plasma lines revealed a plasma temperature of about 30000 K and of the gas blackbody radiation of 4800 K.

The experiments required a precise synchronization between the femtosecond Ti:Sapphire laser firing (150 mJ) and the AC voltage ($500\,\mathrm{kV}$) from the Tesla coil, in order to get full guiding of the discharge along the 2 m gap. It then successfully guided the 500 times more energetic discharge from the $30\,\mathrm{kV}$ DC source.

A combination of high average power ultrashort lasers, providing long filaments, connected to powerful pulsed high voltage sources appears therefore as a particularly attractive configuration for the set-up of laser lightning rods.

6. Conclusion

The development of ultrashort lasers with increasing peak (>TW class) and average powers allows considering possible modulation of key atmospheric processes, like cloud

nucleation, fog dispersion, or lightning activity. On the other hand the modest energy at play in the control handle requires situations where the laser plays the role of a photonic catalyst. For instance, very little energy is required to initiate a powerful lightning strikes, as the thundercloud-ground electrostatic system stores the whole energy before triggering. A similar situation occurs for water condensation, where a nanometric hydrophilic nucleus starts a long water vapor harvesting process until eventually a falling water drop is produced. Again the success of the process requires specific atmospheric conditions with suitable RH, temperature, temperature gradients, cooling rates, etc. The advantage of cloud seeding with laser filaments is therefore to provide the triggering nuclei exactly where they will be most effective to accommodate water. Combining laser seeding with Lidar diagnostics based on the same laser (Kasparian et al 2003, Bourayou et al 2005) is certainly the way to go in this context.

Some of the presented applications, like laser based lightning control or optical communications through fog, are certainly closer to a real world realization than others. In both of the former examples, the further rise in pulse energy (related, e.g. to large frame programs like ELI or XCELS; (ELI 2011, Bashinov et al 2014)), average power (linked with the development of industrial systems) and electrical-power conversion efficiency, will be decisive for a widespread use in the field. So will be the costs, ease of operation, and safety of such future devices. For instance, the 'price per photon' for a TW laser system has dropped by a factor 100–1000 in the last 15 years, thanks to thin-disk Yb laser technology (Metzger 2016). Also, the protection of sensitive sites like airports and the high costs related to lightning damages (~2 Billions USD/ yr) bring this application closest to a real world implementation. Some research projects (e.g. LLR 2017) including industrial consortia were recently launched to this end.

On the water condensation side, real world applications may (or may not) appear on a longer run. The rapidly growing water crisis calls for innovative and efficient technologies, since nowadays, the worldwide offer is limited to see water desalination with reverse osmosis. To become competitive, any new technology should thus ultimately lead to a reduction of both price and power consumption as compared to this technology, i.e. 1 USD m⁻³ and 10 kWh m⁻³ (without transport to the required location, which might be prohibitive). The niche of cloud seeding (chemical or photonic) therefore relates on more local and/or transient actions. A typical example would be coastal regions with rain shadowing, i.e. large mountains nearby an ocean. In this ubiquitous situation, the prevailing wet wind from the sea loses its moisture on the sea-side of the mountain, causing drought on the other side. Seeding could thus efficiently spread the available water on many small nuclei (instead of fewer larger droplets), preventing recurrent raining on the one side of the mountain and transporting moisture to the other side. In a similar way, one could consider seeding actions in order to decrease the activity of heavy rainstorms leading to massive flooding (e.g. flash flooding).

Concerning eye-safety, although vertical pointing a high power laser is not a major issue, if the use is concerted with the air traffic management, it might be relevant to consider transmitters in an eye-safe region, like the mid-IR. The hazardous path could be, in this case, restricted to the filamenting region, and not beyond it. Moreover, recent investigations on mid-IR filamentation show that in the 4–10 μ m region, longer range, higher energy channels are produced than in the NIR (Mitrofanov et al 2015a, 2015b, Panagiotopoulos et al 2015, 2016). Exploiting molecular resonances in the fingerprint region is also attractive for enhancing photo-chemical processes via selective bond-breaking. In this respect, it is interesting to notice that the only feature of ultrashort pulses used to date for the control of atmospheric processes is the resulting high peak intensity. On the other hand, controlling molecular processes with ultrashort laser pulses has been performed for decades in the laboratory, using coherent control methods and optimal pulse shaping (Chelkowski et al 1990, Judson et al 1992, Warren et al 1993, Levis et al 2001). In the atmospheric context, very few coherent control based investigations have been carried out so far. For example, pumpprobe and quantum control schemes were applied in order to quantify and discriminate among biological species, including bacteria and other bio-agents (Scully et al 2002, Courvoisier et al 2005, Kasparian et al 2008a, Li et al 2008, Roth et al 2009, Berti et al 2015). More recently, coherent controlling of the rotational wavepackets dynamics of air molecules showed that gas heating could be produced at a level significantly exceeding that of plasma absorption (in the same conditions) (Zahedpour et al 2014). In turn, as described in sections 4.3 and 5.4, efficient heating leads to favorable conditions for HV discharge guiding and fog clearing. Quantum controlling molecular dynamics for improving the efficiency of atmospheric control might therefore be an attractive option to investigate in the future.

Acknowledgments

The author acknowledges support from the European Research Council Advanced Grant 'Filatmo' and the NCCR 'MUST', from the Swiss National Science Foundation. He also greatly thanks Jerome Kasparian, See-Leang Chin, Ruxin Li, Jean-Claude Kieffer, Jean-Claude Diels and Aurelien Houard for their reading and their valuable comments and suggestions on this review.

References

Ackermann R *et al* 2004 *Appl. Phys. Lett.* **85** 5781–3 Ackermann R *et al* 2006 *Appl. Phys.* B **82** 561–6

Ackermann R, Mejean G, Kasparian J, Yu J, Salmon E and Wolf J P 2006 Opt. Lett. 31 86–8

Agrawal G P 2001 *Non-Linear Fiber Optics* 3rd edn (San Diego, CA: Academic)

Alfano R R and Shapiro S L 1970a Phys. Rev. Lett. 24 592-4

Alfano R R and Shapiro S L 1970b *Phys. Rev. Lett.* **24** 1217–20 Allan J D *et al* 2004 *J. Aerosol. Sci.* **35** 909–22

Andriukaitis G, Balciunas T, Alisauskas S, Pugzlys A, Baltuska A, Popmintchev T, Chen M C, Murnane M M and Kapteyn H C 2011 Opt. Lett. 36 2755

Arantchouk L, Honnorat B, Thouin E, Point G, Mysyrowicz A and Houard A 2016 Appl. Phys. Lett. 108 173501 Arantchouk L, Point G, Brelet Y, Prade B, Carbonnel J, Andre Y B, Mysyrowicz A and Houard A 2014 *J. Appl. Phys.* **116** 013303 Askaryan G A 1962 *Sov. Phys.—JETP* **15** 1088–90

Bandrauk A, Lorin E and Moloney J V 2016 *Laser Filamentation*, *Mathematical Methods and Models* (Switzerland: Springer International Publishing)

Bashinov A V, Gonoskov A A, Kim A V, Mourou G and Sergeev A M 2014 Eur. Phys. J. 223 1105–12

Baum D 2014 Sci. Am. 310 56-63

Bazelyan E M and Raizer Y P 1998 Spark Discharge (Boca Raton, FL: CRC Press)

Bazelyan E M and Raizer Y P 2000 Lightning Physics and Lightning Protection (Bristol: IOP Publishing)

Béjot P, Cormier E, Hertz E, Lavorel B, Kasparian J, Wolf J P and Faucher O 2013 *Phys. Rev. Lett.* **110** 043902

Bergé L, Skupin S, Nuter R, Kasparian J and Wolf J P 2007 Rep. Prog. Phys. 70 1633–713

Berti N, Ettoumi W, Hermelin S, Kasparian J and Wolf J P 2015 *Phys. Rev.* A **91** 063833

Bodrov S, Bukin V, Tsarev M, Murzanev A, Garnov S, Aleksandrov N and Stepanov A 2011 *Opt. Express* **19** 6829

Bohren C R and Huffman D R 1998 Absorption and Scattering of Light by Small Particles (New York: Wiley)

Bondiou A and Gallimberti I 1994 *J. Phys. D: Appl. Phys.* **27** 1252 Bourayou R *et al* 2005 *J. Opt. Soc. Am.* B **22** 369–77

Boutou V, Favre C, Hill S C, Pan Y, Chang R K and Wolf J P 2002 Appl. Phys. B **7552** 145–53

Boyd R W 2008 *Non-Linear Optics* 3rd edn (New York: Elsevier) Braun A, Korn G, Liu X, Du D, Squier J and Mourou G 1995 *Opt. Lett.* **20** 73–5

Bree C, Demircan A and Steinmeyer G 2011 *Phys. Rev. Lett.* **106** 183902

Brelet Y, Houard A, Arantchouk L, Foerstier B, Liu Y, Prade B, Carbonnel J, Andre Y B and Mysyrowicz A 2012 *Appl. Phys. Lett.* **100** 181112

Burch D S, Smith S J and Branscom L M 1958 *Phys. Rev.* 112 171–5

Camino A, Li S, Hao Z and Lin J 2015 *Appl. Phys. Lett.* **106** 021105

Canagaratna M R et al 2007 Mass Spectrom. Rev. 26 185–222 Chelkowski S, Bandrauk A and Corkum P 1990 Phys. Rev. Lett. 65 2355

Cheng Y H, Wahlstrand J K, Jhajj N and Milchberg H M 2013 *Opt. Express* **21** 4740

Chiao R Y, Garmire E and Townes C H 1964 *Phys. Rev. Lett.* 13 479–82

Chin S L 2010 Femtosecond Laser Filamentation (Springer Series on Atomic, Optical and Plasma Physics vol 55) (Berlin: Springer)

Chin S L, Hosseini S A, Liu W, Luo Q, Theberge F, Akozbek N, Becker A, Kandidov V P, Kosareva O G and Schroeder H 2005 *Can. J. Phys.* **83** 863–905

Chin S L, Petit S, Borne F and Miyazaki K 1999 *Japan. J. Appl. Phys.* **38** L126

Chin S L, Talebpour A, Yang J, Petit S, Kandidov V P,

Kosareva O G and Tamarov M P 2002 *Appl. Phys.* B **74** 67–76 Chin S L *et al* 2009 *Appl. Phys.* B **95** 1–12

Chin S L et al 2012 Laser Phys. 22 1-53

Chiwa M, Kondo H, Ebihara N and Sakugawa H 2008 *Environ. Monit. Assess.* **140** 349

Clark I D and Noxon J F 1971 Science 174 941-4

Clegg S L, Brimblecombe P and Wexler A S 1998 *J. Phys. Chem.* A 102 2137–54

Clegg S L and Wexler A S 2011 *J. Phys. Chem.* **115** 3393–60 Clerici M *et al* 2015 *Sci. Adv.* **1** e1400111

Coble B B 1997 Benign Weather Modification (Alabama: Air

University Press, Maxwell Air Force Base) Comtois D et al 2000 Appl. Phys. Lett. **76** 819–21

Comtois D et al 2003a IEEE Trans. Plasma Sci. 31 377-86

Comtois D et al 2003b IEEE Trans. Plasma Sci. 31 387-95

Couairon A and Bergé L 2002 Phys. Rev. Lett. 88 135003

- Couairon A and Mysyrowicz A 2007 *Phys. Rep.* **441** 47–189 Courvoisier F, Boutou V, Kasparian J, Salmon E, Méjean G, Yu J and Wolf J P 2003a *Appl. Phys. Lett.* **83** 213–5
- Courvoisier F, Boutou V, Favre C, Hill S C and Wolf J P 2003b Opt. Lett. 28 206–8
- Courvoisier F, Boutou V, Wood V, Bartelt A, Roth M, Rabitz H and Wolf J P 2005 *Appl. Phys. Lett.* **87** 063901
- Crutzen P J 2006 Clim. Change 77 211
- Crutzen P J and Ramanathan V 2003 Science 302 1679-81
- Curran E B, Holle R L and Lopez R E 1997 Lightning fatalities, injuries and damage reports in the United States, 1959–1994 NOAA Technical Memorandum No. NWS SR-193
- Czys R R 1995 Rev. Geophys. 33 823-32
- Daigle J F, Kamali Y, Bernhardt J, Liu W W, Marceau C, Azarm A and Chin S L 2008 *Opt. Commun.* **281** 3327–35
- Daigle J F, Kamali Y, Chateauneuf M, Tremblay G, Theberge F, Dubois J, Roy G and Chin S L 2009 *Appl. Phys.* B **97** 701–13
- Daigle J F, Theberge F, Lassonde P, Kieffer J C, Fujii T, Fortin J, Chateauneuf M and Dubois J 2013 *Appl. Phys. Lett.* **103** 184101 DeCarlo P *et al* 2006 *J. Anal. Chem.* **78** 8281–9
- De la Cruz L, Schubert E, Mongin D, Klingebiel S, Schultze S, Metzger T, Michel K, Kasparian J and Wolf J P 2016 *Appl. Phys. Lett.* **109** 251105
- Derwent R G, Dernie J I R, Dollard G J, Dumitrean P, Mitchell R F, Murrells T P, Telling S P and Field R A 2014 *Atmos. Environ.* **99** 239–47
- Dicaire I, Nakamura R, Arikawa Y, Okada K, Itahashi T and Summerer L 2015 *Acta Astron.* **107** 208–17
- Diels J C, Bernstein R, Stahlkopf E and Zhao X M 1997 Sci. Am. 277 50-5
- Diels J C and Zhao X M 1992 US Patent 5,175,664
- Dicaire I, Jukna V, Praz C, Milian C, Summerer L and Couairon A 2016 *Laser Photonics Rev.* **10** 481–93
- Dogariu A, Michael J B, Scully M O and Miles R B 2011 *Science* 331 442–5
- Durand M et al 2013 Opt. Express 21 26836-45
- Dutcher C S, Wexler A S and Clegg S L 2010 J. Phys. Chem. A 114 12216–30
- Dwyer J R 2005 Geophys. Res. Lett. 32 L20808
- Dwyer J R and Uman M A 2014 Phys. Rep. 534 147-241
- Dwyer J R et al 2003 Science 299 694-7

37 1130–2

- Eeltink D, Berti N, Marchiando N, Hermelin S, Gateau J, Brunetti M, Wolf J P and Kasparian J 2016 *Phys. Rev.* A 94 033806
- ELI-Whitebook 2011 *Science and Technology with Ultra-Intense Lasers* ed Mourou G A *et al* (Berlin: Thoss Media Publishing)
 Eto S, Zhidkov A, Oishi Y, Miki M and Fujii T 2012 *Opt. Lett.*
- Ettoumi W, Kasparian J and Wolf J P 2015 *Phys. Rev. Lett.* 115 033902
- Faccio D, Averchi A, Lotti A, Di Trapani P, Couairon A, Papazoglo D and Tzortzakis S 2008 *Opt. Express* 16 1565
- Favre C, Boutou V, Hill S C, Zimmer W, Krenz M, Lambrecht H, Yu J, Chang R K, Woeste L and Wolf J P 2002 Phys. Rev. Lett. 89 035002
- Farley F J M 1951 *Proc. R. Soc.* A **207** 527–39
- Feng C Y, Xu X Z and Diels J C 2014 Opt. Lett. 39 3367-70
- Fieux R, Gary C and Hubert P 1975 Nature 257 212
- Fieux R P, Gary C H, Hutzler B P, Eybert-Berard A R, Hubert P L, Meesters A C, Perroud P H, Hamelin J H and Person M 1978 IEEE Trans. Power Appar. Syst. 97 725–33
- Fishman G J et al 1994 Science 264 1313-6
- Forestier B et al 2012 AIP Adv. 2 012151
- Frejafon E et al 1998 Eur. Phys. J. D 4 231-8
- Fresnet F, Baravian G, Magne L, Pasquiers S, Postel C, Puech V and Rousseau A 2002 *Plasma Sources Sci. Technol.* 11 152–60
- Fujii T, Miki M, Goto N, Zhidkov A, Fukuchi T, Oishi Y and Nemoto K 2008 *Phys. Plasma* **15** 013107

- Fujimoto M, Aoshima S and Tsuchiya Y 2002 *Opt. Lett.* **27** 309–11 Garstang M, Bruintjes R, Serafin R, Orville H, Boe B, Cotton W and Warburton J 2004 *Bull. Am. Meteorol. Soc.* **85** 647–55
- Geerts B, Miao Q, Yang Y, Rasmussen R and Breed D 2010 J. Atmos. Sci. 67 3286–302
- Gravel J F, Luo Q, Boudreau D, Tang X P and Chin S L 2004 Anal. Chem. 76 4799–805
- Guo K M, Lin J Q, Hao Z Q, Gao X, Zhao Z M, Sun C K and Li B Z 2012 *Opt. Lett.* **37** 259–61
- Gurevich A V, Milikh G M and Roussel-Dupre R A 1992 Phys. Lett. A 165 463–8
- Gurevich A V and Zybin K R 2005 *Phys. Today* **58** 37–43 Haberberger D, Tochitsky S and Joshi C 2010 *Opt. Express* **18** 17865–75
- Hao Z Q, Zhang J, Li Y T, Lu X, Yuan X H, Zheng Z Y, Wang Z H, Ling W J and Wei Z Y 2005 *Appl. Phys.* B **80** 627–30
- Hemmer P R, Miles R B, Polynkin P, Siebert T, Sokolov A V, Sprangle P and Scully M O 2011 *Proc. Natl Acad. Sci. USA* 108 3130–4
- Henin S et al 2010 Appl. Phys. B 100 77-84
- Henin S et al 2011 Nat. Commun. 2 456
- Henriksson M, Daigle J F, Theberge F, Chateauneuf M and Dubois J 2012 *Opt. Express* **20** 12721–8
- Hercher M 1964 J. Opt. Soc. Am. 54 563
- Hill S C, Boutou V, Yu J, Ramstein S, Wolf J P, Pan Y, Holler S and Chang R K 2000 *Phys. Rev. Lett.* **85** 54
- Hoppel W A and Dinger J E 1973 J. Atmos. Sci. 30 331–4
- Houard A, Jukna V, Point G, Andre Y B, Klingbeil S, Schultze M, Michel K, Metzger T and Mysyrowicz A 2016 *Opt. Express* **24** 7437–48
- Houard A et al 2008 Phys. Rev. A 78 033804
- Hua W et al 2008 Atmos. Chem. Phys. 8 6755-73
- Hubert P, Laroche P, Eybert-Berard A and Barret L 1984 *J. Geophys. Res.* **89** 2511–21
- Ionin A A, Iroshnikov N G, Kosareva O G, Larichev A V, Mokrousova D V, Panov N A, Seleznev L V, Sinitsyn D V and Sunchugasheva E S 2013 J. Opt. Soc. Am. 30 2257–62
- Ionin A A, Kudryashov S I, Levchenko A O, Seleznev L V, Shutov A V, Sinitsyn D V, Smetanin I V, Ustinovsky N N and Zvorykin V D 2012 Appl. Phys. Lett. 100 104105
- IPCC 2013 Intergovernmental Panel on Climate Change, 5th
 Assessment Report ed T F Stocker, D Qin, G-K Plattner,
 M Tignor, S K Allen, J Boschung, A Nauels, Y Xia, V Bex
 and P M Midgley (Cambridge: Cambridge University Press)
 p 1535
- Javan A and Kelley P L 1966 IEEE J. Quantum Electron. 2 470–3Jeon C, Harper D, Lim K, Durand M, Chini M, Baudelet M and Richardson M 2015 J. Opt. 17 055502
- Jhajj N, Rosenthal E W, Birnbaum R, Wahlstrand J K and Milchberg H M 2014a *Phys. Rev.* X **4** 011027
- Jhajj N, Wahlstrand J K and Milchberg H M 2014b *Opt. Lett.* **39** 6312–5
- Ji Z, Zhu J, Wang Z, Ge X, Wang W, Liu J and Li R 2010 *Plasma Sci. Technol.* 12 295–9
- Joly P, Petrarca M, Vogel A, Pohl T, Nagy T, Justforgues Q, Simon P, Kasparian J, Weber K and Wolf J P 2013 Appl. Phys. Lett. 102 091112
- Ju J J, Liu J, Wang C, Sun H, Wang W, Ge X, Li C, Chin S L, Li R and Xu Z 2012 Opt. Lett. 37 1214–6
- Ju J J, Liu J, Wang C, Sun H, Wang W, Ge X, Li C, Chin S L, Li R and Xu Z 2013a App. Phys. B 110 375–80
- Ju J J, Sun H, Sridharan A, Wang T J, Wang C, Liu J, Li R, Xu Z and Chin S L 2013b *Phys. Rev.* E **88** 062803
- Ju J J et al 2014 Appl. Phys. B 117 1001-7
- Ju J J et al 2016 Sci. Rep. 6 25417
- Judson R S and Rabitz H 1992 Phys. Rev. Lett. 68 1500-3
- Kafalas P and Ferdinand A 1973 Appl. Opt. 12 29–33
- Kamali Y et al 2009 Opt. Commun. 282 2062–5

- Kandidov V P, Kosareva O G, Tamarov M P, Brodeur A and Chin S L 1999 *Quantum Electron.* **29** 911–5
- Kartashov D, Alisauskas S, Andriukaitis G, Pugzlys A, Shneider M, Zheltikov A, Chin S L and Baltuska A 2012 *Phys. Rev.* A 86 033831
- Kartashov D, Alisauskas S, Pugzlys A, Shneider M N and Baltuska A 2015 J. Phys. B 48 094016
- Kartashov D, Ališauskas S, Pugžlys A, Voronin A, Zheltikov A, Petrarca M, Béjot P, Kasparian J, Wolf J P and Baltuška A 2013 *Opt. Lett.* **38** 3194–7
- Kasparian J, Frejafon E, Rambaldi P, Yu J, Vezin B, Wolf J P, Ritter P and Viscardi P 1998a *Atmos. Environ.* 32 2957–67
- Kasparian J, Kramer B, Leisner T, Rairoux P, Boutou V, Vezin B and Wolf J P 1998b *J. Opt. Soc. Am.* B **15** 1918–22
- Kasparian J, Rohwetter P, Woeste L and Wolf J P 2012 *J. Phys. D: Appl. Phys.* **45** 293001
- Kasparian J, Sauerbrey R and Chin S L 2000a Appl. Phys. B 71 877
- Kasparian J and Wolf J P 2008a Opt. Express 16 466–93
- Kasparian J and Wolf J P 1998 Opt. Commun. 152 355-60
- Kasparian J et al 1997 Phys. Rev. Lett. 78 2952-5
- Kasparian J et al 2000b Opt. Lett. 25 1397
- Kasparian J et al 2003 Science 301 61-4
- Kasparian J et al 2008b J. Eur. Opt. Soc. 3 08035
- Kasparian J et al 2008c Opt. Express 16 5757-63
- Keith D 2013 A Case for Climate Engineering (Boston, MA: MIT Press)
- Keldysh L V 1965 Sov. Phys.—JETP 20 1307
- Kirkby J et al 2016 Nature 533 521
- Kohler H 1936 Trans. Faraday Soc. 32 1152-61
- Kohler C, Guichard R, Lorin E, Chelkowski S, Bandrauk A D, Bergé L and Skupin S 2013 *Phys. Rev.* A **87** 043811
- Kolesik M and Moloney J V 2004a Opt. Lett. 29 590-2
- Kolesik M and Moloney J V 2004b Phys. Rev. E 70 036604
- Kolesik M, Moloney J V and Mlejnek M 2002 *Phys. Rev. Lett.* **89** 283902
- Kolmogorov A N 1991 Proc. R. Soc. A 434 9-13
- Koopman D W and Wilkerson T D 1971 J. Appl. Phys. 42 1883-6
- Kossyi I A, Kostinsky A, Matveyev A A and Silakov V P 1992 *Plasma Sources Sci. Technol.* **1** 207
- Krider P 2003 Science 299 669
- Kulmala M, Laaksonen A, Korhonen P, Vesala T, Ahonen T and Barrett J C 1993 *J. Geophys. Res.* **98** 22949–58
- Kulmala M, Vehkamaki H, Petaja T, Dal Maso M, Lauri A, Kerminen V M, Birmili W and McMurry P H 2004 *J. Aerosol. Sci.* **35** 143–76
- Kurten T, Torpo L, Ding C G, Vehkamaki H, Sundberg M R, Laasonen K and Kulmala M 2007 *J. Geophys. Res.* 112 04210
- Kundzewicz Z W et al 2014 Hydrol. Sci. J. 59 1–28
- Kwok H S, Rossi T M, Lau W S and Shaw D T 1988 Opt. Lett. 13 192–5
- Laaksonen A, Korhonen P, Kulmala M and Charlson R 1998 J. Atmos. Sci. 55 853
- La Fontaine B, Vidal F, Jiang Z, Chien C Y, Comtois D, Desparois A, Johnston T W, Kieffer J C, Pepin H and Mercure H P 1999 *Phys. Plasmas* **6** 1615–21
- La Fontaine B et al 2000 J. Appl. Phys. 88 610-5
- Lahav O, Levi L, Orr I, Nemirovsky R A, Nemirovsky J, Kaminer I, Segev M and Cohen O 2014 *Phys. Rev.* A **90** 021801
- Lalande P, Bondiou-Clergerie A, Laroche P, Eybert-Berard A, Berlandis J P, Bador B, Bonamy A, Uman M A and Rakov V A 1998 J. Geophys. Res. 103 14109–15
- Lallemand P and Bloembergen N 1965 *Phys. Rev. Lett.* **15** 1010–2 Laurain A, Scheller M and Polynkin P 2014 *Phys. Rev. Lett.* **113** 253901
- Leach D H, Chang R K, Acker W P and Hill S C 1993 *J. Opt. Soc. Am.* 10 34–45
- Leisner T et al 2013 Proc. Natl Acad. Sci. USA 110 10106–10 Levis R J, Menkir G M and Rabitz H 2001 Science 292 709–13

- Li H L, Chu W, Xu H L, Cheng Y, Chin S L, Yamanouchi K and Sun H B 2016 Sci. Rep. 6 27340
- Li H W, Harris D A, Xu B, Wrzesinski P J, Lozovoy V V and Dantus M 2008 Opt. Express 16 5499–504
- Liang H K, Weerawarne D L, Krogen P, Grynko R I, Lai C J, Shim B, Kartner F X and Hong K H 2016 *Optica* 3 678–81
- LLR 2017 Laser lightning rod project http://llr-fet.eu/
- Lu X et al 2015 Sci. Rep. 5 15515
- Libbrecht K G 2006 Rep. Prog. Phys. 68 855-95
- Lindinger A, Hagen J, Socaciu L, Bernhardt T, Woeste L and Leisner T 2004 Appl. Opt. 43 5263
- Liou K N 1986 Mon. Weather Rev. 114 1167-99
- Liu W and Chin S L 2005 Opt. Express 13 5750
- Liu X L et al 2012 Opt. Express 20 5968-73
- Liu Y, Brelet Y, Point G, Houard A and Mysyrowicz A 2013 Opt. Express 21 22791–8
- Liu Y, Ding P J, Lambert G, Houard A, Tikhonchuk V and Mysyrowicz A 2015 *Phys. Rev. Lett.* **115** 133203
- Liu Y, Sun H, Liu J, Liang H, Ju J, Wang T, Tian Y, Wang C, Chin S L and Li R 2016 *Opt. Express* **24** 7364–73
- Lorin E, Chelkowski S and Bandrauk A 2007 Comput. Phys. Commun. 177 908–32
- Lorin E, Chelkowski S, Zaoui E and Bandrauk A 2012 *Physica* D **241** 1059–71
- Lorin E, Lytova M, Memarian A and Bandrauk A 2015 J. Phys. A 48 105201
- Loriot V, Hertz E, Faucher O and Lavorel B 2009 *Opt. Express* 17 13429–34
- Loriot V, Hertz E, Faucher O and Lavorel B 2010 *Opt. Express* 18 3011–2
- Lowke J L 2004 IEEE Trans. Plasma Sci. 32 4-17
- Luderer J C 2001 Untersuchung der Ionisationsspur in einem Weißlichtkanal mit einer Nebelkammer *Physik Diplom Thesis* Freie Universitat Berlin
- Luo Q, Liu W and Chin S L 2003 Appl. Phys. B **76** 337–40
- Luo Q, Xu H L, Hosseini S A, Daigle J F, Theberge F, Sharifi M and Chin S L 2006 *Appl. Phys.* B **82** 105–9
- Ma Y Y, Lu X, Xi T T, Gong Q H and Zhang J 2008 Opt. Express
- Maioli P, Salamé R, Lascoux N, Salmon E, Béjot P, Kasparian J and Wolf J P 2009 *Opt. Express* 17 4726–31
- Marburger J H 1975 Prog. Quantum Electron. 4 35-110
- Marshall T C and Rust R D 1991 J. Geophys. Res. 96 22297-306
- Matthews M, Henin S, Pomel F, Theberge F, Lassonde P, Daigle J F, Kieffer J C, Kasparian J and Wolf J P 2013 *Appl. Phys. Lett.* **103** 264103
- Matthews M, Pomel F, Wender C, Kiselev A, Duft D, Kasparian J, Wolf J P and Leisner T 2016 *Sci. Adv.* **2** e1501912
- Measures R M 1992 *Laser Remote Sensing* (Malabar, FL: Krieger Publishing Company)
- Méchain G, Couairon A, André Y B, D'Amico C, Franco M, Prade B, Tzortzakis S, Mysyrowicz A and Sauerbrey R 2004 Appl. Phys. B **79** 379–82
- Méjean G, Kasparian J, Yu J, Frey S, Salmon E and Wolf J P 2004 Appl. Phys. B **78** 535–7
- Méjean G et al 2003 Appl. Phys. B 76 357-9
- Méjean G et al 2005 Phys. Rev. E 72 026611
- Méjean G et al 2006 Appl. Phys. Lett. 88 021101
- Metzger T 2016 TRUMPF Scientific, ISUILS 15 Conf. (Cassis)
- Miao Q and Geerts B 2013 Adv. Atmos. Sci. 30 1025-38
- Miki M, Aihara Y and Shindo T 1993 *J. Phys. D: Appl. Phys.* **26** 1244–52
- Miki M, Shindo T and Aihara Y 1996 *J. Phys. D: Appl. Phys.* **29** 1984–96
- Miki M and Wada A 1996 J. Appl. Phys. 80 3208-14
- Mitrofanov A V et al 2015a Sci. Rep. 5 8368
- Mitrofanov A V et al 2015b Opt. Lett. 40 2068-71
- Mitryukovskiy S, Liu Y, Ding P J, Houard A and Mysyrowicz A 2014 *Opt. Express* **22** 12750–9

- Moehler O et al 2003 Atmos. Chem. Phys. 3 211–23
- Mongin D, Slowik J G, Schubert E, Brisset J G, Berti N, Moret M, Prevot A S H, Baltensperger U, Kasparian J and Wolf J P 2015 *Sci. Rep.* **5** 14978
- Mongin D, Schubert E, Berti N, Kasparian J and Wolf J P 2017 *Phys. Rev. Lett.* **118** 133902
- Mourou G 2015 Eur. Phys. J. 224 2527-8
- Nagy T and Simon P 2009 Opt. Express 17 8144
- National Research Council 2003 Critical Issues in Weather Modification Research (Washington, DC: National Academies)
- Newman M M, Stahmann J R, Robb J D, Lewis E A, Martin S G and Zinn S V 1967 *J. Geophys. Res.* **72** 4761–4
- Ng N L, Canagaratna M R, Jimenez J L, Chhabra P S, Seinfeld J H and Worsnop D R 2011 *Atmos. Chem. Phys.* 11 6465–74
- Ng N L, Canagaratna M, Zhang Q, Jimenez J and Tian J E A 2010 *Atmos. Chem. Phys.* **10** 4625–41
- Nibbering E T J, Curley P F, Grillon G, Prade B S, Franco M A, Salin F and Mysyrowicz A 1996 *Opt. Lett.* **21** 62
- NLSI 2009 *Lightning Protection for Engineers* (Louisville, CO: National Lightning Safety Institute)
- NOAA 1998 Report No 18, MIT
- NRC, National Research Council 2003 *Critical Issues in Weather Modification Research* (National Academy Press) Washington DC (USA) 123pp
- Nurhuda M, Suda A, Hatayama M, Nagasaka K and Midorikawa K 2002a *Phys. Rev.* A **66** 023811
- Nurhuda M, Suda A and Midorikawa K 2002b *RIKEN Rev.* **48** 40 Nuter R and Bergé L 2006 *J. Opt. Soc. Am.* B **23** 874
- Panagiotopoulos P, Schuh K, Kolesik M and Moloney J V 2016 J. Opt. Soc. Am. 33 2154–61
- Panagiotopoulos P, Whalen P, Kolesik M and Moloney J V 2015 Nat. Photon. 9 543
- Papeer J, Botton M, Gordon D, Sprangle P, Zigler A and Henis Z 2014 *New J. Phys.* **16** 123046
- Papeer J, Botton M, Gordon D, Sprangle P, Zigler A and Henis Z 2015 *New J. Phys.* 17 089501
- Paschen F 1889 Ann. Phys. 273 69
- Paunescu G, Spindler G, Riede W, Schroder H and Giesen A 2009 Appl. Phys. B 96 175–83
- Penano J, Sprangle P, Hafizi B, Gordon D, Fernsler R and Scully M 2012 *J. Appl. Phys.* 111 033105
- Pepin H et al 2001 Phys. Plasmas 8 2532-9
- Perelomov A M and Popov V S 1967 Sov. Phys.—JETP 25 336 Perelomov A M, Popov V S and Terentev M V 1967 Sov. Phys.— JETP 24 207
- Petit Y, Henin S, Kasparian J and Wolf J P 2010 Appl. Phys. Lett. 97 021108
- Petrarca M et al 2011 Appl. Phys. Lett. 99 141103
- Petrarca M et al 2014 Appl. Phys. B 114 319-25
- Pfeiffer T, Gallman L, Abel M J, Neumark M and Leone S R 2006 Opt. Lett. 31 2326
- Pigeon J, Tochitsky S Y and Joshi C 2015 Opt. Lett. 40 5730-3
- Pinnick R G, Biswas A, Armstrong R L, Jennings S G,
- Pendleton J D and Fernandez G 1990 Appl. Opt. 29 918–25
- Point G, Liu Y, Brelet Y, Mitryukovskiy S, Ding P J, Houard A and Mysyrowicz A 2014 *Opt. Lett.* **39** 1725–8
- Point G, Milian C, Couairon A, Mysyrowicz A and Houard A 2015 J. Phys. B 48 094009
- Point G, Thouin E, Mysyrowicz A and Houard A 2016 *Opt. Express* **24** 6271–82
- Polynkin P and Moloney J V 2011 Appl. Phys. Lett. 99 151103
- Pruppacher H R and Klett J D 1997 *Microphysics of Clouds and Precipitation* (Dordrecht: Kluwer)
- Pustovalov V K and Khorunzhii I A 1992 Int J. Heat Mass Transf. 35 583–9
- Qiu J and Cressey D 2008 Nature 453 970-4
- Quinn M N, Jukna V, Ebisuzaki T, Dicaire I, Soulard R,
 - Summerer L, Couairon A and Mourou G 2015 *Eur. Phys. J.* **224** 2645–55
- Rabeony H and Mirabel P 1987 J. Phys. Chem. 91 1815–8

- Rairoux P et al 2000 Appl. Phys. B 71 573-80
- Raizer Y P 1965 Sov. Phys.—JETP 21 1009
- Rakov V A and Uman M A 2003 *Lightning: Physics and Effects* (Cambridge: Cambridge University Press)
- Rambo P, Biegert J, Kubecek V, Schwarz J, Bernstein A, Diels J C, Bernstein R and Stahlkopf K 1999 J. Opt. Technol. 66 194–8
- Rambo P, Schwarz J and Diels J C 2001 J. Opt. A 3 146–58
- Rastegari A, Schubert E, Feng C, Mongin D, Kamer B, Kasparian J, Wolf J P, Arissian L and Diels J C 2016 *Proc. SPIE 9727*, *Laser Resonators, Microresonators, and Beam Control XVIII* (22 April 2016) p 97271H
- Reiss H, Marvin D C and Heist R H 1977 *J. Colloid Interface Sci.* 58 125–41
- Richter M, Patchkovskii S, Morales F, Smirnova O and Ivanov M 2013 New J. Phys. 15 083012
- Rison W, Thomas R J, Krehbiel P R, Hamlin T and Harlin J 1999 Geophys. Res. Lett. 26 3573–6
- Rizk F A M 1994 IEEE Trans. Power Deliv. 9 162-93
- Rodriguez M et al 2002 Opt. Lett. 27 772-4
- Rodriguez M et al 2004 Phys. Rev. E 69 036607
- Rohwetter P, Kasparian J, Woste L and Wolf J P 2011 *J. Chem. Phys.* **135** 134703
- Rohwetter P et al 2010 Nat. Photon. 4 451-6
- Rosenthal E W, Jhajj N, Larkin I, Zahedpour S, Wahlstrand J K and Milchberg H M 2016 Opt. Lett. 41 3905–11
- Rosenthal E W, Jhajj N, Wahlstrand J K and Milchberg H M 2014 *Optica* 1 5–9
- Roth M, Guyon L, Roslund J, Boutou V, Courvoisier F, Wolf J P and Rabitz H 2009 Phys. Rev. Lett. 102 253001
- Saathoff H et al 2013 Atmos. Chem. Phys. 13 4593-604
- Saba M F, Pinto O, Solorzano N N and Eybert-Berard A 2005 *Atmos. Res.* **76** 402
- Salame R, Lascoux N, Salmon E, Ackermann R, Kasparian J and Wolf J P 2007 Appl. Phys. Lett. 91 171106
- Sasaki A, Kishimoto Y, Takahashi E, Kato S, Fujii T and Kanazawa S 2010 *Phys. Rev. Lett.* **105** 075004
- Saum K A and Koopman D W 1972 Phys. Fluids 15 2077
- Schmitt-Sody A, French D, White W, Lucero A, Roach W P and Hasson V 2015 Appl. Phys. Lett. 106 124101
- Schubert E, Brisset J G, Matthews M, Courjaud A, Kasparian J and Wolf J P 2016a *Phys. Rev.* A **94** 033824
- Schubert E, de la Cruz L, Mongin D, Klingebiel S, Schultze M, Metzger T, Michel K, Kasparian J and Wolf J P 2016b *Phys. Rev.* A **94** 043808
- Schubert E, Mongin D, Kasparian J and Wolf J P 2015 *Opt. Express* 23 28640–8
- Scully M O, Kattawar G W, Lucht R P, Opatrny T, Pilloff H, Rebane A, Sokolov A V and Zubairy M S 2002 Proc. Natl Acad. Sci. USA 99 10994–1001
- Seinfeld J H and Pandis S N 2006 Atmospheric Chemistry and Physics 2nd edn (Hoboken, NJ: Wiley)
- Scheller M, Born N, Cheng W B and Polynkin P 2014 *Optica* 1 125–8
- Schnaiter M, Buttner S, Mohler O, Skrotzki J, Vragel M and Wagner R 2012 Atmos. Chem. Phys. 12 10465–84
- Schuh K, Moloney J V and Koch S W 2016 *Phys. Rev.* E **93** 013208
- Shen Y R and Shaham Y J 1965 *Phys. Rev. Lett.* **15** 1008–10 Shilling J E, Chen Q, King S M, Rosenoern T, Kroll J H,
 - Worsnop D R, McKinney K A and Martin S T 2008 Atmos. Chem. Phys. 8 2073–88
- Shindo T, Aihara Y, Miki M, Suzuki T, Mousa A M, Lai L L and House H 1993a *IEEE Trans. Power Deliv.* **8** 311–7
- Shindo T, Miki M, Aihara Y and Wada A 1993b *IEEE Trans. Power Deliv.* 8 2016–22
- Shneider M N, Baltuska A and Zheltikov A M 2011 J. Appl. Phys. 110 083112
- Shumakova V, Malevich P, Alisauskas S, Voronin A, Zheltikov A M, Faccio D, Kartashov D, Baltuska A and Pugzlys A 2016 *Nat. Commun.* **7** 12877

Silaeva E P, Shlenov S A and Kandidov V P 2010 *Appl. Phys.* B **101** 393–401

Singh P I and Knight C P 1988 AIAA J. 18 96–100

Skupin S, Bergé L, Peschel U and Lederer F 2004a *Phys. Rev. Lett.* 93 023901

Skupin S et al 2004b Phys. Rev. E 70 046602

Spott A, Jaron-Becker A and Becker A 2014 *Phys. Rev.* A 90 013426

Sprangle P, Penano J, Hafizi B, Gordon D and Scully M 2011 Appl. Phys. Lett. 98 211102

Stockel P, Weidinger I M, Baumgärtel H and Leisner T 2005 *J. Phys. Chem.* A **109** 2540–6

Sugiyama K, Fujii T, Miki M, Zhidkov A, Yamaguchi M, Hotta E and Nemoto K 2010 Phys. Plasmas 17 043108

Sun H et al 2016 Opt. Express 24 20494-506

Takahashi E, Kato S, Furutani H, Sasaki A, Kishimoto Y, Takada K, Matsumura S and Sasaki H 2011 J. Phys. D: Appl. Phys. 44 302001

Talanov V I 1965 JETP Lett. 2 138

Theberge F, Châteauneuf M, Ross V, Mathieu P and Dubois J 2008 Opt. Lett. 33 2515–7

Theberge F, Daigle J F, Kieffer J C, Vidal F and Chateauneuf M 2017 Sci. Rep. 7 40063

Thoni L, Brang P, Braun S, Seitler E and Rihm B 2004 *Environ. Monit. Assess.* **98** 93–107

Townsend J S 1915 *Electricity in Gases* (Oxford: Oxford University Press)

Traverso A J *et al* 2012 *Proc. Natl Acad. Sci. USA* **109** 15185–90 Trostl W *et al* 2016 *Nature* **533** 527–31

Tsuchiya H et al 2007 Phys. Rev. Lett. 99 165002

Tzortzakis S, Prade B, Franco M and Mysyrowicz A 2000 Opt. Commun. 181 123

Uchida S, Shimada Y, Yasuda H, Motokishi S, Yamanaka C, Yamanaka T, Kawasaki Z and Tsubakimoto K 1999 *J. Opt. Technol.* **66** 199–202

Uman M A and Rakov V A 2005 *Lightning: Physics and Effects* (Cambridge: Cambridge University Press)

Vaill J R, Tidman D A, Wilkerson T D and Koopman D W 1970 Appl. Phys. Lett. 17 20

Valle Brozas F, Salgado C, Apiñaniz J I, Carpentier A V, Sánchez Albaneda M, Roso L, Raposo C, Padilla C and Peralta Conde A 2016 Laser Phys. 26 055602

Vidal F, Comtois D, Chien C-Y, Desparois A, Fontaine B, Johnston T W, Kieffer J C, Mercure H P, Pepin H and Rizk F A 2000 IEEE Trans. Plasma Sci. 28 418

Vincotte A and Bergé L 2004 Phys. Rev. A 70 061802

Wahlstrand J K, Cheng Y H and Milchberg H M 2012 *Phys. Rev.* A **85** 043820

Wang D, Ushio T, Kawasaki Z I, Matsuura K, Shimada Y, Uchida S, Yamanaka C, Izawa Y, Sonoi Y and Simokura N 1995 J. Atmos. Sol.-Terr. Phys. 57 459–66

Wang D et al 1994 J. Geophys. Res. 99 16907–12

Wang T J, Ju J J, Daigle J F, Yuan S, Li R X and Chin S L 2013 Laser Phys. Lett. 10 125401

Wang T J et al 2015 Sci. Rep. 5 18681

Warren W S, Rabitz H and Daleh M 1993 Science 259 1581-9

Webb B, Bradford J, Lim K, Bodnar N, Vaupel A, McKee E, Baudelet M, Durand M, Shah L and Richardson M 2014 Frontiers in Optics 2014, OSA Technical Digest, paper SM1F vol 6 (online) (Optical Society of America)

Weitkamp C 2005 Lidar: Range-Resolved Optical Remote Sensing of the Atmosphere (Berlin: Springer)

Wen F C, McLaughlin T and Katz J L 1978 Science 200 769–71

Wille H, Rodriguez M, Kasparian J, Mondelain D, Yu J, Mysyrowicz A, Sauerbrey R, Wolf J P and Woeste L 2002 Eur. Phys. J. Appl. Phys. 20 183–90

Wilson C T R 1899 Phil. Trans. R. Soc. A 192 403-53

Woeste L et al 1997 Laser Optoelektron. 29 51-3

Wolf J P 2000 UV-DIAL-lidar techniques for air pollution monitoring *Encyclopedia of Analytical Chemistry* vol 3, ed R A Meyers (New York: Wiley) pp 2226–47

Wolk J and Strey R 2001 J. Phys. Chem. B 105 11683-701

Xu H L et al 2007 Appl. Phys. Lett. 90 101106

Xu H L, Azarm A, Bernhardt J, Kamali Y and Chin S L 2009 Chem. Phys. 360 171

Xu H L and Chin S L 2011 Sensors 11 32-53

Xu H L, Lotstedt E, Iwasaki A and Yamanouchi K 2015 Nat. Commun. 6 8347

Yablonovitch E and Bloembergen N 1972 *Phys. Rev. Lett.* **29** 907–10

Yao J P, Zeng B, Xu H L, Li G H, Chu W, Ni J L, Zhang H S, Chin S L, Cheng Y and Xu Z Z 2011 *Phys. Rev.* A 84 051802

Yang J, Zeng T, Lin L and Liu W W 2015 *Opt. Express* **23** 25628–34

Yoshihara K 2005 Chem. Lett. 34 1370

Yoshihara K, Sakamoto Y, Kawasaki M, Takatori Y, Kato S and Kajii Y 2014 *Bull. Chem. Soc. Japan* **87** 593602

Yoshihara K, Takatori Y and Kajii Y 2012 *Bull. Chem. Soc. Japan* **85** 1155–9

Yuan S, Wang T, Teranishi Y, Sridharan A, Lin S H, Zeng H and Chin S L 2013 Appl. Phys. Lett. 102 224102

Zahedpour S, Wahlstrand J K and Milchberg H M 2014 *Phys. Rev. Lett.* **112** 143601

Zemlyanov Y G, Kabanov A M and Armstrong R L 1996 Appl. Opt. 35 6062–7

Zhang Z, Lu X, Liang W X, Hao Z Q, Zhou M L, Wang Z H, Liu X and Zhang J 2009 *Opt. Express* 17 3461–8

Zhang H S et al 2013 Phys. Rev. X 3 041009

Zhao X M, Diels J C, Wang C Y and Elizondo J M 1995 *IEEE J. Quantum Electron.* **31** 599–612

Zhou B et al 2009 Opt. Express 17 11450-6

Zuev A A, Zemlyanov Yu, Kopytin D and Kuzikovskii A V 1985 *High Power Laser Radiation in Atmospheric Aerosols* (Dordrecht: VE Reidel Publ.)

Zvorykin V D, Ionin A A, Levchenko A O, Seleznev L V, Shutov A V, Sinitsyn D V, Smetanin I V and Ustinovskii N N 2013 Nucl. Instrum. Methods Phys. Res. B **309** 2218–22

Zvorykina V D, Ionina A A, Levchenkoa A O, Selezneva L V, Sinitsyna D V, Smetanina I V, Ustinovskiia N N and Shutova A V 2015 Plasma Phys. Rep. 41 112–46